FERMILAB-THESIS-2007-91

irect Searches for 3rd Generation Scalar Leptoquarks at the Run II Tevatron

A dissertation

submitted by

Hao Sun

in partial fulfillment of the requirements

for the degree of

Doctor of Philosophy

in

Physics

TUFTS UNIVERSITY

May 2007

Advisor: Professor Krzysztof Sliwa

irect Searches for 3rd Generation Scalar Leptoquarks at the Run II Tevatron

by Hao Sun

Adviser: Professor Krzysztof Sliwa

Abstract

This dissertation reports on a search for scalar Leptoquarks (LQ) decaying into third generation leptons and quarks. Based on extended gauge theories beyond the Standard Model, the Leptoquarks could be pair-produced in $p\bar{p}$ collisions. A Leptoquark would decay into a lepton and a quark of the same generation. In our analysis we have assumed a third generation Leptoquark would decay to a τ-lepton and a b-quark with 100% branching ratio. We focus our analysis with τ decays to electrons and muons only. Three final states associating with such decays from the decays of the $LQ\ \bar{LQ} \rightarrow \tau^+\tau^- b\bar{b}$ process are used in our searches: $e^+e^- b\bar{b}\ \not\!\!E_T$, $\mu^+\mu^- b\bar{b}\ \not\!\!E_T$, and $e\mu b\bar{b}\ \not\!\!E_T$, where $\not\!\!E_T$ represents the total transverse energy 'imbalance' in an event due to neutrinos from decay of τ-leptons, and b denotes a b-quark jet. The direct experimental search has been performed using data collected by the CDF detector at the Tevatron Collider during 2002-2006. No experimental signals have been observed in CDF data with an integrated luminosity of 361 pb^{-1} of $p\bar{p}$ collisions at a center-of-mass energy of 1.96 TeV. Using the next to leading order theoretical cross section calculations for scalar Leptoquark production in $p\bar{p}$ collisions [2], we set new mass limits on third generation scalar Leptoquarks. We exclude the existence of third generation scalar Leptoquarks with masses below 115 GeV for leptonic tau decay channels.

Acknowledgments

First of first, I would like to thank my advisor Professor Krzysztof Sliwa. His vision, his knowledge, and his passion always guide and encourage me during my time as a graduate student. Not only in the academic field, but also in the real life, his wisdom and patience enlightens me to grow up. Second I would reserve my special thanks to Dr. Simona Rolli. I have been worked with Simona in years in Fermilab. From the beginning till the end, she helped me to resolve tons of problems and clarify many detailed, or even subtle issues in this analysis. Her experience and guidance plays a key role in my thesis process. I really enjoy and appreciate such collaboration with her.

I would also like to thank people from both Tufts and CDF Fermilab. High-energy physics is what I'm interested since I was a under graduate student. I am really grateful for having the opportunity to join a such great high-energy physics group in Tufts. I meet amazing people here like Professor Austin Napier, Tony Mann, Bill Oliver and Jack Schneps. Their passion and working attitude on particle physics inspires me everyday here in the Science and Technology center. I also want to thank Professors Roger Tobin, Ford Lawrence, Alexander Vilenkin, Peggy Cebe and Allen Everett for giving their fantastic lectures on our core graduate courses. Moreover, my thanks go to secretaries in Department of Physics: Waltye Greene, Gayle Grant, Jackie DiMichele, and Jean Intoppa, thank you from solving administrative issues to arranging every travel, so many things that I can count on you. As for students, Ben Whitehouse, Dan Ryan, Matt Hare are my friends. I prefer to call Ben and Matt "Gurus" since they are so good at linux/C++ and are capable to answer any questions I have. Regarding to CDF, I would like to thank Stephan Lammel who is a great physcist, he helped a lot and provided many many valuable suggestions in my analysis. Beate Heinemann from CDF exotics group also gave me insights when I made presentation on the group meeting. Steve Hahn is another name in my mind for thanks. His knowledge and the sense of humor accompanied me in CDF central control room for three months. Thank you Steve, eventually that precious CDF scilicon detector was survived under my control and recorded the first physics run since its last Winter shutdown!

The last but not the least, I would like to thank my family. I thank my aunt Bing Zhou.

To me she is a professional model and example in physics , it is her who keeps me motivated and focused in this field. I'd like to thank my parrents, my cousin as well, I own you all. In the end my special thanks to my wife Dan Wang, your support is the reason that makes me move forward everyday.

Contents

Direct Searches for Scalar Leptoquarks at the Run II Tevatron

Introduction

The search for new particles is one of the most interesting topics in high energy experiments. Historically, whenever a new particle was discovered, our understanding in particle physics always had a big step forward. In many decades past, new particles were discovered at the **high energy frontier**, which is defined as the highest energy available in a facility to produce new particles. Based on Einstein's famous equation, $E = MC^2$, the higher the energy, the more mass (particles) can be produced. The Fermilab Tevatron Hadron Collider and the experiments at Fermilab, CDF and D0, have been at the 'high energy frontier' for new particle searches in the world.

This thesis work has focused on a search for a new type of particle, called a *Leptoquark* at the Fermilab Tevatron Hadron Collider, which collides proton and anti-proton beams with a center-of-mass energy of 1.96 TeV. This thesis work has used colliding beam data collected by the CDF experiment [1] during 2001-2006 in the Tevatron Run II physics program. A brief outline of the thesis is given below.

Part I discusses briefly the Standard Model of the particle physics. Most of this chapter is devoted to describing the theories beyond the Standard Model, which predict the new particles, *leptoquark* (LQ). The production mechanism and the decays modes of the LQ are presented. The search mode and the experimental signature of the LQ are discussed in detail.

Part II presents descriptions of the Tevatron Collider and the CDF detector. The main features of all the CDF sub-detectors are given. This chapter also provides information on the CDF experiment's data acquisition and trigger systems.

Part III includes three chapters which describe how the searches have been performed through data analysis. The basic framework of particle identifications for data analysis with the CDF experiment is presented in detail in Chapter 3. Event selections with different final states to search for the LQ signature are given in Chapter 4 and 5. Background contamination in the selected data sample is estimated using Monte Carlo simulated events and control data samples. The data analysis results, LQ cross-section limit and LQ mass limit are also given in Chapters 4 and 5.

Some information on CDF experimental details, cross checks on physics variables used in the analysis, and additional theoretical formulae are put in appendices.

Part I

Theoretical Motivation

Chapter 1

The Theory

1.1 The Standard Model

High energy physics is the quest to understand the most fundamental laws of Nature and to discover the universe's most basic building blocks. Modern physics has established a highly successful Standard Model to describe the current state of knowledge of elementary particles and their interactions.

The Standard Model contains 12 elementary flavors of fermions, so called because they are spin-$\frac{1}{2}$ and thus obey the Pauli exclusion principle and follow Fermi-Dirac statistics. The fermions, as shown in Table 1.1, consist of leptons (which only interact via the electromagnetic and weak nuclear forces) and quarks (which also interact via the strong nuclear force). The fermions appear to be grouped into three generations, each generation containing a pair of quarks and a pair of leptons. Only the first generation particles (the electron, electron-neutrino and up and down quarks) appear directly as constituents of normal matter, but Nature has provided two copies of the first generation at higher mass scales. The particles in the second and the third generations are unstable (with the exception of neutrinos), and after creation in high energy interactions, they quickly decay.

Each elementary fermion has its own antiparticle, with the same mass but opposite quantum numbers. The antiparticle is denoted by using the symbol for its corresponding particle with a line over it. For example, the up-quark is denoted as u, and anti-up is denoted as $\bar{u}$. For the charged leptons however, it is common to differentiate between particle and antiparticle by the sign of the charge. For example, the antiparticle of the electron (e^-) is the positron, denoted as e^+, rather than $\bar{e}$.

The Standard Model does not include gravitational interactions since they are many orders of magnitude smaller than the other three fundamental forces known in Nature – the strong nuclear force, the weak nuclear force and electromagnetic forces. Those three

Generation:	I	II	III	$Q/\|e\|$
Quarks	u	c	t	+2/3
	(Up)	(Charm)	(Top)	
	d	s	b	-1/3
	(Down)	(Strange)	(Bottom)	
Leptons	e	μ	τ	-1
	(electron)	(muon)	(Tau)	
	ν_e	ν_μ	ν_τ	0
		(Neutrinos)		

Table 1.1: Elementary particles in the Standard Model: the quark and lepton generations and their respective charges. $Q/|e|$ denotes the charge relative to the charge of the electron. The corresponding antiparticles have the opposite charge.

fundamental forces are described in terms of quantized gauge field theories [72]. The force carriers are presented as the quanta of the gauge fields in gauge theory, which are spin-1 vector-bosons.

The strong nuclear force is described by a non-Abelian gauge field theory with $SU(3)$ symmetry known as *Quantum Chromodynamics* (QCD). Its eight vector bosons are known as gluons, which couple to any particle with non-neutral strong charge (color) including themselves. The strong force prevents the existence of isolated non-neutrally colored particles at any directly-observable energy scales. Thus quarks are always detected only as constituents of color-neutral combinations of either a quark/anti-quark pair (a meson, such as the pion, π, and kaon, K) or three quarks (baryons, such as the proton and neutron). Mesons and baryons are collectively known as hadrons.

Electromagnetic and weak forces are combined into a single 'electroweak' force described by a gauge-field theory ([5] and [83]) with a underlying $SU(2)_L \times U(1)$ symmetry. At the energy scales we can observe, this symmetry is not apparent but is somehow spontaneously broken to produce the $U(1)$ of Quantum Electrodynamics (QED), with the photon as its vector boson, and the weak force with massive vector bosons, the Z^0 and $W^\pm$. Table 1.2 lists all the vector bosons described in the Standard Model.

In the Standard Model, the electroweak symmetry is broken by the Higgs mechanism [4], which generates the masses of the Z^0 and $W^\pm$, as well as the masses of the fermions. However, the Higgs boson (a spin-0 fundamental particle) predicted by the Standard Model remains to be discovered, and there is considerable theoretical debate on the exact form the symmetry breaking takes. The searches for the Higgs boson have been carried out from LEP (large-Electron-Positron Collider at CERN) to the Tevatron. The direct search from LEP experiments have set a mass limit for the Standard Model Higgs: $M_{Higgs} > 114\ GeV$. Searches at Tevatron are underway, and a small window still exists to find the Higgs using

Vector boson	Mass (GeV/C^2)	Electric charge
γ **(photon)**	0	0
W^-	80.22	-1
W^+	80.22	+1
Z^0	91.187	0
g **(gluon)**	0	0

Table 1.2: Standard Model Vector boson (spin-1 particles) list. γ interacts with electric charged particles only. $W^{\pm}$ and Z^0 are weak force carriers, interacting with all the fermions. Gluons are strong force carriers, interacting with quarks and themselves.

D0 and CDF experimental data. Most physicists believe that a decisive conclusion about the Higgs will be forthcoming at the LHC (Large Hadron Collider at CERN), which will turn on next year.

1.2 Beyond the Standard Model

Although the Standard Model is so successful in explaining a wide variety of physics, it tells us nothing about the masses and the mixing angles of quarks and leptons, the nature of the Higgs mechanism, and the values of the coupling constants. This proliferation of arbitrary parameters suggests the presence of new physics beyond the Standard Model. Many new physics models follow the approach of constructing the Lagrangian with larger extended symmetry at higher energies and the Standard Model becomes an effective theory at lower energies. Those models often predict a richer particle content, or may indicate a finer particle substructure.

The physics motivation of this thesis is to search for leptoquarks predicted by new physics models with the extended gauge symmetries. In those models Leptonquarks are new bosons coupling to a lepton-quark pair [2]. The characteristic feature of leptoquarks is that they are color-triplet particles carrying both baryon and lepton quantum numbers. They are assumed to be scalar (spin 0) or vector (spin 1) particles which can be produced both singly and in pairs in colliding beams. All other particle characteristics, such as weak isospin and electric charge, are model dependent. Like particles of the Standard Model, leptoquark masses are not predicted. Below we give brief discussions on theoretic models with extended gauge symmetries in which the Leptoquarks are predicted.

1.2.1 Grand Unification Models and Prediction of Leptoquarks

The success of using gauge field theories to describe particle interactions and the electroweak unification shows promise that perhaps all of the forces can be described by some

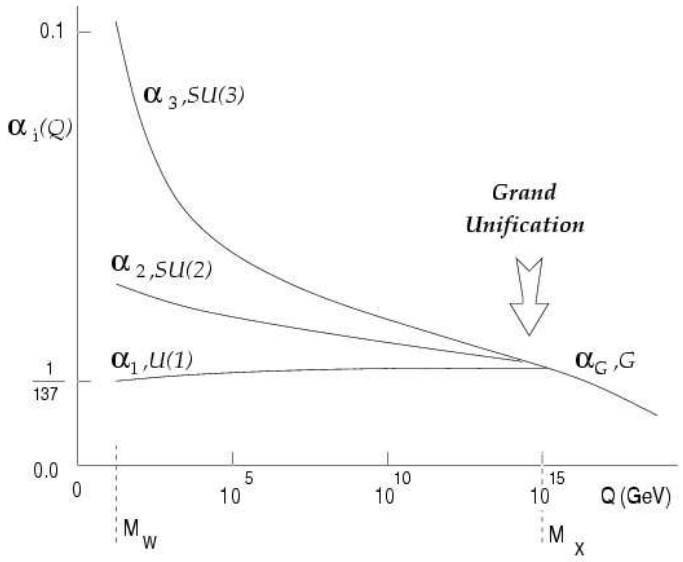

Figure 1.1: The strong, weak and electromagnetic couplings as a function of energy (from Kambara [84]).

larger encompassing gauge theory. Based on their unification it is natural to choose a larger gauge group, $\mathcal{G}$, that is large enough to contain the SM gauge symmetries. Such single gauge group would be able to describe the strong, weak, and electromagnetic interactions, i.e.

$$\mathcal{G} \supset SU(3) \times SU(2) \times U(1).$$

Unlike the SM that used three different coupling parameters to describe electroweak and strong interactions, in Grand Unification Theory (GUT) all interactions are determined by one single coupling constant. The previous electroweak couplings α_1 and α_2 and the strong coupling constant α_3 in the SM coincide at some large energy scale in GUT, which is approximately 10^{15} GeV. The key point for any GUT model is to combine electroweak and strong coupling constants (In fact they are not 'constant' but scale with the momentum transfer of an interaction), by doing so the larger symmetry is attained and the force unification is realized.

Figure 1.1 illustrates how the couplings of the $U(1)$, $SU(2)$ and $SU(3)$ groups evolve as a function of energy. At small energies, or large distances, α_3 asymptotically explodes due to quark confinement signaling the breakdown of QCD perturbation. Electroweak symmetry is still restored at energies around 10^2 GeV, but due to the coupling's logarithmic energy dependence, it isn't until 10^{15} GeV, or 10^{-31} m, that the couplings merge to a unified coupling g_G. At this very high energy scale the interactions would have the same intrinsic

strength and therefore there would be nothing to distinguish the leptons from the quarks. In fact, because the particles interact via the same unified coupling, leptons are allowed to transition to quarks and vice versa.

The simplest (also very elegant) GUT model is the $SU(5)$ model by Howard Georgi and Sheldon Glashow [69, 6]. In this model the $SU(3) \times SU(2) \times U(1)$ combination of gauge theories in the Standard Model are components of a $SU(5)$ gauge symmetry.

In earlier discussion we introduced $SU(3)$ triplets of colored quarks, and weak isospin $SU(2)$ doublets. Now in $SU(5)$ the basis of the group representation is constructed by 5-element vectors under 5-dimensional representation, 5 X 5 traceless matrix under 10-dimensional representation.

For instance, the first-generation fermions may be assigned as:

$$\psi_{jL} = \begin{pmatrix} d_1^c \\ d_2^c \\ d_3^c \\ \hline e \\ -\nu_e \end{pmatrix}_L \tag{1.1}$$

and

$$\psi_L^{jk} = \frac{1}{\sqrt{2}} \left(\begin{array}{ccc|cc} 0 & u_3^c & -u_2^c & -u_1 & -d_1 \\ -u_3^c & 0 & u_1^c & -u_2 & -d_2 \\ u_2^c & -u_1^c & 0 & -u_3 & -d_3 \\ \hline u_1 & u_2 & u_3 & 0 & -e^c \\ d_1 & d_2 & d_3 & e^c & 0 \end{array} \right)_L \tag{1.2}$$

where the quark colors (Red, Blue, Green) are denoted as (1,2,3). The electric charge is a generator of the $SU(5)$ group which enables an account of charge quantization.

For gauge boson content, we shall encounter 24 gauge bosons corresponding to the 24 elements of the adjoint representation of $SU(5)$. The first twelve of them are precisely the known gauge bosons of the $SU(3)_c \times SU(2)_L \times U(1)_Y$ theory: Eight gluons from QCD, and four electroweak bosons W^+, W^-, Z^0 and photon. The last dozen objects are new in $SU(5)$ model. X and Y have charges $q = \pm 4/3, \pm 1/3$ respectively. The $SU(5)$ gauge bosons may be displayed in matrix form as

$$\sqrt{2}\mathbf{V} = \left(\begin{array}{ccc|cc} & & & X_1 & Y_1 \\ & \text{gluons} & & X_2 & Y_2 \\ & & & X_3 & Y_3 \\ \hline X_{\bar{1}} & X_{\bar{2}} & X_{\bar{3}} & W_3/\sqrt{2} & W^+ \\ Y_{\bar{1}} & Y_{\bar{2}} & Y_{\bar{3}} & W^- & -W_3/\sqrt{2} \end{array}\right) + \frac{\mathscr{A}}{\sqrt{30}} \begin{pmatrix} -2 & & & & \\ & -2 & & 0 & \\ & & -2 & & \\ & 0 & & -3 & \\ & & & & -3 \end{pmatrix} \quad (1.3)$$

These new X and Y bosons are often called *leptoquarks* because they mediate transitions between quarks and leptons. Since the interactions mediated by X and Y violate conservation of baryon number, proton decay becomes a natural and interesting outcome based on this leptoquark mechanism. It is also an important feature of the $SU(5)$ model because it allows the model to be tested experimentally.

Another renormalizable GUT theory postulating the existence of leptoquark-like particles is the Pati-Salam Color Symmetric Model [107]. In this SM extension, the $SU(3)_c$ color group is extended to a $SU(4)_c$ group where lepton number L is the fourth color thus unifying baryonic and leptonic matter. The quarks form a quartet having quantum numbers of isospin, strangeness S, and charm C, giving a total global symmetry

$$SU(4)_L \times SU(4)_R \times SU(4)_c.$$

The gauge bosons mediating the forces between the quarks and leptons are vector particles having a non-chiral coupling to the leptons and quarks. In the Pati-Salam model, the leptoquarks are not restricted to couple uniquely within a lepton-quark generation [117]. These inter-generation couplings give rise to FCNC decays such as $B_s \to e\mu$ and $B^0 \to \tau\mu$ (see Figure 1.10). Searches for Pati-Salam leptoquarks at CDF in the Run I program resulted in mass constraints with a 95% C.L. of $M_{LQ} > 19.3$ TeV for a leptoquark coupling to e, μ and $M_{LQ} > 20.4$ TeV for a leptoquark coupling to e, τ [119].

1.2.2 The Buchmüller-Rückle-Wyler Leptoquark Classification

In 1997, Buchmüller-Rückle-Wyler developed a theoratical model (a.k.a. BRW model [39]) to generalize the possible leptoquark states that are consistent with the $SU(3) \times SU(2) \times U(1)$ framework. In this thesis we search for leptoquarks by using this model.

In Buchmüller-Rückle-Wyler model a general classification scheme is set up to include all possible lepton-quark couplings, in this way leptoquarks are categorized by corresponding couplings. Table 1.3 shows there are seven scalar (S) and seven vector (V) leptoquark models in this classification. All these models should satisfy the $SU(3) \times SU(2) \times U(1)$ gauge symmetry of the Standard Model.

In the first column of the table we see seven scalar leptoquarks (spin = 0) followed by seven vector leptoquarks (spin = 1). The L and R superscripts denote whether the leptoquark couples to a left- or right-handed lepton, and the subscript stands for the weak isospin, e.g. $S^L_{1/2}$ is a scalar left-handed leptoquark with weak isospin value 1/2, while V^R_0 is a vector right-handed leptoquark with weak isospin value as 0. Q is the electric charge in the unit of electron charge e. F, is a so-called fermion number defined as $F = L+3B$, where L is the lepton numberand B is the baryon number (i.e. electron has $L = +1$, quarks have $B = +1/3$). In the "coupling" column of the table, λ stands for the unknown leptoquark coupling to leptons and quarks.

There is an important assumption in BRW model: Both the lepton number and baryon number must be conserved separately in leptoquark decays. This means leptoquarks could have a mass as light as $\sim$ 100 GeV/c^2 while avoiding conflicts with rapid proton decay and excluding flavour changing neutral currents [75]. Since leptoquarks only couple to one generation by this assumption, it brings the classification of the first, second and third generation leptoquark. For this thesis, our search will focus on third-generation leptoquarks which couple only to third generation leptons (τ) and quarks (b). Furthermore, BRW models assume that the leptoquarks are chiral, which means the can only couple to left- or right-handed leptons. The last column of Table 1.3, "Squark" denotes as the possible squark assignments in the MSSM theory with broken R-parity (For more details about Supersymmetry (SUSY), Minimal Supersymmetric Standard Model (MSSM) and R-parity conservation in SUSY, see [64] and discussions in appendix B).

Table 1.3 implies charge conjugation symmetry. We can also make *global* replacement on third-generation particles with the corresponding ones in first and second generation.

Model	F	Charge Q	β	Coupling	Squark
S_0^L	2	-1/3	0.5	$\lambda_L(\tau_L^- t), -\lambda_L(\nu b)$	$\tilde{b}_R$
S_0^R	2	-1/3	1	$\lambda_R(\tau_R^- t)$	
$\tilde{S}_0^R$	2	-4/3	1	$\lambda_R(\tau_R^- b)$	
$S_{1/2}^L$	0	-5/3	1	$\lambda_L(\tau_L^- \bar{t})$	
		-2/3	0	$\lambda_L(\nu \bar{t})$	
$S_{1/2}^R$	0	-5/3	1	$\lambda_R(\tau_R^- \bar{t})$	
		-2/3	1	$-\lambda_R(\tau_R^- \bar{b})$	
$\tilde{S}_{1/2}^L$	0	-2/3	1	$\lambda_L(\tau_L^- \bar{b})$	$\bar{\tilde{t}}_L$
		+1/3	0	$-\lambda_L(\nu \bar{b})$	$\bar{\tilde{b}}_L$
S_1^R	2	-4/3	1	$-\sqrt{2}\lambda_L(\tau_L^- b)$	
		-1/3	0.5	$-\lambda_L(\tau_L^- t), -\lambda_L(\nu b)$	
		+2/3	0	$\sqrt{2}\lambda_L(\nu t)$	
V_0^L	0	-2/3	0.5	$\lambda_L(\tau_L^- b), \lambda_L(\nu \bar{t})$	
V_0^R	0	-2/3	1	$\lambda_R(\tau_R^- \bar{b})$	
$\tilde{V}_0^R$	0	-5/3	1	$\lambda_R(\tau_R^- \bar{t})$	
$V_{1/2}^L$	2	-4/3	1	$\lambda_L(\tau_L^- b)$	
		-1/3	0.5	$\lambda_L(\nu b)$	
$V_{1/2}^R$	2	-4/3	1	$\lambda_R(\tau_R^- b)$	
		-1/3	1	$\lambda_R(\tau_R^- t)$	
$\tilde{V}_{1/2}^L$	2	-1/3	1	$\lambda_L(\tau_L^- t)$	
		+2/3	0	$\lambda_L(\nu t)$	
V_1^L	0	-5/3	1	$\sqrt{2}\lambda_L(\tau_L^- \bar{t})$	
		-2/3	0.5	$-\lambda_L(\tau_L^- \bar{b}), \lambda_L(\nu \bar{t})$	
		+1/3	0	$\sqrt{2}\lambda_L(\nu \bar{b})$	

Table 1.3: A classification of leptoquarks in the Buchmüller-Rückl-Wyler leptoquark scheme [39] adopted from [110]. Shown is the leptoquark fermion number $F = 3B + L$, the electric charge Q in units of e, the branching ratio β, and the lepton-quark couplings. The last column shows the possible squark assignments to the leptoquark states in the MSSM with broken R-parity. The classification assumes conjugation symmetry and the ability to globally replace the second-generation particles with first- or third-generation particles.

In this thesis we searched for leptoquarks in the $\tau q \tau q$ leptonic channels, corresponding to the BRW leptoquark $\tilde{S}^L_{1/2}$. Although the coupling assignments for these scalar leptoquarks correspond to the MSSM squarks $\tilde{d}_R$ and $\bar{\tilde{c}}_L$, the searches in this analysis are not squark searches because the squark production cross sections are not the same as the leptoquark production cross sections as discussed in Section 1.3.1.

In addition, there are many other theoretical models that either predict the existence of such hypothetical particles, or they derive virtual particles which share similar properties and decay signature of leptoquarks. In fact that's one of the motivations for searching for leptoquarks, since they appear in a consistent way in a wide range of theories. We can't list all such theories here, however two additional models, Technicolor and SUSY are briefly introduced in appendix B.

1.3 Leptoquark Production in $p\bar{p}$ Collision

There are two possible ways to produce leptoquarks directly at theTevatron, due to its high center mass energy $\sqrt{s}$, either singly or in pairs.

$$p + \bar{p} \rightarrow LQ + \overline{LQ} + X, \tag{1.4}$$

$$p + \bar{p} \rightarrow LQ + \bar{\ell} + X \tag{1.5}$$

Figure 1.2 illustrates the Feynman diagrams of single leptoquark production.

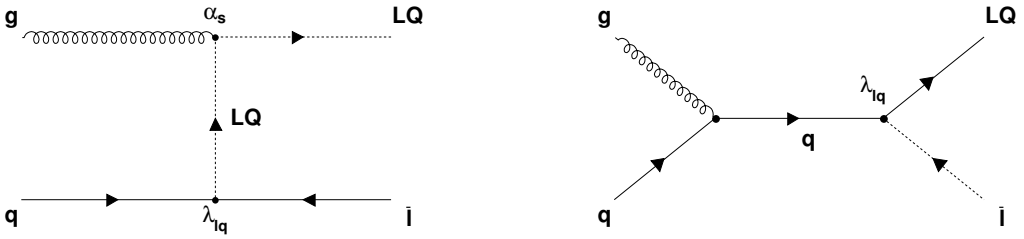

Figure 1.2: Feynman diagrams of the parton tree-level process $gq \rightarrow LQ\ell$. The parameter $\lambda_{\ell q}$ represents the coupling between the lepton and quark.

At the current high-energy hadron colliders such as the Tevatron, the production cross-section for singly produced leptoquarks can be regarded as negligible. This is because it's quadratically dependent on the leptoquark fermionic couplings $\lambda_{\ell q}$ between the lepton and quark. With the combined bound of leptoquark mass and the coupling constant $\lambda_{\ell q}$, the chance to find a singly produced leptoquark will be very limited in the mass range up to

$\mathcal{O}(1\ \text{TeV})$ [34]. For example, in the case that $M_{LQ_s} = 200\ \text{GeV/c}^2$ and $\lambda_{\ell q} = e/10$, one finds $\sigma[p\bar{p} \to LQ_s\bar{\ell}] \sim 4 \times 10^{-3}$ pb [86]. Theoretical limits on the production cross section of singly-produced leptoquarks at the Run I and Run II Tevatron have been calculated [61].

Therefore at Tevatron the major way to produce leptoquarks will be the pair-production. There are three production processes possible for pair-produced leptoquarks shown below:

$$q\,g \;\to\; LQ\,\overline{LQ}, \tag{1.6}$$

$$q\,\bar{q} \;\to\; LQ\,\overline{LQ}, \tag{1.7}$$

$$g\,g \;\to\; LQ\,\overline{LQ}. \tag{1.8}$$

The process in Equation 1.6 contributes to the partonic cross-section in order α_s^3 and is included only in the Next-to-Leading Order (NLO) calculation as will be discussed in Section (1.3.1). The most common mechanism for leptoquark pair production at high-energy hadron colliders is both quark-antiquark annihilation (Equation 1.7) and gluon fusion (Equation 1.8). Figures 1.3 and 1.4 show the leading order contributions to the partonic pair production cross-section. At the Tevatron quark-antiquark annihilation is the largest contribution to the cross section coming from the s-channel.

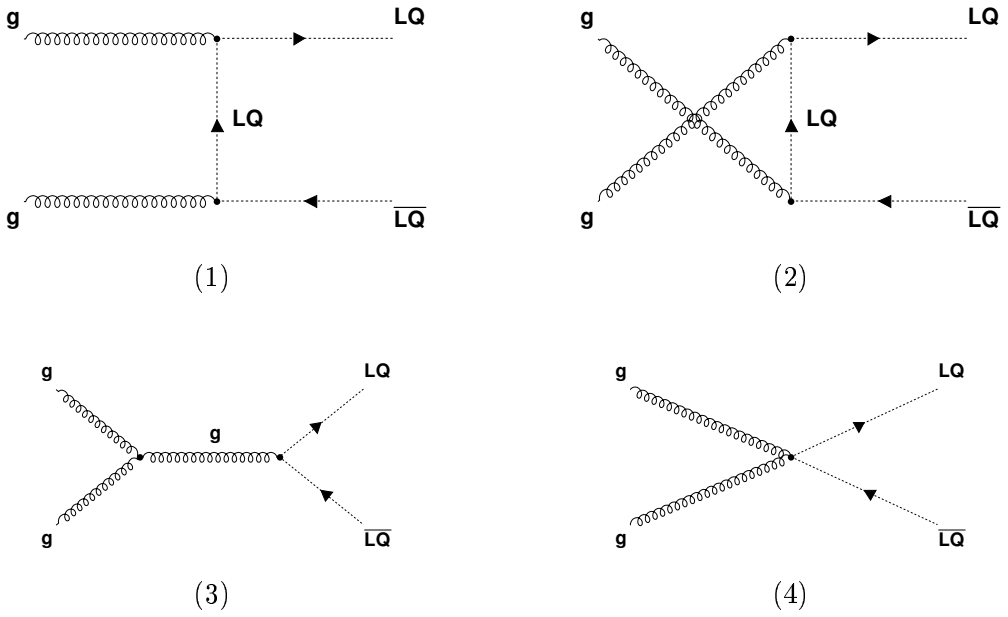

Figure 1.3: Feynman diagrams of the parton level process $gg \to LQ\overline{LQ}$.

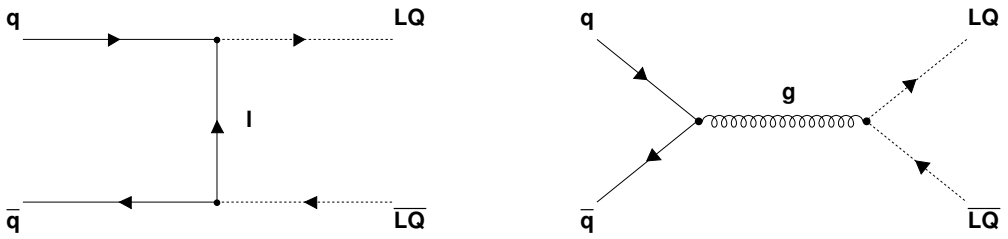

(5) (6)

Figure 1.4: Feynman diagrams of the parton level process $q\bar{q} \to LQ\overline{LQ}$ (5-6).

The effective Lagrangian describing scalar and vector leptoquark interactions with gluons is given below:

$$\mathscr{L} = \mathscr{L}_S^g + \mathscr{L}_V^g, \tag{1.9}$$

where

$$\mathscr{L}_S^g = \sum_{scalars} \left\{ (\mathcal{D}_{ij}^{\mu}\Phi^j)^{\dagger}(\mathcal{D}_{\mu}^{ik}\Phi_k) - M_S^2\Phi^{i\dagger}\Phi_i \right\}, \tag{1.10}$$

$$\mathscr{L}_V^g = \sum_{vectors} \left\{ -\frac{1}{2}G_{\mu\nu}^{i\ \dagger}G_i^{\mu\nu} + M_V^2\Phi_{\mu}^{i\ \dagger}\Phi_i^{\mu} - ig_s\left[(1-\kappa_G)\Phi_{\mu}^{i\ \dagger}t_{ij}^a\Phi_{\nu}^j\xi_a^{\mu\nu} + \frac{\lambda_G}{M_V^2}G_{\sigma\mu}^{i\ \dagger}t_{ij}^aG_{\nu}^{j\mu}\xi_a^{\mu\sigma}\right]\right\}. \tag{1.11}$$

where g_s is the strong coupling constant, t_a are the generators of $SU(3)_c$, M_S (M_V) is the scalar (vector) leptoquark mass, and κ_G and λ_G are the anomalous coupling constants. The gluon field strength tensor and vector leptoquark field strength tensor are shown respectively as follows [34]:

$$\xi_{\mu\nu}^a = \partial_\mu A_\nu^a - \partial_\nu A_\mu^a + g_s f^{abc}A_{\mu b}A_{\nu c},$$
$$\xi_{\mu\nu}^i = \mathcal{D}_{\mu}^{ik}\Phi_{\nu k} - \mathcal{D}_{\nu}^{ik}\Phi_{\mu k},$$

To achieve local gauge invariance, the covariant derivative is defined as:

$$\mathcal{D}_{\mu}^{ij} = \partial_\mu\delta^{ij} - ig_s t_a^{ij}A_\mu^a, \tag{1.12}$$

where A_μ^a is the local transformation field containing a non-Abelian tensor term.

The gluon-leptoquark interactions are determined by the non-Abelian $SU(3)_c$ gauge-

symmetry of scalar QCD, making theoretical calculation of the pair-production cross-section dependent on the leptoquark quantum numbers and independent of the lepton-quark coupling, λ_{lq} [2]. For the case of scalar leptoquarks that is interested in this thesis, it means that the production cross-section can be calculated as a function of leptoquark mass only. For the case of vector leptoquarks, the production cross-section depends on the values of the anomalous couplings. These couplings are related to the magnetic moment μ_V and electric quadrupole moment q_V by [34]

$$\mu_V = \frac{g_s}{2M_V}(2 - \kappa_G + \lambda_G), \tag{1.13}$$

$$q_V = -\frac{g_s}{M_V^2}(1 - \kappa_G - \lambda_G), \tag{1.14}$$

respectively. There are no direct bounds on the vector leptoquark anomalous couplings, but they are assumed to be real numbers. There are typically two choices to constrain the couplings:

- Yang-Mills type coupling where $\kappa_G = \lambda_G = 0$
- Minimal Vector type coupling where $\kappa_G = 1, \lambda_G = 0$

The Minimal Vector type coupling has a smaller calculated cross section than the Yang-Mills type coupling and both have larger cross sections than scalar leptoquarks. Again we need not worry about the coupling with μ_V and q_V because we only serach for scalar leptoquarks in this analysis.

1.3.1 Leading Order and Next-to-Leading Order Cross Section

The differential leading order (LO) partonic scattering cross-sections for quark-antiquark annihilation and gluon fusion are given by [3]:

$$\frac{d\sigma_{LO}}{d\cos\theta}\left[q\bar{q} \to LQ_S\,\overline{LQ}_S\right] = \frac{\alpha_s^2\pi}{18\hat{s}}\beta^3\sin^2\theta, \tag{1.15}$$

$$\frac{d\sigma_{LO}}{d\cos\theta}\left[gg \to LQ_S\,\overline{LQ}_S\right] = \frac{\alpha_s^2\pi}{6\hat{s}}\left\{\frac{1}{32}\left[25 + 9\beta^2\cos^2\theta - 18\beta^2\right] - \frac{1}{16}\frac{(25 - 34\beta^2 + 9\beta^4)}{1 - \beta^2\cos^2\theta} + \frac{(1-\beta^2)^2}{(1-\beta^2\cos^2\theta)^2}\right\}, \tag{1.16}$$

where $\sqrt{\hat{s}}$ is the invariant energy of the subprocess, α_s is the strong coupling constant, and $\beta = (1 - 4M_{LQ}^2/\hat{s})^{1/2}$. In the integral form they appear as:

$$\sigma_{LO}\left[q\bar{q} \to LQ_S\,\overline{LQ}_S\right] = \frac{\alpha_s^2\pi}{\hat{s}}\frac{2}{27}\beta^2, \tag{1.17}$$

$$\sigma_{LO}\left[gg \to LQ_S\,\overline{LQ}_S\right] = \frac{\alpha_s^2\pi}{96\hat{s}}\left\{\beta(41 - 31\beta^2) + (18\beta^2 - \beta^4 - 17)\log\frac{1+\beta}{1-\beta}\right\}. \tag{1.18}$$

Analogous to equations 1.17 and 1.18, the vector leptoquark leading-order scattering cross-sections are given by [4]:

$$\sigma_{LO}\left[q\bar{q} \to LQ_V\,\overline{LQ}_V\right] = \frac{\alpha_s^2\pi}{27\hat{s}}\frac{\beta^3}{1-\beta^2}\left[23 - 3\beta^2 + \frac{4}{1+\beta^2}\right], \tag{1.19}$$

$$\sigma_{LO}\left[gg \to LQ_V\,\overline{LQ}_V\right] = \frac{\alpha^2\pi}{24\hat{s}}\frac{1}{(1-\beta^2)}\left\{\beta(\frac{523}{4} - 90\beta^2 + \frac{93}{4}\beta^4) - \frac{3}{4}(65 - 83\beta^2 + 19\beta^4 - \beta^6)\log\frac{1+\beta}{1-\beta}\right\}, \tag{1.20}$$

The Next-to-Leading Order (NLO) cross section for pair-produced leptoquarks at the Tevatron has also been calculated [2]. The NLO calculation includes the virtual gluon loop corrections (see diagrams in Figure 1.5), initial state and final state gluon radiations (see diagrams in Figure 1.6) and gluon 'compton process' (see diagrams in Figure 1.7).

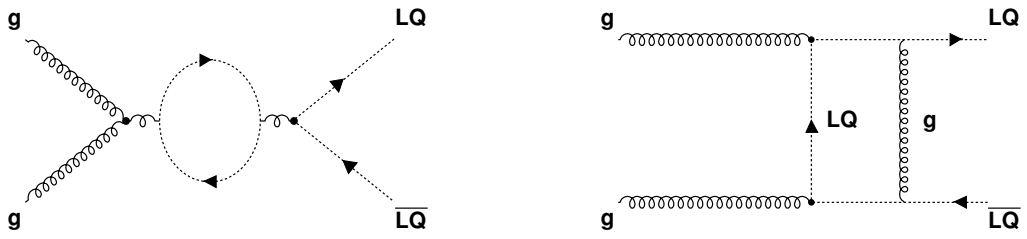

(7) (8)

Figure 1.5: Example Feynman diagrams for virtual gluon corrections involving self-energy and vertex correction.

We exclude the non-point-like structures of leptoquarks in this analysis. Such models are not expected below energy scales of $\sim$ 1 TeV, this was predicted by Schrempp's paper as early as 1985 [108]. Thus in this thesis we will treat leptoquarks as point-like particles to calculate their production cross sections.

To determine the total NLO cross-section for pair produced scalar leptoquarks, the contributions from the QCD corrections are folded into the LO partonic cross-section and

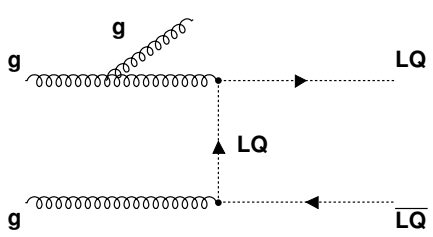

(9)

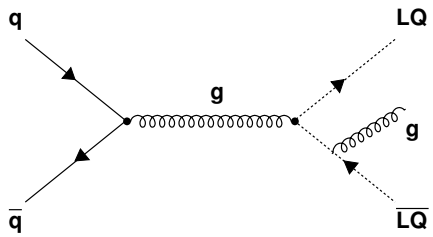

(10)

Figure 1.6: Generic Feynman diagrams for gluon radiation.

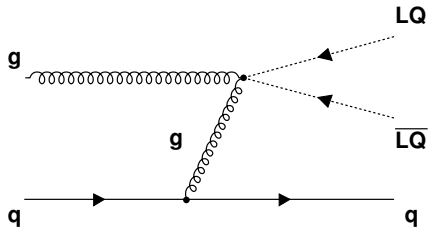

(11)

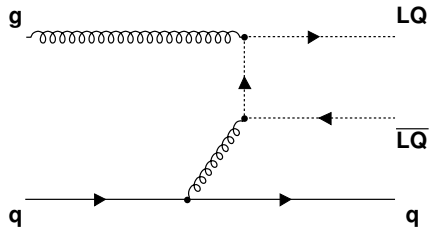

(12)

Figure 1.7: Generic Feynman diagrams for gluon 'Compton' scattering.

perturbatively expanded in terms of scaling functions f_{ij}:

$$\hat{\sigma}_{ij}(s, M_{LQ}^2) = \frac{\alpha_s^2 \mu^2}{M_{LQ}^2} \left[f_{ij}^{(0)}(\eta) + 4\pi\alpha_s\mu^2 \times \left\{ f_{ij}^{(1)}(\eta, r_t) + \overline{f}_{ij}^{(1)}(\eta) \log \frac{\mu^2}{M_{LQ}^2} \right\} \right], \quad (1.21)$$

where $i, j = g, q, \bar{q}$ denote the initial-state partons and μ is the renormalization and factorization scale. The scaling functions in equation (1.21) depend on the invariant parton energy $\sqrt{\hat{s}}$ and leptoquark mass M_{LQ} through $\eta = \hat{s}/4M_{LQ}^2 - 1$ and on $r_t = m_{top}/M_{LQ}$, the mass ratio of the top quark and leptoquark.

A numerical result for the leptoquark production cross-section cannot be produced analytically because of the composite nature of the proton and antiproton. The parton subprocess cross-section can be computed analytically, but this must be summed over all possible pairs of participating partons in the proton and antiproton and additionally integrated over the parton momentum distributions. In our experiment *event generator* programs, such as **PYTHIA** can be used to fully model the leptoquark productions in $p\bar{p}$ collisions, which includes using the initial state parton-density-functions (PDF) to calculate the partonic cross-

sections and producing the final state quark hadronic-jets. The parton density parameterization used in our analysis is CTEQ6.1 [35]. The values of $K = \sigma_{NLO}/\sigma_{LO}$ for cross-section calculations are evaluated in the leptoquark mass range between $150 \leq M_{LQ}/\mathrm{GeV/c^2} \leq 250$ and vary only between 1.20 and 1.08 [2].

Figure 1.8 shows the cross section as a function of factorization scale for a scalar leptoquark mass of 220 GeV/c^2 at the Run II Tevatron. In the LO case, the cross-section is heavily

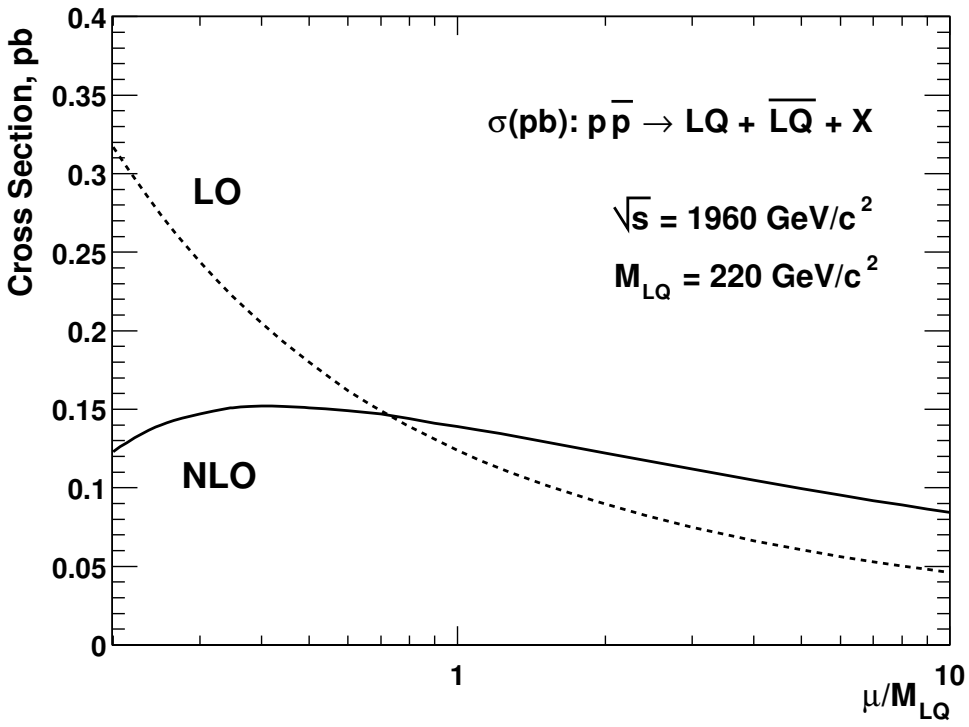

Figure 1.8: The theoretical scalar leptoquark cross section as a function of factorization/normalization scale at the Run II Tevatron.

dependent on the factorization scale. A change of scale from $\mu = 2M_{LQ}$ to $\mu = M_{LQ}/2$ increases the cross section by 100%. This scale dependence is reduced dramatically by the QCD corrections in the NLO case, varying by only 30% within the same factorization range.

The values for the LO and NLO theoretical cross-section for a range of scalar leptoquark masses is shown in Table 1.4. Figure 1.9 shows the theoretical cross sections for Tevatron energies in Run I and Run II. The NLO cross sections for $\sqrt{s} = 1960$ GeV are used in this analysis to set upper limits on the scalar leptoquark mass.

M_{LQ} (GeV/c^2)	σ_{gg} (pb)		$\sigma_{q\bar{q}}$ (pb)		σ_{gq} (pb)	σ_{tot} (pb)		K
	LO	NLO	LO	NLO	NLO	LO	NLO	
100	6.03	10.9	5.93	5.66	-0.332	12.0	16.3	1.36
140	0.617	1.20	1.31	1.26	-0.057	1.92	2.40	1.25
180	0.0904	0.184	0.356	0.349	-0.012	0.446	0.521	1.17
220	0.0162	0.0342	0.107	0.108	-0.00259	0.123	0.139	1.13
260	0.00327	0.00708	0.0345	0.0346	-0.000627	0.0378	0.0411	1.09
300	0.000716	0.00156	0.0113	0.0115	-0.000157	0.0121	0.0129	1.07

Table 1.4: Theoretical scalar leptoquark cross-sections for $p\bar{p}$ collisions at $\sqrt{s} = 1.96$ TeV.

1.3.2 Leptoquark Decay

Experimental limits set some restrictions on the properties of leptoquarks. For example, due to experimental limits on helicity-suppressed leptonic pion decays, most theories require that leptoquarks be essentially chiral, which means leptoquarks can't shift from left-handed to right-handed particles freely. Another restriction on leptoquarks is about their couplings or lepton-quark quantum numbers. Someone may argue that there is no arbitrary reason to forbid leptoquarks couple to any lepton-quark combination, for example SU(5) model allow such decay happens. However the obvious downfall of a leptoquark theory with universal couplings would be that such leptoquarks would give rise to flavor-mixing-induced FCNC.

It is important to note that although one can require leptoquarks to have chiral and family diagonal couplings, the $SU(2)_L$ eigenstates of the quarks and leptons are not their mass eigenstates and thus lepton-quark mixing can still give rise to inter-generation decays so long as the charge is conserved [75]. Examples of such flavor-mixing-induced FCNC would be $K_L^0 \to e\mu, D^0 \to \pi^0 e\mu$, or $B^0 \to \mu\tau$ as shown in Figure 1.10. However, the bounds that are obtainable from such FCNC involve several unknown parameters and are *weaker* than experimental limits set by direct searches.

Experimental limits on FCNC indicate that flavor-mixing is severely suppressed and thus leptoquarks are assumed to decay uniquely within a lepton-quark generation. In this analysis we focus on leptoquarks exhibiting family-diagonal decays. Figure 1.11 shows two possible decays for a third-generation leptoquark. The parameter β is the branching ratio of leptoquark decays into a charged lepton-quark pair and a neutrino-quark pair. Since we search for leptoquarks in pairs, there is a combinatorial ambiguity as to which leptoquark decays into a charged lepton and quark. The combinatoric rates are given by:

$$LQ_3 \to q_3\tau^{\pm} \qquad BR = \beta \tag{1.22}$$

$$LQ_3 \to q_3\nu_\tau \qquad BR = 1 - \beta. \tag{1.23}$$

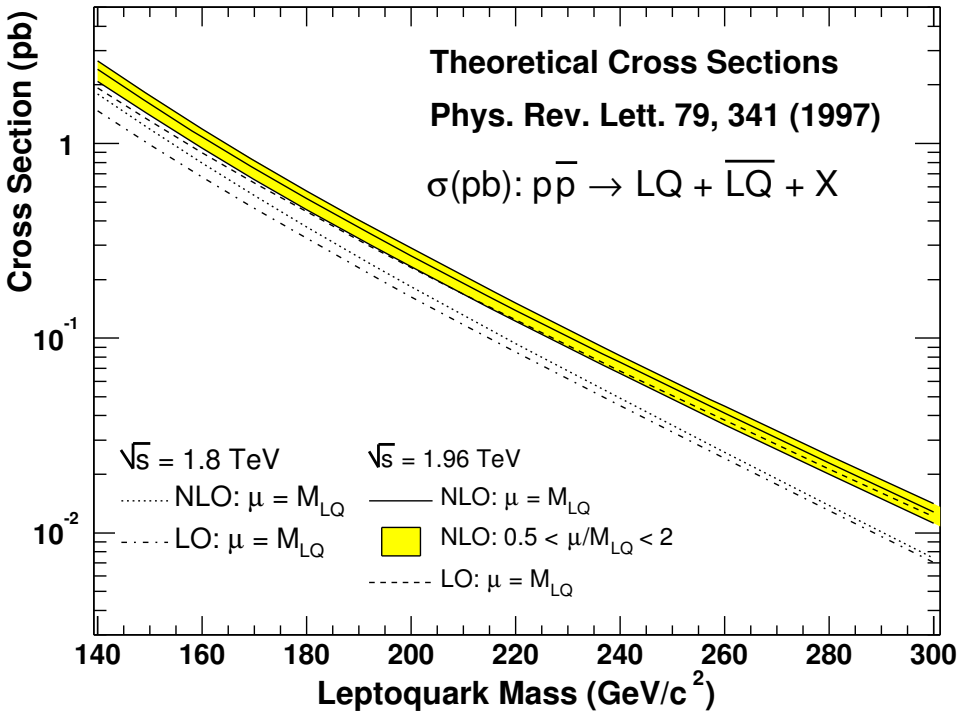

Figure 1.9: The theoretical scalar leptoquark cross section as a function of leptoquark mass at the Run I and Run II Tevatron.

Therefore, the combinatoric rates for the channels $\ell\ell qq$, $\ell\nu qq$ and $\nu\nu qq$ channels are respectively $BR = \beta^2, 2\beta(1-\beta)$, and $(1-\beta)^2$.

Tau-Lepton Decay Modes

As the heaviest lepton among three generations, the τ has multiple decay channels. In general we can divide τ decays into two categories: the hadronic decay and the leptonic decay. In hadronic mode τ decay is associated with pions and kaons; while in leptonic mode, the tau decays to the less heavy leptons (electron or muon). In this thesis we focus on leptonic decay analysis. The result from chapters 4 and 5 shows that although leptonic modes are not the dominant channels in tau decays, there is enough sensitivity to filter decay signature from backgrounds.

Table 1.5 lists the branching ratios for each channel in τ decays.

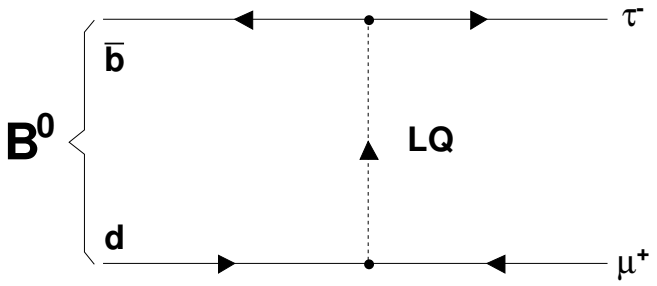

Figure 1.10: An example of a leptoquark induced FCNC decay process $B^0 \rightarrow \mu\tau$. The leptoquark LQ couples with more than one lepton-quark generation.

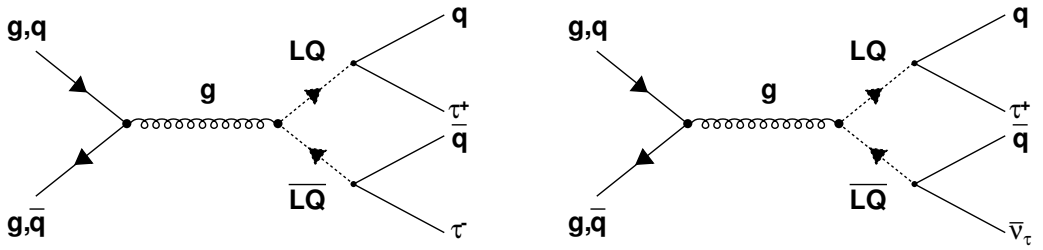

$\beta = 1$ $\beta = 1/2$

Figure 1.11: The third generation scalar leptoquark decay for $\beta = 1$ (left) and $\beta = 1/2$ (right).

1.3.3 Previous Leptoquark Search Results

In February, 1997, the H1[7] and ZEUS[121] collaborations working on e^+p collisions at HERA accelerator in DESY, Germany, simultaneously released papers reporting an excess of NC events with high Q^2. This was regarded as a hint of a leptoquark signature. Since then, many results on leptoquarks searches have been published.

What makes things more interesting was that by end of 1997, H1 observed a cluster of the events at a mass of about 200 GeV/c^2. This observation could be explained by the existence of scalar leptoquarks, or interpreted by scalar squarks in super-symmetric theories with R-parity breaking. Anyway, if low-mass scalar leptoquarks do exist, they would be produced at significant rates at the $p\bar{p}$ Tevatron Collider. So immediately both CDF [62] and DØ[77] conducted searches for leptoquarks using Run I Tevatron data and reported a combined lower limit of $M_S > 242$ GeV/c^2 [40]. For the vector leptoquark case, even at choices of κ and λ such that the cross section is minimized [34], the lower mass bounds were

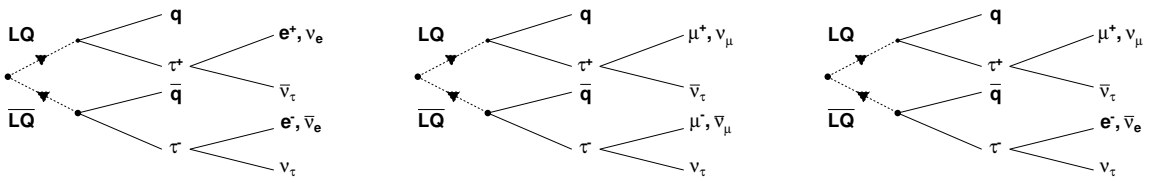

Figure 1.12: The leptonic decays for third generation leptoquarks.

Channel	Branching Ratio
Hadronic Decay	
$\pi^-\nu_\tau$	$(11.31 \pm 0.15)\%$
$K^-\nu_\tau$	$(7.1 \pm 0.5) \times 10^{-3}$
$\pi^-\bar{K}^0\nu_\tau$	$(7.7 \pm 0.8) \times 10^{-3}$
$\pi^-\pi^0\nu_\tau$	$(25.24 \pm 0.16)\%$
$\pi^-2\pi^0\nu_\tau$	$(9.27 \pm 0.14)\%$
$\pi^-\pi^+\pi^- \geq 0\nu_\tau$	$(14.09 \pm 0.31)\%$
Leptonic Decay	
$\mu^-\bar{\nu}_\mu\nu_\tau$	$(17.35 \pm 0.10)\%$
$\mu^-\bar{\nu}_\mu\nu_\tau\gamma$	$(2.3 \pm 1.0) \times 10^{-3}$
$e^-\bar{\nu}_e\nu_\tau$	$(17.83 \pm 0.08)\%$

Table 1.5: Main decay channels of the τ lepton

significantly higher than the scalar limit.

The leptoquark searches from Run I at the Tevatron exclude the interpretation of the excess events found at HERA as being a result of the production of a leptoquark state with chiral and family-diagonal couplings to fermions [86]. ZEUS also observed a cluster in their data, but at a mass of about 220 GeV/c^2. This difference in energy between the H1 cluster and ZEUS's cluster was later ruled out by as resulting from initial state radiation or detector effects [24]. Thus it has been ruled unlikely that the excess observed at HERA was due to the production and decay of a single narrow resonance.

Since then, the data collected at H1 and ZEUS has doubled, and no excess events have been observed. For *ep* collisions, the production cross section does depend on the leptoquark coupling and thus mass limits have been set by both collaborations which depend on $\lambda_{\ell q}$. Figure 1.13 shows the leptoquark mass limits as a function of λ_{eu} for the $\beta = 1$ case. The diagram also shows the limits set by LEP. Figure 1.13 shows how the Tevatron limits relate to the mass limits set by LEP and HERA. For large coupling value, LEP and HERA limits are very high. The Tevatron limits are able to probe mass regions having a small coupling

constant. The published Run I Tevatron results are listed in Table 1.6. Preliminary results

Channel	$\mathcal{L}$, pb^{-1}	M, GeV/c^2	Comments
First Generation			
$eeqq$	110	213	CDF Collaboration [42]
$eeqq$	115	225	combined result, DØ Collaboration [54]
$eeqq$	123	225	DØ Collaboration [55]
$eeqq$	233	242	CDF and DØ combined result
$e\nu qq$	115	204	combined result, DØ Collaboration [54]
$\nu\nu qq$	85.2	98	DØ Collaboration [59]
Second Generation			
$\mu\mu qq$	110	202	CDF Collaboration [43]
$\mu\mu qq$	94	200	combined result, DØ [56]
$\mu\nu qq$	94	160	DØ Collaboration [57]
$\mu\nu qq$	94	180	combined result, DØ Collaboration [56]
$\nu\nu cc$	88	123	CDF Collaboration [46]
Third Generation			
$\tau\tau bb$	60,20,92	94	DØ Collaboration [58]
$\tau\tau bb$	110	99	CDF Collaboration [44]
$\nu\nu bb$	88	148	CDF Collaboration [46]

Table 1.6: Published results of scalar leptoquark searches from the Run I Tevatron. $\mathcal{L}$ is the time-integrated luminosity and M is the leptoquark mass below which scalar leptoquarks have been excluded at the 95% C.L. The $\tau\tau bb$ channel was analyzed by DØ using three sets of data collected using different triggers.

of scalar leptoquark searches at both the Run I and Run II Tevatron are shown in Table 1.7.

1.3.4 The Experimental Challenge

The search for the third generation of leptoquarks through the process

$$p\,\bar{p} \;\rightarrow\; LQ\;\bar{LQ} \rightarrow \tau^+\tau^-\;b\bar{b}$$

has great experimental challenges compared to the searches for the first and the second generation leptoquarks since the τ-lepton is unstable and quickly decay to leptons (e or μ) or hadrons with multiple neutrinos in the final states. The efficiency of τ identification is relatively low, and the fake identification rate is higher. Further more, the leptons from τ decays are relatively 'soft', thus trigger efficiency for such events will be low as well. The major background comes from top pair production:

$$p\,\bar{p} \;\rightarrow\; t\,\bar{t} \rightarrow W^+W^-\;b\bar{b}$$

followed by W's decay to leptons plus neutrinos.

The goal of the physics analysis in this thesis is to distinguish leptoquark signals from background with high efficiency to maximize the discovery potential at Tevatron. This thesis performed the searches in following three decay modes:

$$LQ\ \bar{LQ} \rightarrow \tau^+\tau^-\ b\bar{b} \rightarrow e^+e^-b\bar{b}\ \nu_e\bar{\nu}_e\nu_\tau\bar{\nu}_\tau$$

$$LQ\ \bar{LQ} \rightarrow \tau^+\tau^-\ b\bar{b} \rightarrow \mu^+\mu^-b\bar{b}\ \nu_\mu\bar{\nu}_\mu\nu_\tau\bar{\nu}_\tau$$

$$LQ\ \bar{LQ} \rightarrow \tau^+\tau^-\ b\bar{b} \rightarrow e\mu b\bar{b}\ \nu_e\nu_\mu\nu_\tau\bar{\nu}_\tau$$

The experimental event topologies for above processes are two isolated leptons (e, μ), two b-jets and large missing transverse energies due to neutrinos escaping detection. Detailed data analysis will be presented in Part III.

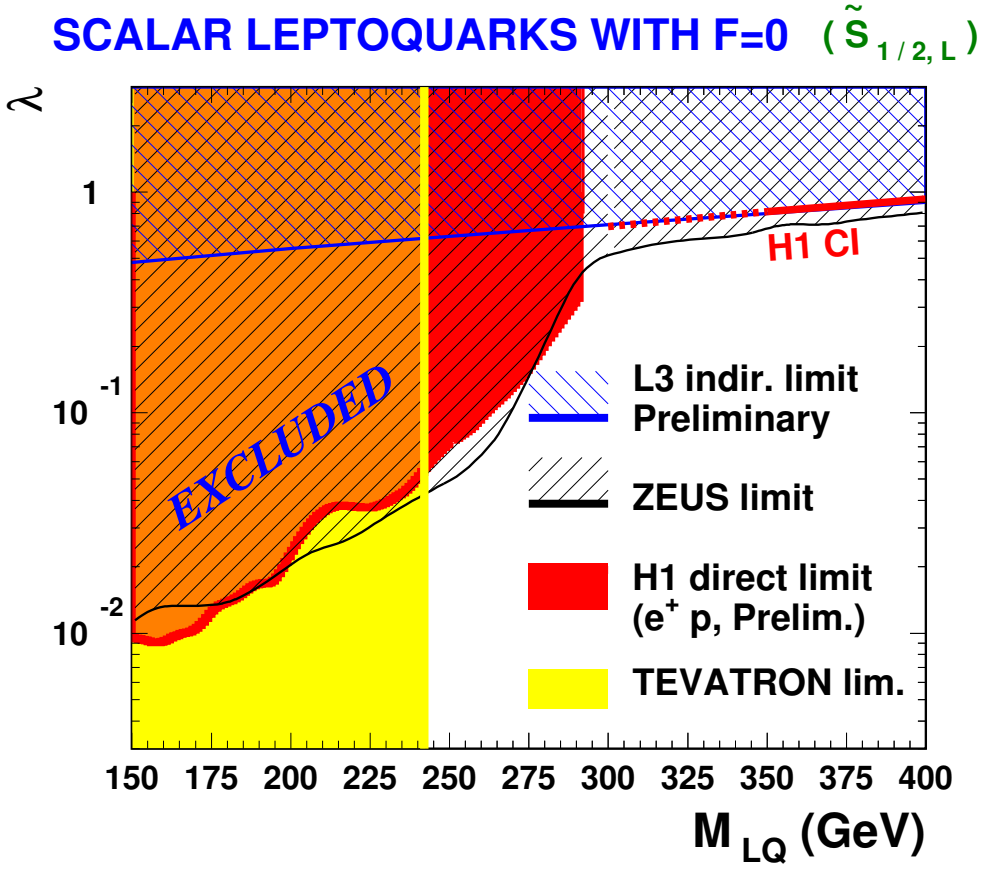

Figure 1.13: Limits on the first-generation scalar leptoquark mass as a function of the leptoquark coupling (from ZEUS Collaboration [120]). The limit for the Tevatron, which is independent of the leptoquark coupling, is from combined CDF and DØ results from Run I.

Channel	$\mathscr{L}$, pb^{-1}	M, GeV/c^2	Comments
First Generation			
$eeqq$	175	238	DØ Run II Preliminary
$eeqq$	203	230	CDF Run II Preliminary
$e\nu qq$	175	194	DØ Run II Preliminary
$e\nu qq$	72	166	CDF Run II Preliminary
$\nu\nu qq$	191	78-117	CDF Run II Preliminary [27]
Second Generation			
$\mu\mu qq$	104	186	DØ Run II Preliminary
$\mu\mu qq$	109	209	CDF Run I Preliminary, combined result [95]
$\mu\mu qq$	126	206	CDF Run II Preliminary [103]
$\mu\nu qq$	109	164	CDF Run I Preliminary [96]
$\mu\nu qq$	109	183	CDF Run I Preliminary, combined result [95]

Table 1.7: Preliminary results of scalar leptoquark searches at the Run I and Run II Tevatron. Note that no results have been produced from CDF and D0 in searches for Third Generation Leptoquarks in the Run II program.

Part II

Experimental Apparatus

Chapter 2

The Apparatus

2.1 Fermilab Accelerator and Tevatron in Run II

The Tevatron is a proton-antiproton collider at the Fermi National Accelerator Laboratory (Fermilab), located on 6,800 acres of land approximately 40 miles west of Chicago, Illinois. Fermilab has built a series of particle accelerators to produce and accelerate protons and anti-protons at very high speed (980 GeV proton $\approx c - 495km/h$), and Tevatron is the last process on this accelerator chain.

The history of Tevatron began in 1985, at beginning it operated as a 800 GeV fixed target accelerator. As the time passed by, Tevatron eventually developed to a proton-antiproton collider. The first physics run started in 1992, called Run I. Fermilab operated proton and anti-proton beams at 900 GeV in Run I, which stands for the total energy of the collision (a 900 GeV proton and a 900 GeV antiproton) at approximately 1.8 TeV. By the end of 1995, Run I ended with a total luminosity of 110 pb^{-1} physics data recorded on tape. The major achievement of Run I is the discovery of Top quark in 1995. Then in March 2001, Tevatron began the Run II with the higher beam energy 980 GeV, therefore the center-of-mass energy increased to $\sqrt{s} = 1.96$ TeV. Compared to Run I, Tevatron not only increased the beam energy, but also made a significant upgrade of the accelerator complex to increase the luminosity in Run II. The luminosity of Run I is limited by two technical reasons: The anti-proton production and the control of high intensity beams. Main Injector (MI) and the Recycler were built to solve these problems. At the moment of writing this thesis, Tevatron Run II has run 5 years and recently hit the mark of 1 fb^{-1} as total luminosity recorded on data disk.

The various components of the accelerator chain and their associated energies are listed in Table 2.1. The locations of these accelerators and storage rings are shown in Figure 2.1 and 2.2. We will give a brief introduction on these components in the following sections.

Machine	E-Injection	E-Extraction	Beam	Destination
Preacc	rest	750 KeV	p	Linac
Linac	750 KeV	400 MeV	p	Booster
Debuncher	400 MeV	8 GeV	$\bar{p}$	
Accumulator	8 GeV	8 GeV	$\bar{p}$	
Booster	8 GeV	8 GeV	p	Main Injector
Main Injector	8 GeV	120 GeV	$p, \bar{p}$	Switchyard, Accumulator
	8 GeV	150 GeV	$p, \bar{p}$	Tevatron
Tevatron	150 GeV	960 GeV	$p, \bar{p}$	Collision

Table 2.1: The components of the accelerator chain at Fermilab. The energy and destination of the beam depends on the operational mode of the accelerator.

2.1.1 Proton Source

The proton is produced by using an intense local electrostatic field to split the di-hydrogen molecule (H_2), and the outcome H^- anions are accelerated by a 750 KeV Cockroft-Walton machine. The continuous H^- ion beam is segmented into bunches, and accelerated by an 150-meter linear accelerator (LINAC) with 400 MeV. After leaving the LINAC the anions pass through a thin foil of graphite that tears apart the pair of electrons of each ion, it makes only proton and such the anion beam into a proton beam. This proton beam is delivered into a 475m long circular synchrotron (The Booster) that accelerates the protons to 8 GeV. And then the proton beam is transfered into the Main Injector (MI). The MI is used both for accelerating and injection the proton beam into the Tevatron, and for creating an intense proton beam used to produce anti-protons (Anti-proton will be discussed in next section). Before injection into the Tevatron, protons are accelerated up to 150 GeV within a few seconds.

2.1.2 Antiproton Production and Recycling

Antiprotons ($\bar{p}$) are produced by colliding a 120 GeV proton beam from the MI onto a 7 cm thick Nickel target. Roughly speaking, one antiproton is produced for every million proton collisions. Hence the interaction products need to be efficiently filtered in order to reject non-$\bar{p}$ particles. In the first step, charged particles are focused by a "lithium lens", a tubular piece of lithium traversed by a 650 kA current. Then a pulsed magnet vetoes positively charged particles and selects negative charge particles with a momentum of the order of 8 GeV. This process happens about every 1.5 seconds. For every 1 million protons that hit the target, only about twenty 8 GeV antiprotons survive.

After the non-$\bar{p}$ particles fallout, only $\bar{p}$ remains. The resulting $\bar{p}$ beam is de-bunched and focused further through betatron stochastic cooling and momentum cooling. Antiprotons are

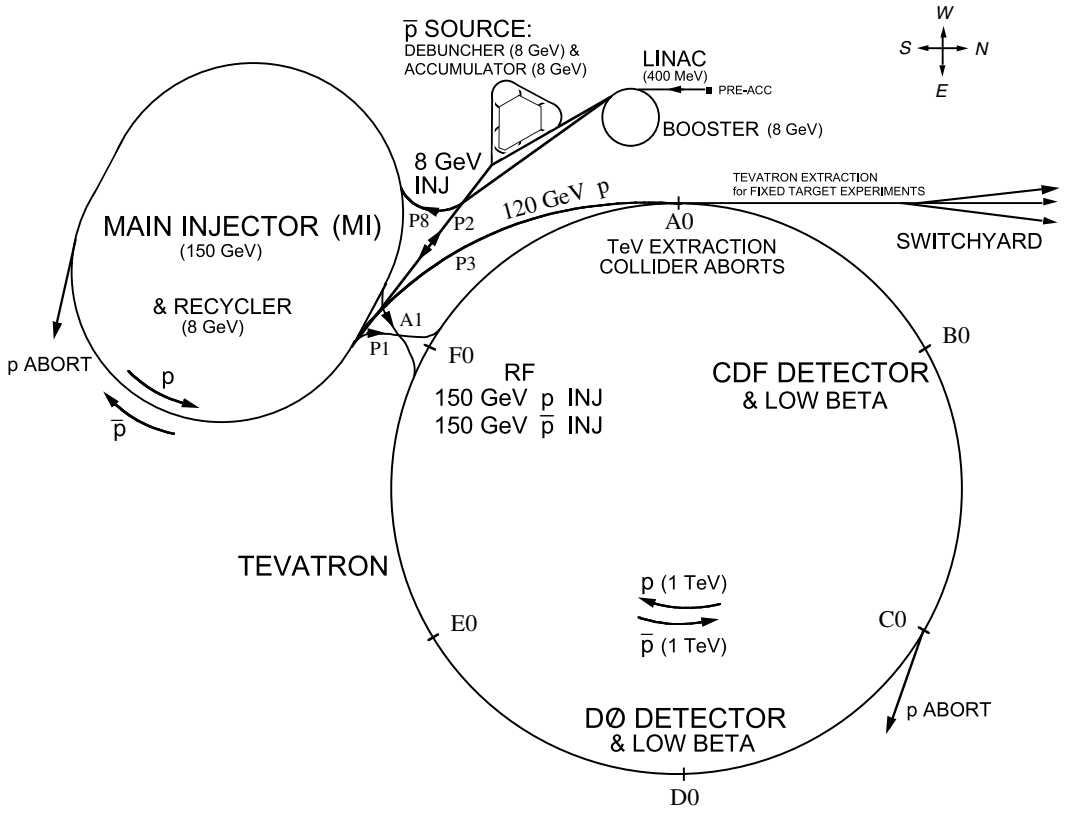

Figure 2.1: An aerial diagram of the Run II accelerator chain. Although the Run II Tevatron was designed to run at 1 TeV, the Run II nominal energy is 960 GeV. It is divided into 6 sectors divided by straight sections labeled A0 through F0. The CDF II is located at B0. [26]

stored into the accumulator, a set of concentric synchrotrons 80-meter long in circumference. Accumulation rates of the order of 10^{11} antiprotons per hour have been reached. Once enough antiprotons are accumulated (Typically 150 $\times 10^{10}$), they are transfered into the MI in the direction opposite to the protons, accelerated up to 150 GeV together with the proton beam, and delivered into the Tevatron.

Because $\bar{p}$ production is one the limiting factors in increasing the luminosity, the recycle was designed to recoup the antiprotons that remain in the Tevatron at the end of each store, and re-inject them in Tevatron for the next Tevatron collider store, together with a new stack of antiprotons from the accumulator. In the current operation however, the recycle is used as an extension of the accumulator: Antiprotons are transfered from the accumulator into the recycle, where the beam is cooled down before injection into Tevatron.

2.1.3 Main Injector

Before Run II, Fermilab used the Main Ring to inject the protons and antiprotons into the Tevatron. The Main Ring was the original 400 GeV proton synchrotron built during the early 1970s. However there existed many limitations on the performance since the Main Ring was not designed for this purpose. In Run II upgrade this Main Ring is replaced by Main Injector (MI). MI was built in 1998. It is a new rapid cycling accelerator designed for four major purposes:

- To accept the 8 GeV protons or antiprotons from the Booster, the antiproton accumulator and the Recycler.
- To Accelerate protons to 120 GeV and deliver them to the antiproton production target, fixed target area and NuMI beamline (for neutrino production).
- To accelerate p or $\bar{p}$ to 150 GeV and inject them into the Tevatron.
- To accept 150 GeV antiprotons from Tevatron and decelerate them to 8 GeV for transfer to the Recycler.

The MI parameters are listed in Table 2.2.

Circumference	3319.419 m
Injection Momentum	8.9 GeV/c
Peak Momentum	150 GeV/c
Minimum Cycle Time (@120 GeV)	< 1.5 s
Minimum Cycle Time (@150 GeV)	2.4 s
Number of Protons	3×10^{13}
Number of Bunches	498
Protons/Bunches	6×10^{10}

Table 2.2: Main Injector Parameter List.

2.1.4 The Accelerating and Storage Ring

The Tevatron is the final destination of the protons and antiprotons before collision. First, 150 GeV proton bunches are loaded from the Main Injector and into the Tevatron in 3 groups of 12 evenly-spaced bunches. Next, the antiprotons are sent from the Accumulator back into the Main Injector where they are accelerated from 8 GeV to 150 GeV. The antiproton bunches are loaded one bunch at a time into the Tevatron to make another 3 groups of 12 evenly spaced bunches. The Tevatron Ring then accelerates the bunches to an energy of 980 GeV.

The Tevatron ring features 1000 cyrogenically cooled super conducting magnets and is approximately 6 km in circumference. The ring is divided into six sectors labeled A through F. Each sector has straight sections which are serviced by buildings labeled "0". Their locations are shown in Figure 2.1. The proton and antiproton bunches are allowed to cross paths at the B0 and D0 points where particle detectors are positioned. The bunches are spaced such that there are 36 bunches crossings every 396 ns. This crossing time impacts the design of the electronic triggering system, which is discussed in Section 2.3. The Tevatron ring essentially stores the proton and antiproton beams while they are allowed to collide at the D0 and B0 points. The store ends when another batch of antiprotons is ready or the beam is aborted due to malfunction.

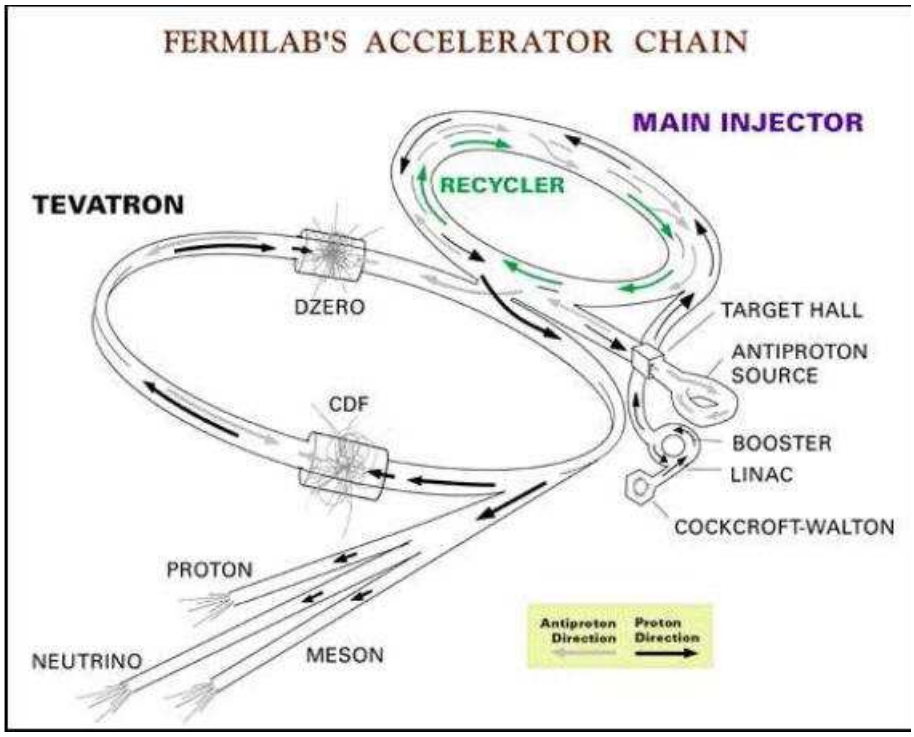

Figure 2.2: Fermilab Accelerator Chain

2.2 The Run II Collider Detector at Fermilab

The Collider Detector at Fermilab Run II (CDF II) is a general purpose soleniodal detector, which consists of precision charged particle tracking system, fast projective calorimeters, fine grained muon detectors, a Time-of-Flight system, a Cherenkov Luminosity Counter and related front-end readout electronics.

The detector is located along the B0 straight section of the Tevatron ring. An elevation view about CDF II is shown in Figure 2.3. Tracking systems are contained in a superconducting solenoid, 1.5 m in radius and 4.8 m in length, which generates a 1.4 Tesla magnetic field parallel to the beam axis. Calorimetry and muon systems are all outside the solenoid.

The Tevatron beam line goes through the detector, and the interaction point, which serves as the coordinate system origin, is at the center of the CDF. The positive z-axis is defined to be collinear with the beam-line and pointing along the direction of the proton beam (EAST) (So protons move in the positive direction, and antiprotons move in the negative one). The y-axis points directly up and the x-axis points outward (NORTH) from the center of the detector ring. We use a coordinate system where the polar angle θ is measured from the proton direction, the azimuthal angle ϕ is measured from the Tevatron plane, and the pseudo-rapidity is defined as $\eta = -\log\ \tan(\frac{\theta}{2})$. The transverse component of a particle's energy and momentum is defined by the angle of the particle's track in the $y-z$ plane with respect to the beam position, i.e. $p_T = p\sin\theta$ and $E_T = E\sin\theta$ where p and E are the particle's momentum and energy respectively.

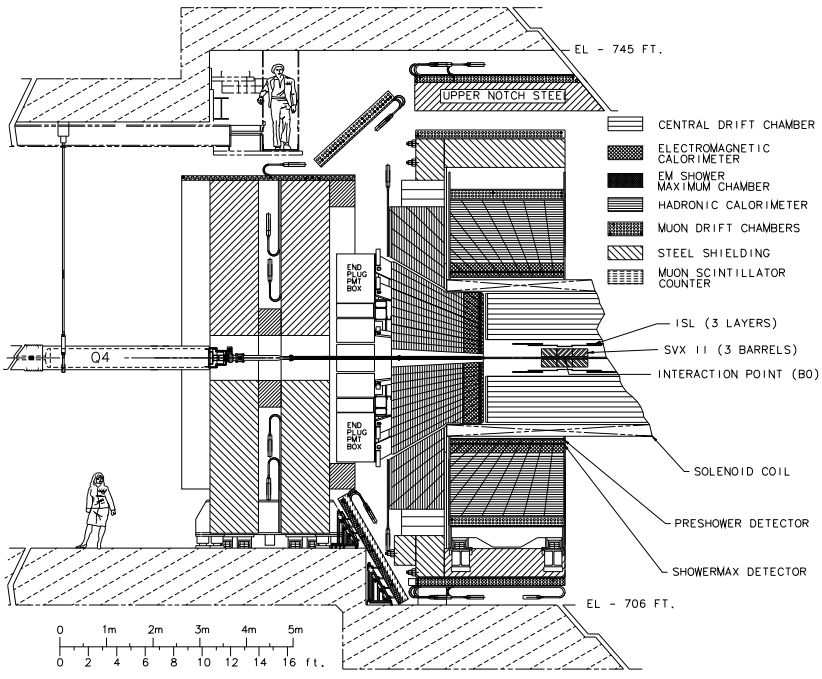

Figure 2.3: A cross section schematic of the CDF II detector [47].

CDF has gone through periods of extensive upgrades. The CDF II we see today is totally different to the one in Run I. Most components have been entirely replaced with new hardware and triggering systems. Quoting from CDF Run II completion report:

Collider Run IIa began in 2001, the running conditions for collider Run II specified that the detector must be capable of handling peak luminosity up to $2 \times 10^{32} cm^{-2}\ sec^{-1}$, bunch spacing as small as 132 ns, and an integrated luminosity of 2 fb^{-1}. The CDF Run IIa upgrade included replacing the plug and forward gas calorimeters with a new scintillator-based calorimeter and replacing the Central Tracking Chamber with a device with shorter drift time to allow tracking in a high-luminosity environment. A completely new silicon system was built and installed. The front-end electronics and trigger systems were upgraded to accommodate data-taking at higher rates and with shorter bunch spacing. Muon detection systems were upgraded to increase acceptance and allow the electronics to work with shorter bunch spacing. The data acquisition system was upgraded to increase throughput and reliability. A new time-of-flight detector was added, as were new detectors in the forward region. The CDF Upgrade Project for Run IIa was successfully completed in March 2001.

The Run IIb CDF Detector Project was submitted in December 2002 for the purpose of extending the useful life of the CDF detector to instantaneous luminosities of $3 \times 10^{32} cm^{-2} sec^{-1}$ with 396 ns crossing separation) and an integrated luminosity of 15 fb^{-1}. The integrated luminosity requirement was revised to 8 fb^{-1} during the construction of the project, and the technical scope was adjusted accordingly. The project that remained after this change included upgrades to the data acquisition to accommodate the high event rate, upgrades to the track triggers to address the complexity of the events seen at high luminosity, and upgrades to the calorimeter system that replaced gas chamber systems with scintillator.

In short, CDF Run II upgrades accommodate higher luminosities. With improved read-out and triggering electronics, the bunch-crossing times becomes shorter and the performance of detector is better compared to Run I.

The main features of the detector systems are summarized in following sections and described in greater details in CDF II Detector Technical Design Report (Run IIa [47], Run IIb [48]).

The Detector Components

The cutaway view of CDF is shown in Figure 2.4, the inner cutaway view is shown in Figure 2.5.

- SVX: Silicon Vertex Detector

  Purpose: High-precision tracking and secondary vertex detection at inner radii.

- L00: Layer 00

  Purpose: Improved precision of track measurements and tagging efficiency, Layer 00

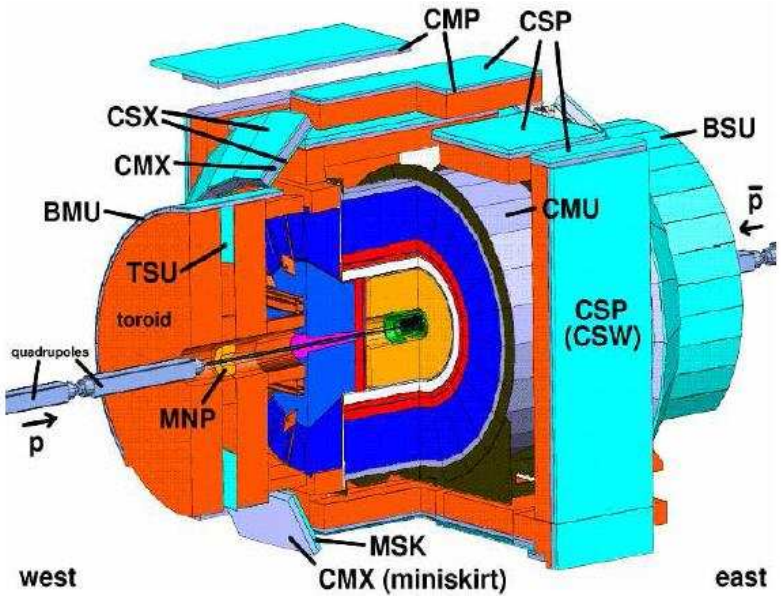

Figure 2.4: Cutaway view of CDF II.

also serves as insurance against the loss of the innermost of SVX II (layer 0) to radiation damage.

- ISL: Intermediate Silicon Layer

  Purpose: In the central region, provides enhanced linking of tracks between SVX II and COT. In the plug region, where COT coverage is incomplete, provides improved silicon-only tracking capabilities.

- COT: Central Outer Tracker

  Purpose: Central-purpose tracking in the central region of the detector.

- TOF: Time-of-Flight Detector

  Purpose: Provides Time-of-Flight information to enhance particle identification abilities in the central detector, especially for improving $K - \pi$ discrimination.

- Solenoid

  Purpose: Provides the magnetic field for tracking in the central detector region.

- CEM: Central Electromagnetic Calorimeter

  Purpose: Energy measurement of electromagnetic showers in the central region.

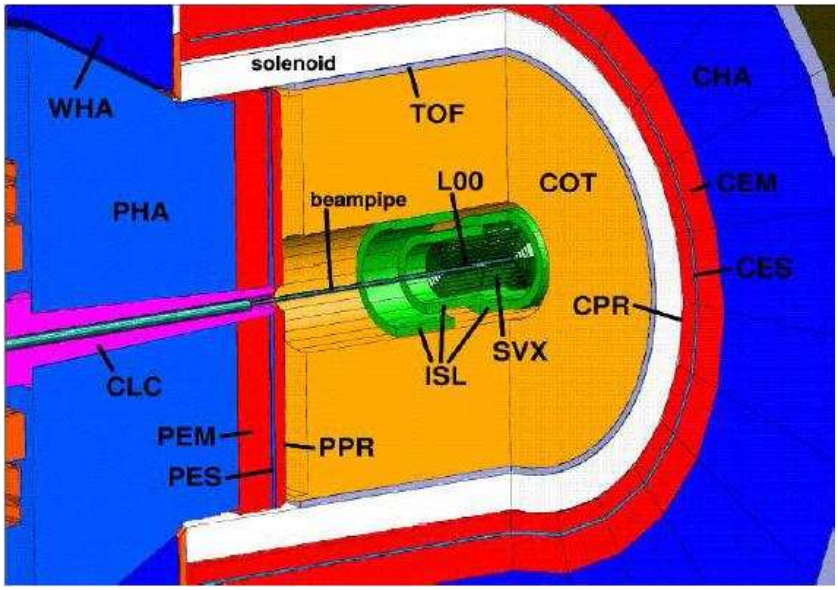

Figure 2.5: Inner cutaway view of CDF II.

- CHA: Central Hadronic Calorimeter

  Purpose: Energy measurement of hadronic showers in the central region.

- WHA: End-wall Hadronic Calorimeter

  Purpose: Extension of hadronic calorimeter coverage to the end-wall region.

- CES: Central E-M ShowerMax Chamber

  Purpose: High-precision position measurements at shower maximum to provide track linking ability and transverse shower profiles to improve particle identification.

- CPR: Central Pre-Radiate Chamber

  Purpose: Preshower measurements for enhanced discrimination between electrons and pions, and improved photon measurements.

- CCR: Central Crack Chamber

  Purpose: To provide some coverage for particles which would otherwise fall into the gaps between calorimeter wedges.

- PEM: Plug Electromagnetic Calorimeter

  Purpose: Energy measurement of electromagnetic showers in the plug region of the detector.

- PHA: Plug Hadronic Calorimeter

  Purpose: Energy measurement of hadronic showers in the plug region of the detector.

- PES: Plug Electromagnetic ShowerMax Detector

  Purpose: Like CES, provides precision measurements of shower positions and improved ability to separate electrons, pions and photons.

- PPR: Plug Pre-Radiate Detector

  Purpose: Like CPR, provides enhanced ability to discriminate between electrons and pions.

- CMU: Central Muon Chambers

  Purpose: Detection of muons in the central detector region.

- CMP: Central Muon Upgrade

  Purpose: Confirmation of CMU tracks. Since CMP is behind more material,CMP hits have a higher signal-to-background ratio and increase the trigger efficiency of the CMU/CMP combination.

- CMX: Central Muon Extension

  Purpose: Extension of central muon coverage to $\eta = 1.0$.

- BMU: Barrel Muon Chambers

  Purpose: Muon detection in the forward region.

- Toroids

- CSP: Central Scintillator Upgrade

- CSW: CSP Wall Scintillators

  Purpose: Fast timing and trigger counters for CMU/CMP muons.

- CSX: Central Scintillator Extension

  Purpose: Fast timing and trigger counters for CMX muons (in the conical section).

- MSK: CMX Miniskirt Scintillators (same as MSX)

  Purpose: Fast timing and trigger counters for CMX muons (in the miniskirt section)

- BSU: Barrel Scintillator Upgrade

  Purpose: Fast timing and trigger counters for BMU muons.

- TSU: Toroid Scintillator Upgrade

  Purpose: Additional triggering powers for forward muons.

- CLC: Cerenkov Luminosity Counters

  Purpose: Luminosity measurement of the beams at CDF

- Beam pipe

- MNP: Miniplug

  Purpose: Measurement of diffractive events and far forward particles.

- BSC: Beam Shower Counters

  Purpose: Measurements of diffractive events, also provides beam loss information.

- RPS: Roman Pot Spectrometer

  Purpose: Measurement of diffractive events.

2.2.1 Tracking System

When charged particles travel through the matter, they will lose their energy for ionizing atoms and molecules of the media nearby their trajectories. CDF II tracking system is able to record and reconstruct these trajectories — People usually call them tracks. To reconstruct the tracks of particles is called tracking.

The tracking system in CDF II is composed of two main parts: The Silicon Vertex Detector (SVX) and the Central Outer Tracker (COT). There are also two additional parts in CDF II tracking system as the part of Run II upgrade plan: The Intermediate Silicon Layor (ISL) and Layer 00 (L00). Figure 2.6 shows the schematic view of the CDF tracking volume in the $r - z$ plane. From inner beampipe to outside layer the location order is L00, SVX, ISL and then COT.

The L00 and ISL were introduced in Run II. Together with the SVX they comprise the CDF II silicon tracking system, shown in Figure 2.7.

The L00 is a silicon detector inside the SVX. It consists of 6 narrow and 6 wide groups of the micro-strip detectors, called "wedges". Six of them are placed at radius of 1.35 cm and the other six are at the radius of 1.62 cm. There are 6 modules along the z axis with a total length of 95 cm. Sensors in L00 are single-side and made of more light-weight and radiation-hard silicon than the SVX. They are mounted on a carbon-fiber support for tracks passing through the high-density SVX material. This make a resolution of impact parameter d_0 as small as 25 μm.

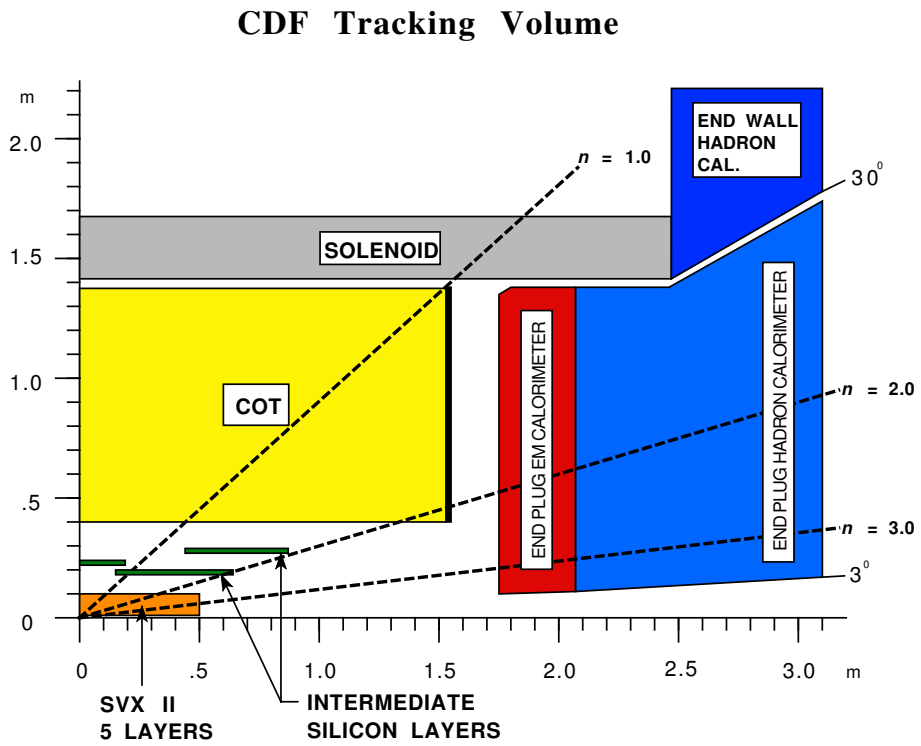

Figure 2.6: A cross section of one quadrant in the $r-z$ plane of the CDF II tracking volume [47].

The ISL consists of three separate silicon layers outside of SVX, extending in overlapping regions of η. A single ISL layer covering $|\eta| < 1$ is positioned 22 cm from the beam line. Two more layers are positioned at a radii 20 and 28 cm and cover the region $1.0 \leq |\eta| \leq 2.0$. The layers consists of the double-sided silicon micro-strip detectors, and the readout electronics are identical to the SVX. ISL improves the tracking in the central region. In fact L00, ISL and SVX are capable of providing standalone tracking in the region $1.0 \leq |\eta| \leq 2.0$.

The function of SVXII [45] is to determine a precise position of the secondary vertexes. It consists of 5 layers of a combination of 90-degree and small-angle (1.2^o) stereo layers of double-sided silicon sensors, also called "wafers". The entire SVX detector is composed of 3 barrels covering a total z-distance of 96.0 cm, or $|\eta| \leq 2.0$, which is roughly twice as long as the SVX detector in Run I. The 5 silicon layers cover a radial distance of 2.4 to 10.7 cm from the beam line. The SVX detector is capable of a resolution of 12 μm. In order to suppress the creation of secondary particles and reduce multiple scattering, the amount of material used to construct the SVXII was kept to a minimum, approximately 3.5 radiation lengths (X_0). In all there are a total of 405,504 channels in the system which are connected to readout chips which have been radiation hardened. Due to the length of the barrels,

the readout speed and capacitance limitations, the readout chips are located close to the silicon sensors and within the active volume of the detector. The consequence is a reduction in resolution of the $r\phi$ impact parameter. Layer 00 is mounted on the beam-pipe just to compensate for this effect.

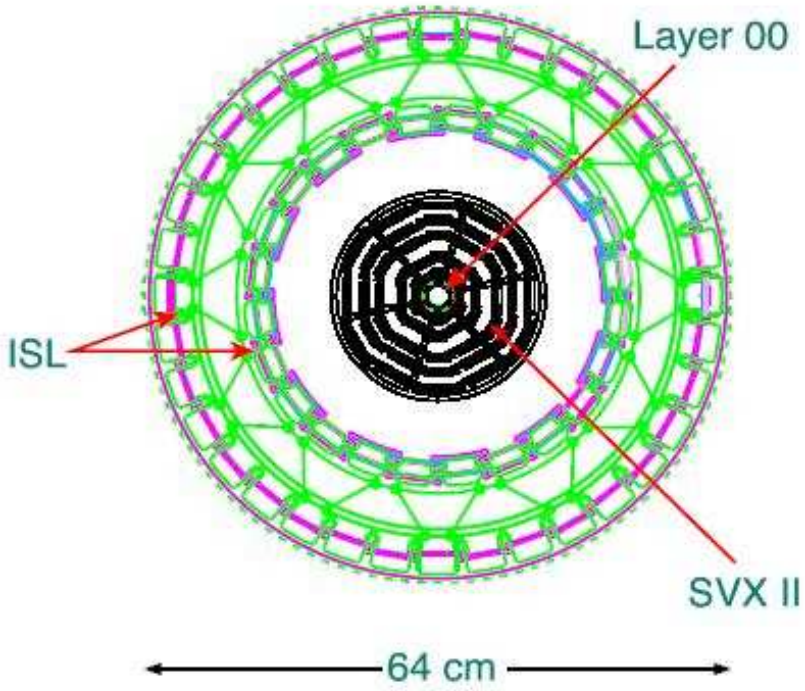

Figure 2.7: The side view of L00, SVX and ISL system

The Central Outer Tracker (COT) is an cylindrical open-cell drift chamber. In CDF II it is used to detect charged particles [31] (Like the role of the Central Tracker Chamber (CTC) in Run I). It encloses the SVX and ISL by extending radially from 44 to 132 cm and has an effective pseudo-rapidity tracking region of $|\eta| \leq 1.0$. It is filled with a fifty to fifty mixture of Argon and Ethane plus trace amounts of alcohol. The information about the particle tracks is obtained from the wires. Each drift cell comprises 12 alternating sense and shaper wires running down the middle of two gold-on-mylar cathode planes separated by about 2 cm (Figure 2.8) [47].

The ends of the wires are strung between two precision-milled end-plates giving a wire tension of 135 g. There are a total of 96 layers of drift cells divided into 8 "super-layers" which alternate between 4 axial and 4 stereo super-layers. The axial super-layers run parallel to the beam line whereas the stereo super-layers alternate in tilt by $\pm 3^o$ with respect to the beam line. The stereo super-layer geometry makes track reconstruction in the $r - z$ plane

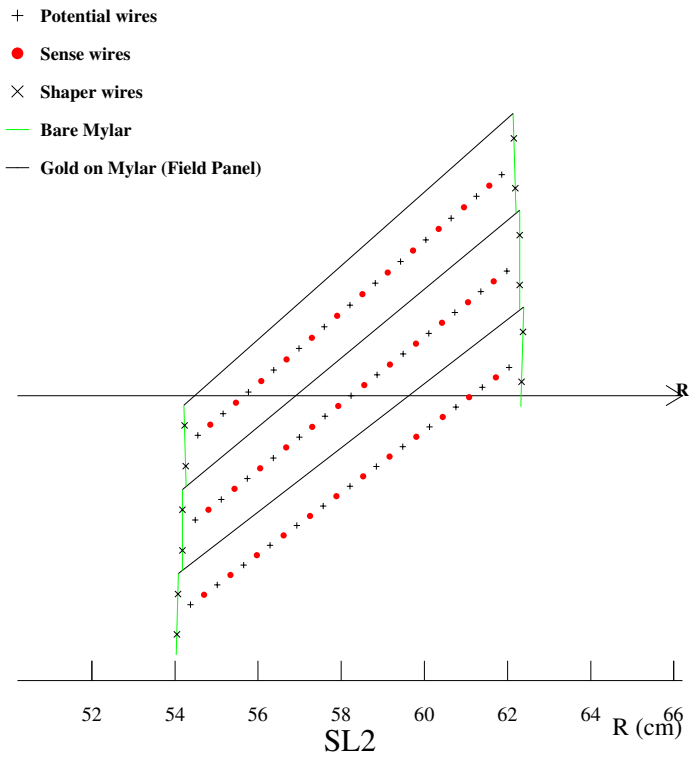

Figure 2.8: A cross section of several COT drift chambers. The wires alternate between sense wires and potential wires. The arrow shows the relative direction of the nominal beam position [47].

possible. Due to the solenoid's large magnetic field, the drift cells are oriented at a 35^o degree angle in the $r - \phi$ plane (Figure 2.9) to accommodate drift trajectories in the ϕ-direction and to optimize for track measurements transverse to the beam line. A gas with a higher drift velocity and smaller drift cells with respect to the CTC drift cells of Run I have made the COT capable of maximum drift times of 100 ns and a resolution of 140 μm [8]. The COT is currently operating very well in Run IIa and will be retained in Run IIb.

2.2.2 Calorimetry

Calorimeters have played a key role in the CDF II by measuring electron and photon energies, jet energies, and net transverse energy flow. Two layers of calorimeters are built in CDF calorimetry system. The inner layer is for electromagnetic towers, hadronic towers are located behind EM towers and pointing back to the $p\bar{p}$ interaction region. Both EM and Hadronic types are *sampling* calorimeters since they have a similar structure — Multiple

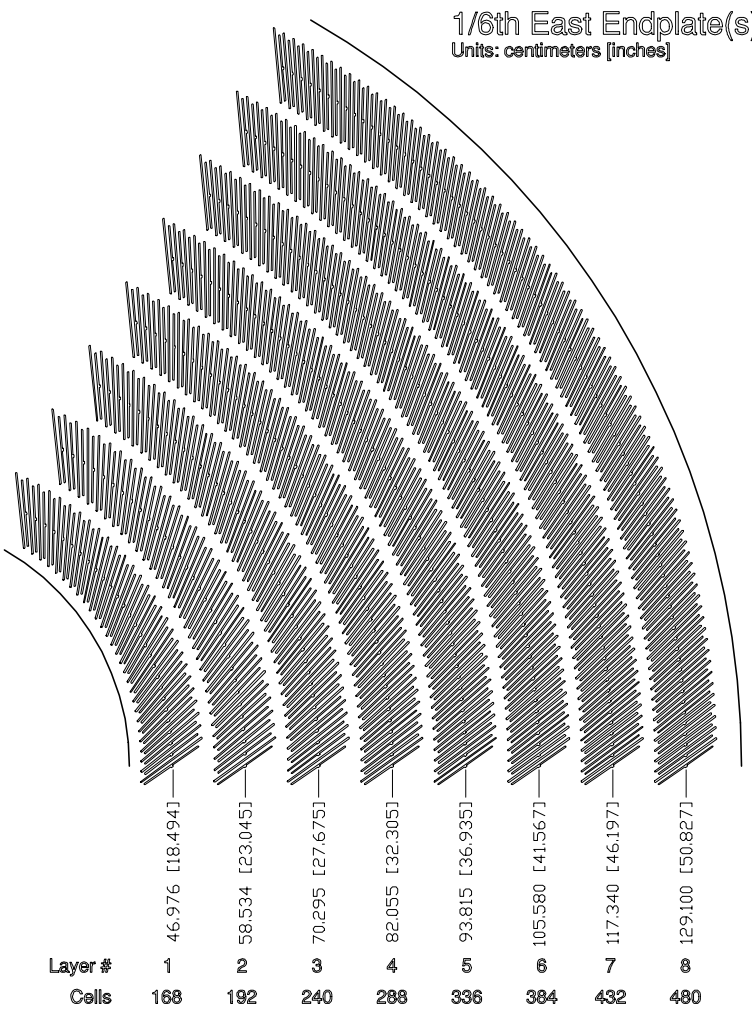

Figure 2.9: The east end-plate showing the field planes of the COT cells. The numbers represent the radial distance from the beamline in centimeters[inches].

layers of scintillator tiles are sandwiched between sampling material used to absorb the incoming particle energies. The only difference is EM calorimeter uses lead as sampling material while the hadronic uses iron and steel.

The third-generation scalar leptoquark search covers almost every physics object involved in calorimetry: Electrons, jets and missing transverse energy (neutrinos).

When a energetic electron passes into the absorber material of the electromagnetic calorimeter, the absorber feels a high electric field inside the atoms. The force on the electron from the electric field causes the electron to change direction which causes it to emit a virtual photon (so that total energy and momentum are balanced). The virtual photon has sufficient energy and momentum that it produces a e^+e^- pair. These particles have

high momentum and travel roughly parallel to the direction of the initial electron. Each of the electrons, positrons or photons produce further pairs as they pass through the high field regions of atoms. This process repeats itself and eventually cascade or "shower" of electrons and positrons develops. In the end there is not enough energy to form any more pairs and all the electrons and positrons are absorbed by the material of the calorimeter.

Muons have exactly the same interactions as electrons. However, the behavior of high-energy muons as they go through matter is quite different from electrons. The reason is that the muon is about 210 times more massive than the electron, and the force on it from the electric field is the same because the charge on it is the same as electron. That force is not large enough to cause the muon to change direction significantly. Therefore muons are known as minimum ionizing particles (MIP's). The characteristic of a MIP-like particle is one criterion used in identifying muons and becomes especially important in the case that a muon passes undetected through the muon detectors.

Hadrons (jets) are much more massive than electrons, they are not significantly deflected by the atomic electric field. However, they have strong interactions so they interact with the material in both the electromagnetic and hadronic calorimeters to produce a different type of shower. The released jet energies are measured by the scintillator tiles which are embedded with wavelength shifting sheets or fibers. These fibers then carry the light to photomultiplier tubes (PMT's) located outside of the sensitive detector volume. There is no way to distinguish between jets from photons and hadrons, however electrons are distinguishable by their large ratio of electromagnetic to hadronic energy. The calorimeter gains are initially calibrated from test beam data and are retained by calibrations carried out between runs via xenon flashers and LED sources.

As for neutrinos, since they don't interact with matters, they will pass through the detector without losing their energies. Thus neither calorimetry system nor other components of CDF II can do any direct energy mesurement on neutrinos. They are regarded as "undetected" physics objects and are reconstructed only in the sense of the missing transverse energy, $\not\!\!E_T$. CDF use this presentation for neutrinos because $p\bar{p}$ beam comes through the z axis, each collision happened in CDF is assumed to have zero transverse momentum at beginning. And by the conservation law of energy, the total vector sum of transverse energy in a physics event should keep as zero during the whole process. If neutrinos carry their energies and fly away without being detected, they will cause an imbalance of transverse energy (so the sum of transverse energies are not equa to zero) in the event. The reconstructed $\not\!\!E_T$ objectrepresents the direction and energy of the neutrino's trajectory in the $r-\phi$ plane. The calculation of the neutrino transverse energy is discussed further in Section 3.7.

The calorimetry detectors in CDF are mechanically subdivided into three regions: Central, Wall and Plug (in order of increasing pseudo-rapidity). By the region people in CDF

(a.k.a. "Gurus") usually name these calorimeters as CEM (Central Electro-Magnetic), CHA (Central Hadron), WHA (Wall Hadron), PEM (Plug Electro-Magnetic) and PHA (Plug Hadron).

The central parts cover the region $|\eta| < 1.1$ for EM and $|\eta| < 1.3$ for the hadronic calorimeters. They are divided into towers with equal size 15^o in ϕ and 0.1 in η. The plug calorimeters extend the η down to 3.6 and have various segmentations.

The CEM uses lead sheets interspersed with scintillator as the active medium and employs phototube readout, around 19 X_0 in depth (X_0 is defined as the radiation length which is the mean distance for the $e^{\pm}$ to lose 1/e of its energy). The energy resolution for CEM is $13.5\% \oplus 2\%$ [9], where $\oplus$ denotes addition in quadrature. The first layer of CEM is called pre-shower detector (CPR) and readout separately. A shower-max detector is located approximately $6X_0$ deep into the CEM. Figure 2.10 shows a schematic of one CEM wedge.

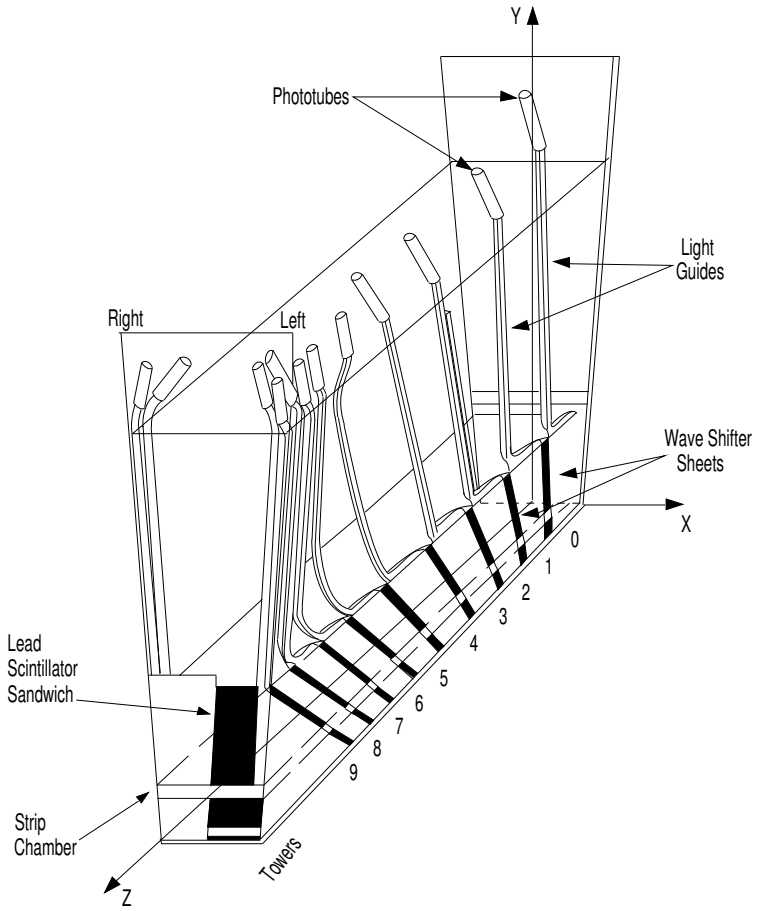

Figure 2.10: A schematic of a CEM wedge [47].

The CES uses proportional strip and wire counters in a fine-grained array, as shown in 2.11. CES provides precise position ($\pm 2mm$ resolution at 50 GeV [11]) and shape information for electromagnetic cascades.

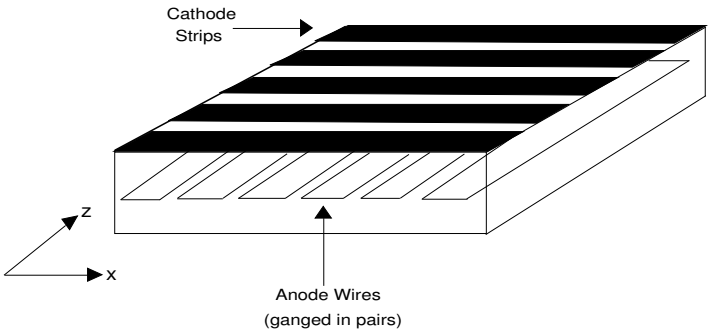

Figure 2.11: A schematic of a CES wedge [47].

The CHA and WHA use steel absorber interspersed with acrylic scintillator as the active medium. They are approximately 4.5 λ in depth, and have an energy resolution of $75\%/\sqrt{E}\oplus$ 3% [12].

The plug calorimeters consist of PEM and PHA. At about 6 X_0 in depth in PEM is PES. The PEM is a lead-scintillator sampling calorimeter. It is approximately 21 X_0 in depth. PEM has an energy resolution of $16\%/\sqrt{E} \oplus 1\%$ [13]. The PES is composed of two layers of scintillator strips: U and V layers offset from the radial direction by $+22.5^o$ and -22.5^o respectively. PES provides position information in the $r - \phi$ plane. The resolution of the PES is about $\pm 1mm$. PHA is located behind PEM, it is a steel-scintillator sampling calorimeter. It is about 7 λ in depth, and has an energy resolution of $74\%/\sqrt{E} \oplus 4\%$.

2.2.3 Muon Detectors

As mentioned in last section, muons have no hadronic interaction, thus they don't lose much energy in calorimeters by ionizing the atoms or molecules when passing through the matter. Due to the muon's long lifetime and penetrating ability, the muon detectors are positioned in the outermost regions of CDF II.

CDF uses four systems of scintillators and proportional chambers for muons detection with the region of $|\eta| < 2$. They are:

- CMU: Central Muon detector
- CMP: Central Muon Upgrade

- CMX: Central Muon Extension
- IMU: Intermediate Muon detector

The muon chambers in the CMP and CMX are placed together with scintillators, which are used to suppress the backgrounds coming from the interactions in the beampipe material. The scintillator systems are called CSP and CSX, respectively. Figure 2.12 shows each muon detector coverage in the $\eta - \phi$ plane. In this analysis only CMU, CMP, and CMX are used. IMU is a new system for Run II which is not included in the dataset we used for this analysis.

Individual muon candidates are detected in the muon chambers from the track segment they leave. The track segment is called a *muonstub*. Having a stub does not guarantee a muon event, because a stub can be due to a hadronic punch-through or just noise in the electronics. If a stub matches a certain track measured by the COT of silicon tracking system the the two elements are combined to make a muon. A muon's momentum is determined by its track curvature through the CDF II tracking volume. The radius of curvature for muons is very slight due to their relatively large masses. Thus, to improve muon momentum resolution, their tracks are often constrained to originate from the beam-line or from a track segment in the silicon detector.

Table 2.3 summarizes the mechanical/technical information of muon detectors used in this analysis, we also give a brief introduction on individual muon detector in the following subsections. For more design and performance details please refer to CDF Technical Design Report [47] (1996) and [48] (2002).

	CMU	CMP	CMX
Pseudorapidity coverage	$\lvert\eta\rvert \leq\sim 0.6$	$\lvert\eta\rvert \leq\sim 0.6$	$\sim 0.6 \leq \lvert\eta\rvert \leq\sim 1.0$
Drift tube cross-section	2.68 x 6.35 cm	2.5 x 15 cm	2.5 x 15 cm
Drift tube length	226 cm	640 cm	160 cm
Maximum drift time	800 ns	1.4 μs	1.4 μs
Scintillation counter thickness		2.5 cm	1.5 cm
Total counters		269	324
Pion interaction lengths	5.5	7.8	6.2
Minimum detectable muon p_T	1.4 GeV/c	2.2 GeV/c	1.4 GeV/c
Multiple scattering resolution	12 cm/p	15 cm/p	13 cm/p

Table 2.3: Design specifications of the CMU, CMP, and CMX detectors

CMU: Central Muon Detector

The Central Muon detector is placed outside of the hadronic calorimeter at the radial 347 cm. It covers the pseudorapidity region $\lvert\eta\rvert \leq\sim 0.6$ [67][68]. Only the muons with p_T

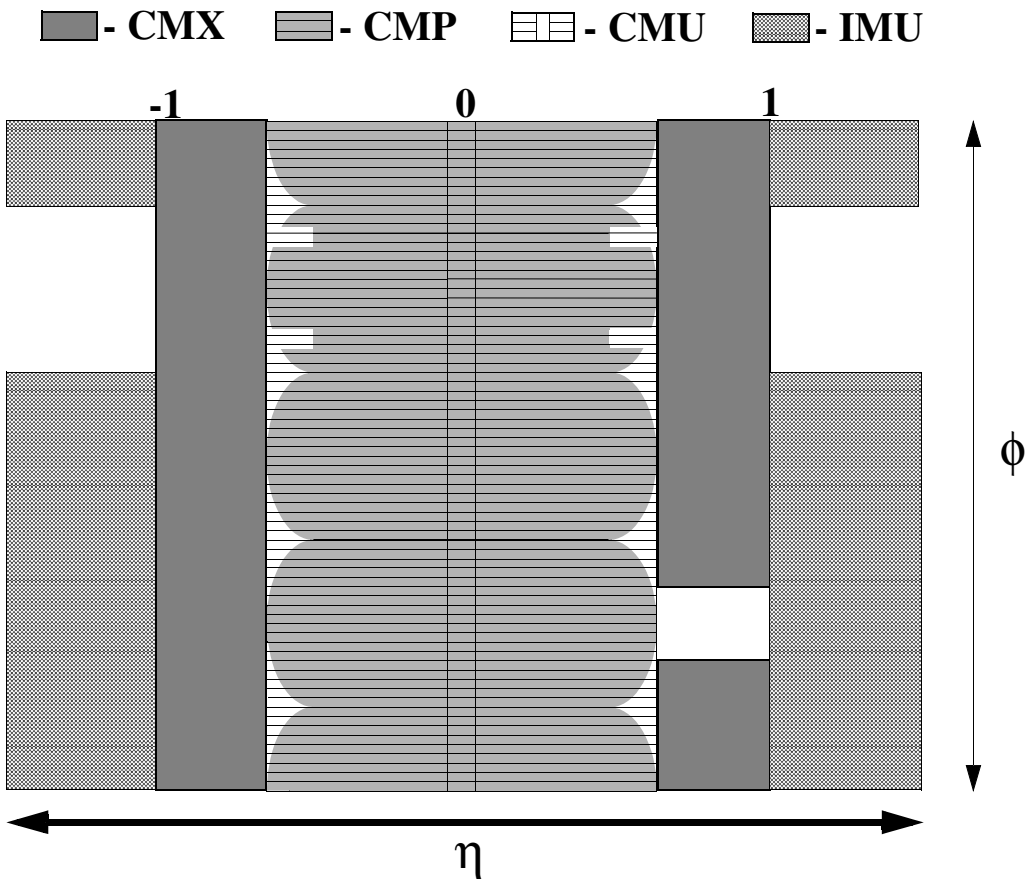

Figure 2.12: Location of the muon detector elements in the $\eta - \phi$ plane. The solid bands show the Run II coverage upgrades [47].

greater than about 1.4 GeV/c can reach the CMU. CMU is segmented in ϕ into 24 wedges, each one of which covers 15^o. The working part of the wedge covers 12.6^o, so that CMU has 24 gaps with 2.4^o each. CMU is also divided into East (positive z) and West (negative z) halves with about 18 cm gap entered at z = 0 between the two,

A wedge consists of three chambers of angular coverage 4.2^o. Each of them is composed of four layers of four rectangular drift cells as shown in Figure 2.13. The cells are filled with same Argon-Ethane gas mixture as the COT. The voltage on the aluminum cathodes of the cell layer is $\tilde{2}500$ V, while the stainless still sense wires are kept at +2325 V.

Two of the four cell layers are oriented along a radial plane passing through the z axis, while the other two are laid along the parallel plane. They are stacked in the way that there is a 2 mm ϕ-offset between the first/third and second/fourth layers. The offset resolves track ambiguity in the azimuthal dimension by determining which of the 2 sets of sense wires were

hit first. The z position of the hit on a sense wire is determined from the charge division between the ends of the wire. The resolution in the CMU chambers is about 250 μm in the $r - \phi$ plane and about 1 mm in z.

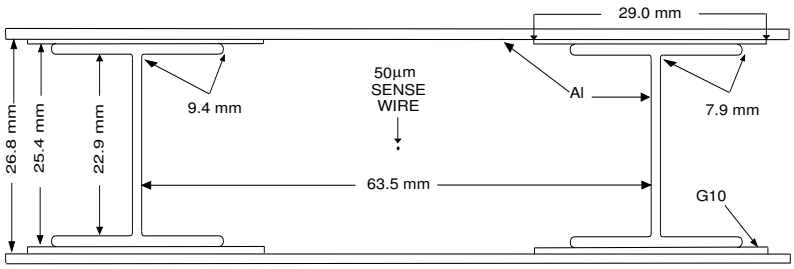

Figure 2.13: A schematic of a CMU drift cell [47].

CMP: Central Muon Upgrade

The Central Muon Upgrade covers the central region of the detector as well as CMU, but it also covers the CMU's gap in ϕ. The CMP is located behind the CMU and shielded by an additional steel absorber. This absorber is used to reduce hadronic punch-through contamination which the CMU suffers from. The path of the muons is effectively increases by this absorber from 5.5 to 7.8 hadron interaction lengths. Only the muons with p_T greater than 2.2 Gev/c can reach CMP.

As the second set of single wire drift chambers, CMP walls have four layers of rectangular single-wire drift tubes. CMP chambers are filled with the same gas mixture as COT. A 50/50 mixture of Argon-Ethane gas bubbled through a -5^oC bath of isotropy alcohol, with a maximum drift time of about 1.4 μs.

CMP chambers are mounted directly on the absorber. They consist of single wire tubes with 2.5 cm $\times$ 15 cm $\times$ 640 cm. Some of them are a little bit shorter to allow the cables from the inner parts of the detector go outside. The drift tubes are organized into four layers with each layer being shifted by a half-size of the tube with respect to neighboring layers.

A layer of rectangular scintillation counters (the CSP) is located outside of the CMP drift chambers. The dimension of a single scintillator is about 2.5 cm $\times$ 15 cm $\times$ 320 cm,

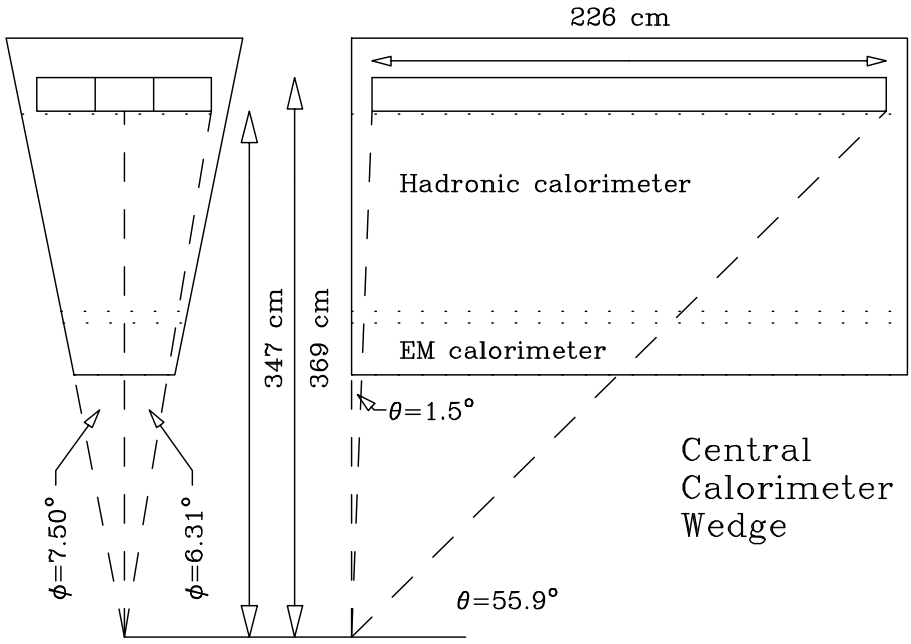

Figure 2.14: A schematic of an entire CMU module [47].

whose length is as half as a single chamber. CSP is read out by single phototubes. These phototubes are located at the center of a CSP array and are displaced away from the wall to allow inter-leaving of the phototubes. This assignment saves the space occupied by the light-guide and photomultiplier tube assembly.

An illustration of the configuration of steel, chambers and scintillators are shown in Figure 2.16. The counters provide precise timing for track matching and beam crossing identification.

CMX: Central Muon Extension

The Central Extension consists of the wedges forming a conical shapes on both ends of the detector. Each wedge covers 15^o in ϕ and the range $0.65 < |\eta| < 1.0$. The rectangular drift tubes are arranged such that their sense wires point radially toward the beam-line. CMX chambers are same as CMP tubes except a different length as 180 cm. Each wedge in the CMX has 48 tubes, with 8 layers arranged and each layer has 6 tubes. The layers are staggered so that there are at least 4 tubes in any coverage in ϕ. Layers are also placed at a slight stereo angle, which provides an available measurement on z coordinate.

In Run I CMX had a 30^o gap at top on the west gap and a 90^o gap at the bottom in both East and West ends. The first gap was created to make space for the liquid helium lines and the second gap was due to intersection of the conical section with the collision hall

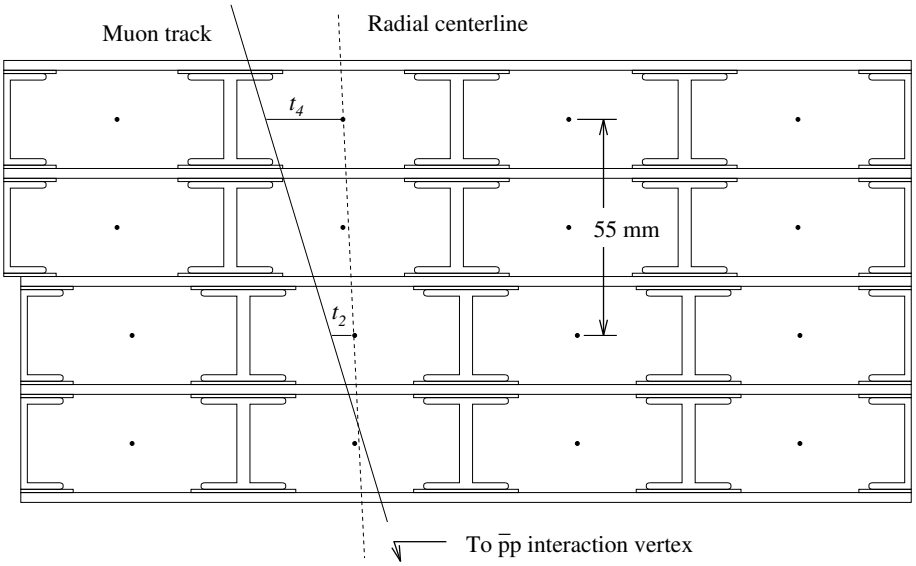

Figure 2.15: A schematic of an entire CMU module [47].

floor. For Run II both gaps are covered by KeyStone and MiniSkirt additions to CMX. The KeyStone consists of two more CMX wedges, while MiniSkirt has a slight different geometry, shown in Figure 2.17.

2.2.4 Luminosity Counters

The Cherenkov Luminosity Counters (CLC) measures the average number of the interactions per bunch crossing number N_{BC}. The instantaneous luminosity L is determined by:

$$L = \frac{N_{BC} \cdot f_{BC}}{\sigma_{p\bar{p}}} \tag{2.1}$$

where f_{BC} is the rate of the bunch crossing at the Tevatron and $\sigma_{p\bar{p}}$ is the total $p\bar{p}$ cross section at $\sqrt{s} = 1.96$ TeV.

The working principle of CLC is known as the effect of Cherenkov radiation: When a charged particle passes through an insulator at a speed greater than the speed of light in that medium, it will emit electromagnetic radiation into a cone along with the particle trajectory. The opening angle of this cone depends on the ratio of speed of moving particle and speed of light, also depends on the refraction index of the medium. (A side note: The velocity of light that must be exceeded is the phase velocity rather than the group velocity, therefore we are not violating the relativity here)

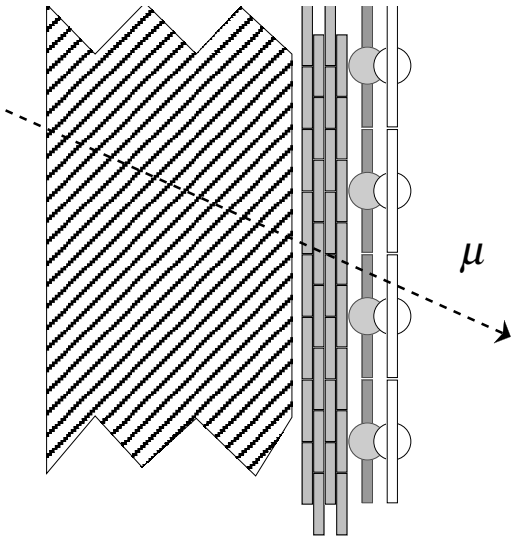

Figure 2.16: An illustration of the configuration of steel, CMP chambers and CSP scintillators looking in the z-direction. A muon track is drawn to indicate the interaction point. The two layers of scintillation counters are overlapped in the z-direction.

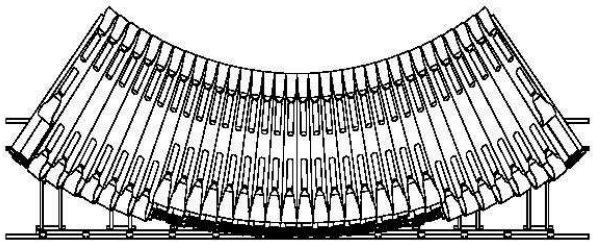

Figure 2.17: The MiniSkirt portion of the CMX system.

The CLC's are located within the 3^o cavities enclosed by the end of plug calorimeters on the east and west sides of the central detector through which the beam-pipe extends. Such arrangement makes CLC to be the most sensitive to the particles coming directly from the interaction point. This is because particles coming from interaction point have a longest flight path in the gas of the counter, therefore the amount of radiation light they produced is the largest.

The CLC is designed to perform reliably at a peak instantaneous luminosity of 2×10^{32} $\mathrm{cm}^{-2}\mathrm{s}^{-1}$ and has a timing resolution of $\sigma < 100$ ps which is roughly a factor of 2 better than the scintillator counters used in Run I. CLC in Run II is capable to handle multiple interactions within the same bunch crossing and achieve an overall accuracy of the luminosity measurement better then 5 %.

2.3 Triggering and Data Acquisition

The proton and antiproton bunches cross in the Tevatron every 396 ns at CDF. At an instantaneous luminosity of 2×10^{32} cm^{-2}s^{-1} and an inelastic cross section of $\sim 60 \times 10^{-27}$ cm^2 at $\sqrt{s} = 1.96$ TeV, the Run II Tevatron is expected to produce about 12 million events every second. The CDF electronic readout systems are thus designed to be capable of operating at the higher bunch crossing rate, which is approximately 7.6 MHz. The specifications of the triggering system are described in this section in terms of their maximum functioning capacity.

The number of interactions per bunch crossing depends on the instantaneous luminosity. Figure 2.18 shows the number of interactions per bunch crossing as a function of the instantaneous luminosity.

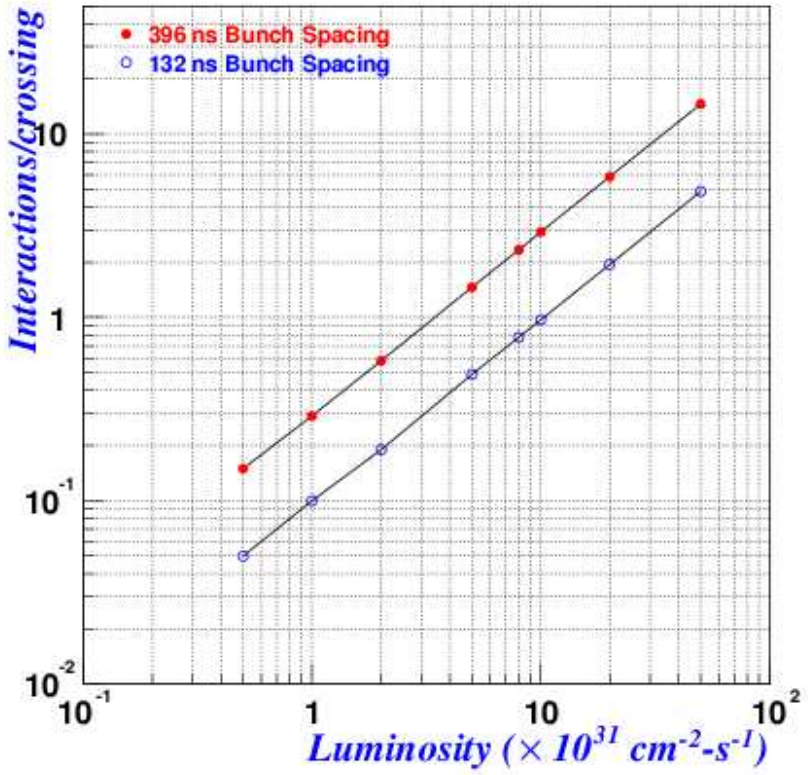

Figure 2.18: The number of interactions per bunch crossing as a function of luminosity for a bunch crossing of 132 ns and 396 ns (taken from [76]).

Recording all of these events would require an enormous data throughout of $\tilde{1}000$ GBytes/sec (Assuming the average size of an event is 100 KB). It is not only impossible to achieve this

rate with existing technology, but also unnecessary to do so. The majority of these events are less interesting minimum bias events in which the $p\bar{p}$ collisions are diffracting and produce no secondary particles with large transverse energy. The more interesting events are typically hard scattering and result in final state particles having large transverse momentum. However these types of processes also have very small cross sections.

To make a reasonable event selection and record data with a manageable size, we have to select and write to tape with the events we are interested only while skipping all other uninterested samples. This job is done by building a three-level-trigger system (Level-1, 2, 3), connected with buffered pipelines. Figure 2.19 shows a flow diagram of the trigger rates.

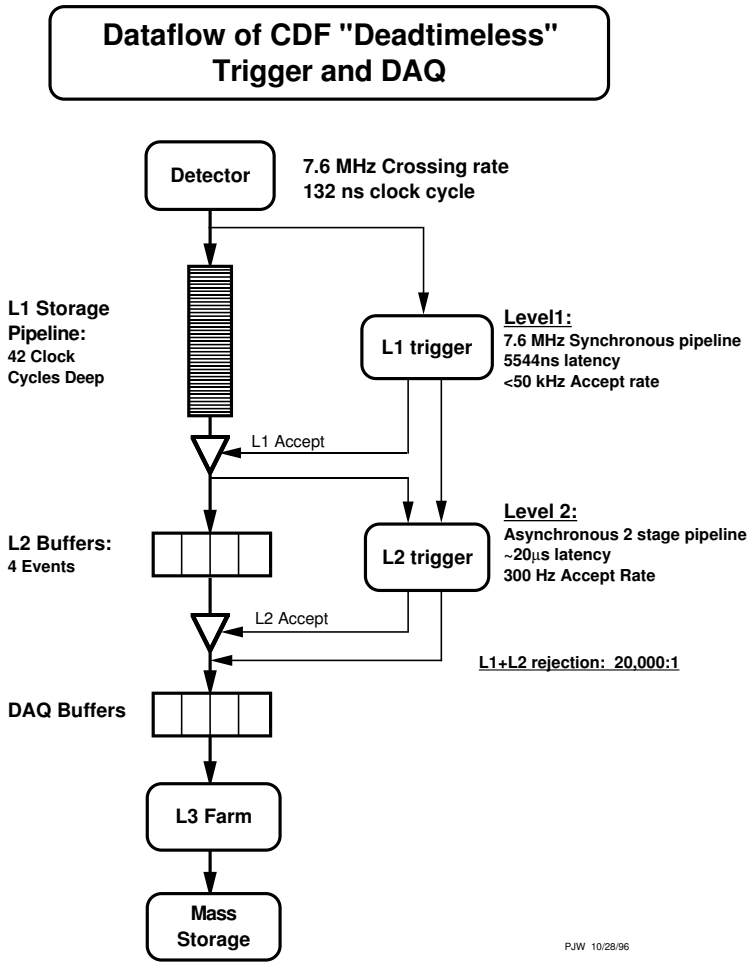

Figure 2.19: A flowchart of the CDF II online data flow. The specifications for the trigger system were designed for a maximum bunch crossing period of 132 ns.

The Level-1 trigger has only 4.5 μs to make a decision about each event. On average

it only accepts only one event out 150, bring the event rate down to about 10 KHz. The accepted events go further to Level-2. Level-2 has a little bit more time to process, about 20-30 μs per event. If Level-2 accepts the event, the whole detector is read out and the event goes further to the Event Builder and Level-3 trigger. The event rate at this stage is about 200-300 Hz. A block diagram showing the trigger components of the Level-1 and Level-2 triggers is shown in Figure 2.20. In the Event Builder the data fragments from the different parts of the detector are collected into a single event record, which is submitted to the Level-3. At Level-3 the acceptance is about one event out of 4. The accepted events are eventually transmitted to the mass storage devices at a rate of approximately 75 Hz and get written into the tape.

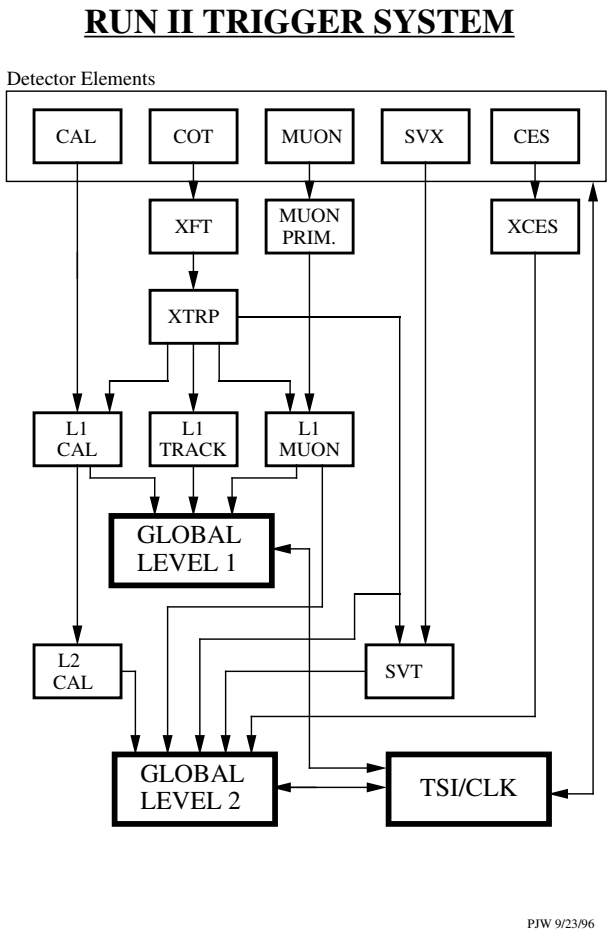

Figure 2.20: The Level-1 and Level-2 triggering systems. The TSI (Trigger Supervisor Interface) provides an interface between the trigger system, data acquisition and clock.

Level -1

The Level-1 trigger is synchronous with the 7.6 MHz Tevatron bunch crossing rate and has a decision time of 4 μs. At such rate it can't do the detailed reconstruction of COT tracks and muon stubs or obtain the details of showers in the calorimeters. Instead it uses some every roughly reconstructed patterns, which are called primitives. For instance, for the muon stubs we only know which muon chamber has the stub, but the stub position and slope are not known yet. The muon or calorimeter primitives, being combined with the track primitives would give us electrons, muons and jets, which we can trigger upon.

XFT and XTRP

The Extremely Fast Tracker (XFT) uses information from only 4 axial superlayers of the COT to identify high-p_T track primitive in the $r-\phi$ plane. To do so the hits from the COT are separated into two classes according to their drift time: *Prompt* hits with the drift time less than 44 ns and *Delay* hits with longer drift time. Then the hit pattern in the event is compared to a predefined set of patterns for both types of hits. This predefined set of patterns helps to find the segments of high-p_T tracks from the beamline very quickly. For all found segments, information about the charge, curvature and the ϕ position at COT superlayer is kept. Then the segments which seems coming from the same track are linked together into the track primitive. Given the short time which XFT has, the parameters of the track primitive are estimated very crudely. The information of the found track primitives is delivered to the Extra Polator unit (XTRP) and to Level-2. The XTRP matches the track primitives from XFT with the muon and calorimeter primitives. XTRP also uses a predefined set of pattern to speed up the matching process.

Level -2

The events accepted by Level-1 go to Level-2 for the further processing. The Level-2 uses the primitives from the Level-1 plus some additional information from the calorimetry and SVX. The information of $r-\phi$ hits from the SVX is used to extrapolate the XFT track primitives inside the SVX and to determine the track impact parameter, d_0. Some triggers look for tracks with high d_0, i.e. for the events with displaced vertex. This capability was introduced in Run II.

Event Builder and Level -3

In the Event Builder system the event fragments from the different parts of the detector are put together and go further as one whole piece. This is done with the aid of an Asyn-

chronous Transfer Mode (ATM) network switch, which takes the event fragments from the Level-2 VME crates, puts them in the proper places and then feeds them to the Level-2.

The Level-3 farm consists of hundreds of computers [87]. They are subdivided into 16 groups (sub-farms) of 16-18 computers in each. One computer in each sub-farm serves as converter node, accepting the data from the Event Builder and directing it to one of the other computers in the sub-farm (processor node) for the analysis. The accepted events go to the output nodes and then further to the mass storage device. Each output node is shared by two sub-farms.

The processor nodes transform the event fragments into a united event record, which has all the information about the event from all components of the detector. The Level-1 and Level-2 have to deal with crudely reconstructed primitives because of the lack of time. The Level-3 has enough time to fully reconstruct tracks, muons, electrons, jets etc and to apply the final trigger requirement to them.

Trigger path

The data used in this analysis was skimmed from the Stream B inclusive high-p_T central electron and muon dataset, and is discussed in further detail in Section 3.2. The L1, L2 and L3 triggers for these data samples are listed in Table 2.4.

	CEM path	
L1	L1_CEM8_PT8_v-4	
L2	L2_CEM8_PT8_CES3_TRK5_DPHI10	
	L2_CEM8_PT8_CES3_TRK8	
L3	L3_ELECTRON_CENTRAL_18	
	CMUP path	CMX path
L1	L1_CMUP6_PT4	L1_CMX6_PT8_PS1
		L1_CMX6_PT8_CSX_PS1
		L1_CMX6_PT8_CSX
L2	L2_AUTO_L1_CMUP6_PT4	L2_AUTO_L1_CMX6_PT8
	L2_TRK8_L1_CMUP6_PT4	L2_AUTO_L1_CMX6_PT8_CSX
L3	L3_MUON_CMUP18	L3_MUON_CMX18

Table 2.4: The trigger paths used in leptoquark search analysis. The number following the muon type denotes the p_T trigger of the muon stub. The number follwing the "PT" denotes the p_T of the XFT trigger.

The names of the trigger paths reflect their trigger criteria. The number following the muon type, e.g. the L1 trigger L1_CMUP**6**_PT4, denotes a Level-1 6 GeV/c trigger derived from the muon stub. The number following the "PT" denotes the muon momentum trigger from the XFT and "TRK" denotes a cut based on the track-p_T. "AUTO" denotes an

automatic Level-2 accept and the "PS" denotes the implementation of a prescaled acceptance rate. Similarly, the electron trigger L2_CEM8_PT8_CES3_TRK8 stands for a level-2 selection path as, the minimum energy stored in central electromagnetic calorimeter (CEM) as 8 GeV/c^2, minimum electron transverse momentum as 8 GeV/c, the minimum energy stored in central electromagnetic shower detector (CES) as 3 GeV/c^2, and the cut based on associated track-p_T as 8 GeV/c.

Part III

Analysis

Chapter 3

Data Analysis

3.1 Analysis Strategy and Routine

Chapter 2 introduced the experimental assets. The Tevatron and CDF provide us a platform to associate the physics objects with detector components.The data collected and recorded from the detector are usually called physics "events". We study the physics processes organizing these events by using their *signature*. The analysis performed in this thesis belongs to signature based searches.

The strategy in signature based searches usually follows such a routine: First we clarify the signature of the physics object for our analysis. Then by setting a series of kinematic cuts, we define the signal region and control region. Various regions are used to verify our understanding of the backgrounds' composition and distribution. They also help us to understand the signal behavior of kinematic quantities. Those cuts are applied to the data in sequence with the purpose of suppressing the backgrounds and enhancing the signal retention. Therefore the data analysis in this thesis is more or less like a counting experiment. All cuts need to be optimized so that we can get the maximum ratio of signal over backgrounds. In the end the final observed number of events is compared with the Standard Model expectation. If there is a significant inconsistency found between observations in the signal region and Standard Model predictions, it would be an indication of new Physics beyond the SM. Otherwise we will set an upper mass exclusion limit on the production cross section if no excess occurs.

As discussed in Section 1.3.2, third-generation leptoquarks can decay into $\tau q \tau q$ for $BR = 1$ and $\tau q \nu q$ for $BR = 1/2$. We examine the $\tau q \tau q$ mode where taus decay to leptons like electrons and muons. The quarks in any decay channel will fragment into jets. The neutrino will pass through the CDF II detector undetected due to its neutral charge and negligible mass and will appear as an imbalance of transverse energy in the detector. Thus, we search

for the signature as $lljj$ (Here l can be either electron or muon). Because the branching ratio for leptoquark decay is unknown, separate searches are performed for each possible final state. Each search contains the kinematic feature of two highly energetic jets plus two isolated high-p_T leptons (electron or muon).

The number of signal events for each channel is calculated based on the data luminosity, the theoretical cross section, and the efficiency of detecting the signal event in the data. Although the signature for each channel is different, the selection rule is same — we have to keep the selection efficiencies as high as possible. This is important for leptoquark searches so that a signal is experimentally accessible at the Run II energy of $\sqrt{s} = 1.96$ TeV. We will discuss the analysis details for each channel in the next two chapters.

3.2 The Inclusive High-p_T Data Sample

Each event recorded by CDF II contains extensive information about all kinds of physics objects, and at every second there are hundreds of thousands events generated at the interaction point. The way to handle such data is to split it into file systems with a manageable size, called *datasets*. Each dataset corresponds to a specific analysis purpose and matches the general event selection criteria.

Based on third generation leptoquark signaure, the datasets we needed in this analysis are lepton samples. For electrons, one such dataset is the Level-3 trigger dataset for high-p_T electrons located on tape with catalogue identifier *bhel08/09*. This dataset was reconstructed using offline CDF II software version 6.1.4 and is comprised of data collected from March 2002 to February 2006 [20]. For the muon case, the dataset is called *bhmu08/09*.

The data sample used for this analysis is a filtered version of the *bhel08/09* and *bhmu08/09* dataset stripped for the CDF Top Group from the inclusive high-p_T lepton datasets. The events were filtered using a loose set of cuts listed in Table 3.1 to keep a high efficiency for events containing high-p_T central electrons and muons. As listed in Table 2.4, The level3 trigger names for these high-p_T leptons are: ELECTRON_CENTRAL_18, MUON_CMUP18 and MUON_CMX18. The resulting inclusive central lepton datasets are located on tape with catalogue dataset identifier *bhel0d/bhmu0d* for data taken from March 2002 to August 2004, *bhel0h/bhmu0h* for data taken from December 2004 to September 2005, and *bhel0i/bhmu0i* for data taken from September 2006 to February 2006.

So far, the data sample we have processed for this analysis only includes dataset bhel0d and bhmu0d, which corresponds to an integrated luminosity of 361.82 ± 21.26 pb^{-1} and contains good runs from 141544 to 186598 . This luminosity figure contains a correction factor of 1.019 to account for a measured proton-antiproton inelastic cross section of 60.7 mb [65]. The good run list was selected following the Good Run List v14 created by the CDF

	tcl switch	Inclusive Electron Criterion
•	CdfEmObject.Pt set 9.0	$p_T > 9$ GeV/c
•	CdfEmObject.etCalMin set 18.0	$E_T > 18$ GeV
•	CdfEmObject.delX set 3.0	$\Delta x < 3.0$ cm
•	CdfEmObject.delZMin set 5.0	$\Delta z < 5.0$ cm
•	CdfEmObject.E/P set 4.0	$E/P < 4.0$
•	CdfEmObject.lshr set 0.3	$L_{shr} < 0.3$
•	CdfEmObject.hademMax set 0.125	$E_{HAD}/E_{EM} < 0.125$
	tcl switch	Inclusive Muon Criterion
•	minPtCut set 18.0	$p_T > 18$ GeV/c
•	useSlidingEmCut set true	$E_{EM} < max(2, 2 + 0.0115(p - 100))$ GeV
•	useSlidingHadCut set true	$E_{HAD} < max(6, 6 + 0.0280(p - 100))$ GeV
•	maxCMUdXCut set 5.0	Δx(CMU) < 5.0 cm
•	maxCMPdXCut set 10.0	Δx(CMP) < 10.0 cm
•	maxCMXdXCut set 20.0	Δx(CMX) < 20.0 cm
•	maxBMUdXCut set 50.0	Δx(BMU) < 50.0 cm

Table 3.1: The level-3 trigger criteria used to filter the *bhel0d/0h/0i* and *bhmu0d/0h/0i* dataset.

Data Quality Group [114]. Runs were selected based on the electron and muon detector. Good showermax and good silicon status were not required. For the CMX detector, the good run list is divided into two sections, pre-CMX and post-CMX. The luminosity with and without the CMX detector in the run is $\mathscr{L}$(pre-CMX) = 20.08 pb^{-1} and $\mathscr{L}$(post-CMX) = 341.74$\pm$20.50 pb^{-1} respectively. At the time of writing this thesis dataset bhel0h/i and bhmu0h/i are still under processing due to the limit of our disk space, we will update our search result once the analysis job is done.

3.3 Leptoquark Signal Monte Carlo

We generated ten 5000-event samples of leptoquark pairs decaying into τq with leptoquark masses M_{LQ} ranging from 80 to 260 GeV/c^2. The leptoquarks have charge $-2/3$ and are forced to decay as $LQ\overline{LQ} \to \tau^- \bar{b} \tau^+ b$. This decay mode corresponds to the BWR leptoquark model $\tilde{S}^L_{1/2}$, as shown in Table 1.3. Moreover, for each leptonic decay mode of tau, we use package TAUOLA [49, 50] to force the taus to decay to specific leptons at generator level, i.e. $\tau^- \to e^-$, $\tau^- \to \mu^-$. (Therefore it's thirty 5000-event samples instead of ten, because we apply TAUOLA to all three leptonic channels, and for each channel we generate ten 5000-event samples with various leptoquark masses.)

The events were generated using Pythia [112] and CDF software base release 6.1.4 . The samples were generated to simulate realistic beam conditions by emulating run number

151435 and using the following talk-to for the full beam position:

```
talk GenPrimVert
BeamlineFromDB set false
sigma_x set 0.0025
sigma_y set 0.0025
sigma_z set 28.0
pv_central_x set -0.064
pv_central_y set 0.310
pv_central_z set 2.5
pv_slope_dxdz set -0.00021
pv_slope_dydz set 0.00031
exit
```

All of the scalar leptoquark Monte Carlo samples have been generated at Leading Order with $Q^2 = M_{LQ}^2$ and the MRS-R2 PDF set [28]. The samples were simulated with cdfSim version 5.3.3_nt and were reconstructed using Production 6.1.4.

3.4 Background Monte Carlo

When we look at the final state of three possible leptonic decay channels, the main sources of background for the $eqeq$ and $\mu q\mu q$ channel are Drell-Yan events associated with 2 jets where the Z/γ^* decay into 2 electrons or 2 muons, top production where both $W \to e/\mu+\nu$, events due to QCD processes and fake leptons, and cosmic ray events accompanied by jets due to radiation. For the $eq\mu q$ channel however, the Drell-Yan is no longer the dominant force since Z/γ^* doesn't decay to lepton pairs in different generations. Top production becomes the major source in this channel. W events with 3+ jets also make a contribution to background, in which one of the jets is mismeasured as a lepton. Other backgrounds for these leptoquark decay channels include $b\bar{b}$, $Z \to \tau\tau$, and W^+W^- but have negligible contributions after kinematic selection.

Details of the generation of the background samples and specifics regarding the estimated background calculation in the $eqeq$,$\mu q\mu q$ and $eq\mu q$ channels are discussed in Sections 4.3 and 5.3 respectively.

3.5 Electrons

Because of its small mass, an electron leaves a large amount of ionizing energy in the CDF electromagnetic calorimeter. In particular, Central Electromagnetic Shower (CES) chamber system, Plug Electromagnetic Shower (PES) chamber system, and Central Preradiator

(CPR) chamber system are the most effective detectors to capture and record the electron events. Besides electrons, photons and jets also travel through and deposit a large amount of energy in the calorimeter. To identify electrons among these physics objects we use a number of selection cuts. A summary of the selection cuts and the individual efficiency for each cut are shown in Table 3.2 and 3.3, respectively. Details are discussed in the following section.

Variable	**'tight' central**	**'loose' central**
E_T	$>$ 20 (25) GeV	$>$ 20 (25) GeV
P_T	$>$ 10 GeV/c	$>$ 10 GeV/c
$Iso4$	$<$ 0.1	$<$ 0.1
E_{had}/E_{em}	$<$ 0.055 + 0.00045*E	$<$ 0.055 + 0.00045*E
E/P	$<$ 2.0 or $P_T >$ 50 GeV/c	
L_{shr}	$<$ 0.2	
$Q * \Delta x$	-3.0 cm to 1.5 cm	
$\lvert\Delta z\rvert$	$<$ 3.0 cm	
${\chi^2}_{strip}$	$<$ 10	
$\lvert z_0\rvert$	$<$ 60.0 cm	$<$ 60.0 cm
COT Track quality	3 axial and 3 stereo SL with at least 7 hits each	3 axial and 3 stereo SL with at least 7 hits each
FIDELE	1 (fiducial in CEM)	1 (fiducial in CEM)

Table 3.2: The electron ID selection cuts. See Ref. [90].

3.5.1 Electron Identification and Isolation Efficiency

A description of the variables used in the electron ID and isolation selections follows.

- E_T: The transverse electromagnetic energy deposited by the electron in the CEM is calculated as the electromagnetic cluster energy multiplied by $\sin(\theta)$, where θ is the polar angle provided by the best COT track pointing to the EM cluster. An electron cluster is made from a seed EM tower and at most one more shoulder tower in the same wedge, passing some well defined requirements [91]. The maximum cluster size could have two towers in pseudorapidity ($\Delta\eta \approx 0.2$) and one tower in azimuth ($\Delta\phi \approx$ 0.13 rad)

- P_T: The transverse momentum of the COT beam-constrained track as measured using the track curvature in the COT in the magnetic eld.

- Isolation: The energy in a cone of radius $\Delta R = \sqrt{\Delta\eta^2 + \Delta\phi^2} \leq 0.4$ around the electron cluster excluding the electron cluster divided by the energy in the electron

Variable	Data ($E_T > 20$ GeV)		Data ($E_T > 25$ GeV)	
	N-t eff. (%)	N-1 eff. (%)	N-t eff. (%)	N-1 eff. (%)
E_{had}/E_{em}	99.3 ± 0.2	99.4 ± 0.5	99.3 ± 0.2	99.4 ± 0.5
E/P	91.3 ± 0.3	93.4 ± 0.4	91.2 ± 0.3	93.3 ± 0.4
$Iso4$	97.5 ± 0.2	97.9 ± 0.4	97.6 ± 0.2	98.0 ± 0.4
L_{shr}	98.9 ± 0.2	99.4 ± 0.5	98.9 ± 0.2	99.4 ± 0.5
$Q * \Delta x$	98.2 ± 0.2	99.9 ± 0.5	98.2 ± 0.2	99.9 ± 0.5
$\lvert\Delta z\rvert$	99.3 ± 0.1	99.9 ± 0.5	99.4 ± 0.1	99.9 ± 0.5
${\chi^2}_{strip}$	96.3 ± 0.2	96.9 ± 0.4	96.2 ± 0.2	96.9 ± 0.4
# Axial SL	99.6 ± 0.1	99.7 ± 0.5	99.6 ± 0.1	99.7 ± 0.5
# Stereo SL	97.5 ± 0.2	97.8 ± 0.4	97.4 ± 0.2	97.8 ± 0.4
Total ϵ_T	82.5 ± 0.5		82.5 ± 0.5	
Total ϵ_L	94.0 ± 0.3		94.1 ± 0.3	

Table 3.3: The electron ID cut efficiency. ϵ_T stands for tight central selection efficiency, ϵ_L stands for loose selection. All uncertainties shown are statistical. See Ref. [90].

cluster. We correct the isolation variable for calorimeter leakage (see [97]).[1]

- E_{had}/E_{em}: The ratio of the hadronic (CHA+WHA) calorimeter energy to the electromagnetic (CEM) calorimeter energy for a cluster.
- E/P: The ratio of the EM cluster transverse energy to the COT track transverse momentum.
- L_{shr}: The lateral shower profile for electrons. This variable compares the energy in CEM towers adjacent to the seed tower for data and test beam electrons [98].
- Q * Δx: The distance in the r- ϕ plane between the extrapolated, beam constrained, COT track and the best matching CES cluster, times the charge of the track.
- Δ z: The distance in the r-z plane between the extrapolated, beam constrained, COT track and the best matching CES cluster.
- ${\chi^2}_{strip}$: The χ^2 comparison of the CES shower profile in the r-z view with the same profile extracted from test beam electrons.
- z_0: The z intersection of the track with the beam axis in the r-z plane.
- Track quality cuts: The electron-associated track must have passed through 3 axial and 3 stereo superlayers (SL), with at least 7 hits out of 12 in each SL.

[1] Most analyses in the EWK and Top groups are using the Isolation fraction rather than total Isolation, thus this is the variable we use here.

3.6 Muons

Compared to electrons, muons are about 200 times heavier and their bremsstrahlung radiation is therefore about 40,000 times smaller. They can travel through most detector calorimeter layers in CDF while leaving behind only a small amount of ionizing energy.

For this reason, the various muon detectors at the CDF II have been placed around the outer-most region of the detector. Three muon detection systems are included in this analysis: CMU, CMP, and CMX. Each is located in the central pseudorapidity region (see Section 2.2.3). We determine the muon type by reading its stub hits associated with its reconstructed track. For instance, we define a CMUP muon that contains stubs hits from both the CMU and CMP detectors, likewise a CMX muon contains a stub hit from the CMX muon system. In addition we define a special type of muon called "TRK" muon, which is neither the type of CMUP nor CMX (But it's still highly energetic, like the CMIO tracks used in Run I).

For $\mu q \mu q$ channel, we consider either CMUP, CMX or TRK muon as the candidate, for $eq\mu q$ channel we only conside CMUP or CMX muons. Selection details will be discussed in Chapter 4 and 5.

For all CMUP and (most) CMX muons in this analysis we are using non-beam-constrained tracking. The associated tracks objects are called "DefTrks". DefTrks are a collection of tracks stored in the PAD tracks collection. Since they are fitted by hit information from the silicon detectors, DefTrks do not rely on the run-dependent beam location. This method is inherited from the CDF Top Group.

The curvature of the muon tracks is corrected by so-called "Larry Correction", as prescribed in CDF Note 6558 [99]. The rate of false curvature was determined by studying the E/p distributions as a function of ϕ for positive and negative tracks in the data. The difference in the E/p for negatively and positively charged tracks is fitted and the curvature correction is determined to be:

$$\frac{1}{q \cdot p_T} = \frac{1}{q \cdot p_T} - 0.00039 - 0.00129 \cdot \sin(\phi + 0.47), \tag{3.1}$$

where p_T is the muon transverse momentum, ϕ is the azimuth angle and q is the charge. Only tracks with silicon are corrected. Therefore we apply the correction to muon tracks in which the error on the impact parameter is $\sigma(d0) < 0.33$. This requirement indicates the presence of silicon in the track reconstruction.

3.6.1 Muon Identification and Isolation Efficiency

A summary of the Muon ID selection is shown in Table 3.4. A description of the variables used in the muon ID and isolation selections follows.

The efficiency study of Muon ID is carried out by CDF electroweak group by taking $Z \rightarrow \mu^+\mu^-$ events as the learning process ([88, 89]). The CMUP and CMX muon identification method and the selection cuts variables are extracted from their report. However there is one point to notice, The Electroweak group uses beam-constrained COT tracks as their associated muon tracks, while in this thesis we are using non-beam-constrained track object as DefTrks. Details of the study of the muon ID and isolation efficiencies using DefTrks (including TRK muon), and the table of muon ID efficiencies can be found in Appendix D.

Cut Variable	**Purpose**	**Condition**
P_T	MIP	> 20 GeV/c
E_{em}/GeV		< 2+max(0,0.0115*(p-100))
E_{had}/GeV		< 6+max(0,0.0280*(p-100))
E_T^{iso}/P_T		< 0.1
Number of axial SL with ≥ 5 hits	track quality	≥ 3
Number of stereo SL with ≥ 5 hits		≥ 2
$\lvert z_0 \rvert$		< 60 cm
Tracks w/ no silicon hits: $\lvert d_0 \rvert$		< 0.2 cm
Tracks w/ silicon hits: $\lvert d_0 \rvert$		< 0.02 cm
$\lvert \Delta x \rvert$(CMU)	Track-Stub match	< 3 cm (if CMUP)
$\lvert \Delta x \rvert$(CMP)		< 5 cm (if CMUP)
$\lvert \Delta x \rvert$(CMX)		< 6 cm (if CMX)

Table 3.4: The muon ID selection cuts. TRK muons are not required to satisfy the track-stub match.

- E_{EM} and E_{HAD} – The muon is regarded as a Minimum Ionizing Particle (MIP) due to its ability in passing through the detector without leaving a large amount of energy in the calorimeter and with no significant reduction in its momentum. E_{EM} and E_{HAD} refer to the muon energy deposited in the electromagnetic and hadronic calorimeters. Because the amount of energy deposited in the calorimeter is dependent on the particle momentum, the E_{EM} and E_{HAD} selection cuts slide with the muon momentum. For $p_T < 100$ GeV/c, the cuts are $E_{EM} < 2$ GeV and $E_{HAD} < 6$ GeV. For $p_T > 100$ GeV/c, the cuts slide as $E_{EM} < 2 + 0.0115(cp_T - 100)$ GeV and $E_{HAD} < 6 + 0.0280(cp_T - 100)$ GeV. Figure 3.1 shows the E_{EM} and E_{HAD} distributions for leptoquark Monte Carlo data.

- E_T^{iso}/p_T – This is the fractional isolation defined by the ratio of transverse momentum

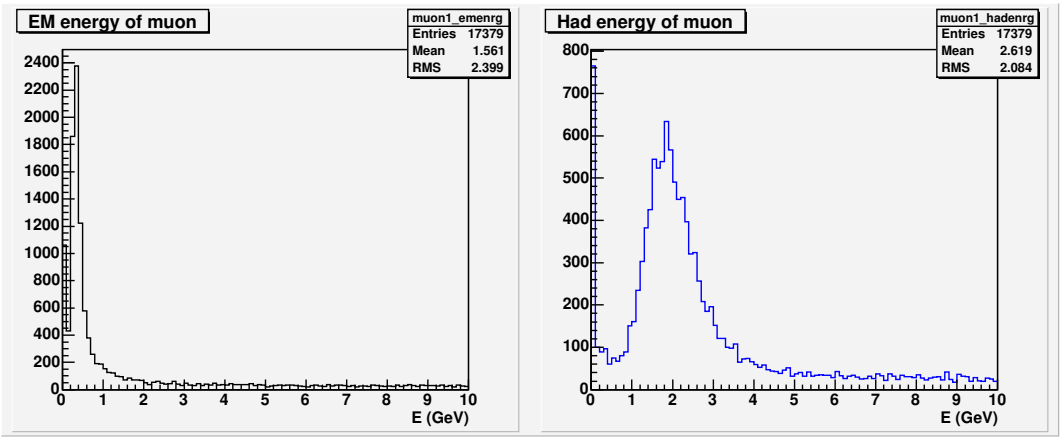

Figure 3.1: Electromagnetic (left) and hadronic energy (right) distributions for muons from leptoquark decay, $\mu q \mu q$ channel ($M_{LQ} = 120$ GeV/c^2).

in a cone radius 0.4 about the muon and the total transverse muon momentum. This cut reduces possible muons which radiate photons via higher-order QCD processes. A well isolated muon is required to have $E_T^{iso}/p_T < 0.1$. The efficiency of this cut is listed in Table 3.5.

- $|\Delta x|$ – It stands for the $r \cdot \phi$ distance between the fitted track path and the muon stub hit location. The purpose of this cut is to make sure that a track is correctly associated to a muon stub hit. E.g. If a track has a distance longer than 3 centimeters from a CMU muon stub (5 cm for CMP, 6 cm for CMX), most likely it is another charged particle's trajectory and we won't consider them as one associated muon event. The value of the stub-match cut is related to the distance in r of the muon detector from the event vertex. TRK muons are not required to pass this cut. Figure 3.2 shows the stub match distributions for the leptoquark Monte Carlo.

- Track quality variables – The number of COT Stereo hits and COT Axial hits, and z-vertex belong to this category. N_{stereo} and N_{axial} are required to be at least 20 and 16 respectively. By definition, a DefTrk contains at least 20 stereo and 16 axial COT hits **OR** at least 5 axial silicon hits. The purpose for applying this selection cut is thus to reject any muons which qualify as a DefTrk via the 5 axial silicon hit requirement. The effect of this cut is only felt by TRK muons. The reason for this is that because TRK muons are not required to have a stub match, their track pseudorapidity is not restricted to the central region of the CMUP and CMX detectors. The pseudorapidity range of the TRK muons is limited only by the quality of the track. For an event with a z-vertex less than 60cm, reconstructed TRK muons with a pseudorapidity greater

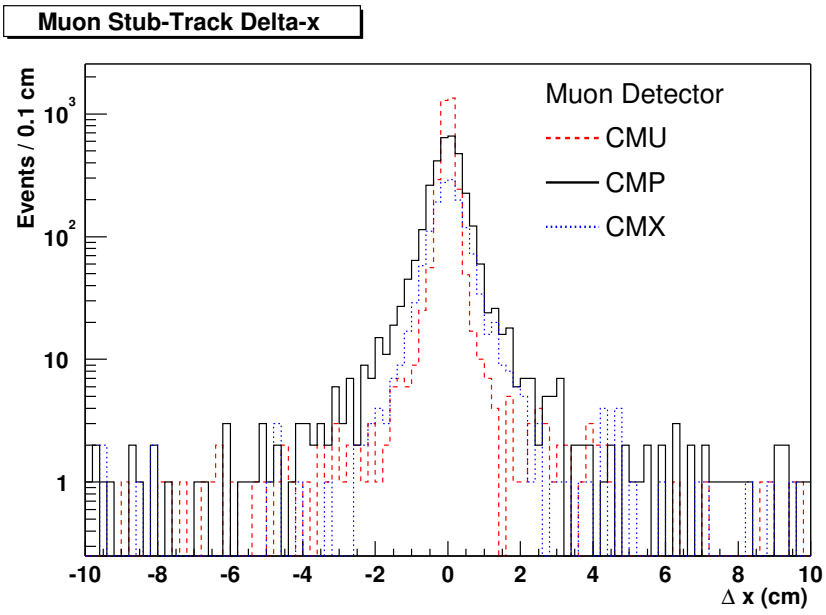

Figure 3.2: Stub-track matching for CMU, CMX, and CMX muon types in the $M_{LQ} = 220$ GeV/c^2 Monte Carlo sample.

than 2.0 are unlikely to pass muon selection cuts. As a result, COT hit requirements are likely to reject, for example, any forward region muon fitted to a track defined only by silicon hits and a BMU stub. The efficiency of this cut is 98.8% for TRK muons, and is 100% for CMUP and CMX muon.

A summary of the individual preselection efficiencies for each muon type is shown in Table 3.5. Detailed discussion about efficiency of trigger, reconstruction and Z-Vertex are included in Appendix E.

	CMUP	**CMX**	**TRK**
ϵ_{muID}	$88.9 \pm 0.6\%$	$95.2 \pm 0.5\%$	$94.0 \pm 0.1\%$
ϵ_{muIso}	$98.2 \pm 0.3\%$	$97.7 \pm 0.6\%$	$97.8 \pm 0.0\%$
ϵ_{trig}	$88.7 \pm 0.7\%$	$95.4 \pm 0.6\%$	-
ϵ_{muReco}	$94.5 \pm 0.6\%$	$99.2 \pm 0.3\%$	-
ϵ_{fid}	$95.1 \pm 0.1(stat) \pm 0.5(sys)\%$		

Table 3.5: Efficiency summary table as from Ref. [88], [89], [106], [111], and Appendix D and E.

3.7 Missing Transverse Energy, $\not\!\!E_T$

The transverse energy E_T, is defined as $E\sin\theta$, where E is the energy measured by the calorimeter. The imbalance in transverse energy, $\not\!\!E_T$, is the magnitude of $\not\!\!\mathbf{E_T}$ with $\not\!\!\mathbf{E_T} = -\sum_i E_T^i \mathbf{n_i}$, where $\mathbf{n_i}$ is a unit vector that points from the interaction vertex to the ith calorimeter tower in the transverse plane. Usually $\not\!\!E_T$ is regarded as the presence of an outgoing undetected neutrino in a physics event.

In this analysis, the raw $\not\!\!E_T$ value has to be corrected with two factors. First, the $\not\!\!E_T$ must be corrected to exclude the muon energy deposited into the calorimeter:

$$\not\!\!E_T(x) = -E(x) = -\sum_i (HAD_i + EM_i)\cos\phi_i + (HAD_T^\mu + EM_T^\mu)\cos\phi_\mu - p_T^\mu \cos\phi_\mu, \quad (3.2)$$

$$\not\!\!E_T(y) = -E(y) = -\sum_i (HAD_i + EM_i)\sin\phi_i + (HAD_T^\mu + EM_T^\mu)\sin\phi_\mu - p_T^\mu \sin\phi_\mu. \quad (3.3)$$

$E(x,y)$ is the sum of the hadronic (HAD) and electromagnetic (EM) energy deposited in the i wedges of the calorimeter. Each physics event is assumed to have zero initial transverse energy and thus the x and y components of the $\not\!\!E_T$ are negatively equated to the x and y components of the total transverse energy detected in the event. The muon energy in an event is added to the total transverse energy by subtracting the energy it deposits in the calorimeter and adding the reconstructed momentum.

Secondly, the total sum of transverse energy should be further corrected by the presence of jets in the event as discussed in Section 3.8. The jet energy corrections are accounted for in the $\not\!\!E_T$ calculation.

3.8 Jets

At CDF jets are observed as clustered energy depositions in the calorimeters, usually resulting from the quark or gluon fragmentation. Jets are clustered using a cone algorithm with a fixed cone size in which the center of the jet is defined as (η^{jet}, ϕ^{jet}) and the size of cone as $R = \sqrt{(\eta^{tower} - \eta^{jet})^2 + (\phi^{tower} - \phi^{jet})^2} = 0.4$, 0.7 or 1.0. In this analysis we use the jets with clustering cone-radius as 0.7. Furthermore, we ask jets stay in the region of pseudorapidity within $|\eta| \leq 2.0$.

We take two types of jets into our selection. The first one is "tight", whose transverse energy must be greater then 25 GeV. The other is "loose", which is required to have $E_T > 15$ GeV. Tight jets are a subset of loose jets. The jet energies can be distorted due to various underlying and physical effects. The raw jet energies are thus scaled to account for these effects in order to obtain the energy of the final state particle-level jet. The following combination of corrections to the raw jet energies account for these effects (the nomenclature

follows CDF convention)[115, 41]:

- Eta-dependent - This correction is applied to raw jet energies measured in the calorimeter to make jet energy uniform along eta. The transverse energy of the two jets in a 2->2 process should be equal. This property is used to scale jets outside the $0.2<|\text{eta}|<0.6$ region to jets inside the region. (Level 1)
- Multiple interactions - Corrects the jets for events with multiple interactions for the same bunch crossing. The contributions from the extra interactions are subtracted on average. (Level 4)
- Absolute - Corrects the jet energy measured in the calorimeter for any non-linearity and energy loss in the un-instrumented regions of each calorimeter. (Level 5)
- Underlying event - Corrects for the energy associated with the spectator partons in a hard-scattering event. The energy is subtracted on average. (Level 6)
- Out-of-cone - Corrects the jet energy for leakage of radiation outside the clustering cone used for jet definition. (Level 7)

Level 2 and Level 3 corrections were used to correct the jet energies, and account for the energy scale difference between Run I and Run II. Since the new Gen 6 cdf software was released, these two levels of corrections were replaced by other corrections and are no longer in use.

Chapter 4

Search for Scalar Leptoquarks in the $eqeq$ and $\mu q \mu q$Channel

As discussed in Section 1.3.2, the experimental signature for pair-produced third generation scalar leptoquarks for the $BR = 1$ case consists of two isolated high-p_T taus and two energetic jets. In this chapter we focus on decay of both taus into two electrons first, then we discuss the case where both taus decay into two muons.

4.1 $eqeq$ channel analysis

The full data sample is reduced by preselecting events according to the criteria described in Appendix E. Each event is required to be a di-electron event such that at least one electron is of type 'tight' central and the second electron is of type so-called 'medium' central.

The definition of tight central electron and the corresponding identification cuts are shown in section 3.5 and table 3.2. The medium central electron is defined in the following table 4.1.

For the di-electron event selection, we pick the combination of one tight central electron plus one medium central electron instead of two tight electrons. The main reason for a such combination is to improve our lepton selection efficicency from signal.

4.1.1 Monte Carlo study and analysis cuts applied

Once the di-electron events have been preselected, the events are required to pass a set of selection cuts designed to discriminate the preselected events from possible backgrounds mimicking the leptoquark signal. Section 4.3 discusses the various possible backgrounds in the $eqeq$ channel. The simulated signal and background events used to study the acceptance

Variable		Medium Central Cut
kinematic cuts		
	E_T	> 8 GeV
	P_T	> 4 GeV/c
	Fiduciality	fidEle = 1
		(CES based)
	Z_{vertex}	$\lvert {z_0}^{track} \rvert < 60.0$ cm
identification cuts		
	E_{had}/E_{em}	$< 0.055 + 0.00045$*E
	E/P	< 1.8 or $P_T > 50$ GeV/c
	L_{shr}	< 0.2
	${\chi^2}_{strip}$	< 10.0
	$Q * \Delta x$	-3.0 cm to 1.5 cm
	$\lvert \Delta z \rvert$	< 3.0 cm
	$Iso4$	< 0.1

Table 4.1: Medium central eletron summary table as from Ref. [92].

of the selection cuts are discussed in Section 3.3 and 3.4. The selection cuts are applied to the data in the following order:

1. The first electron with $E_T > 25$ GeV, the following electron with $E_T > 10$ GeV - This cut ensures that the electron is a properly triggered electron and reduces the amount of QCD background associated with less energetic electrons. The leading and second leading electron E_T distributions for a leptoquark mass of 120 GeV/c^2 are shown in Figure 4.1.

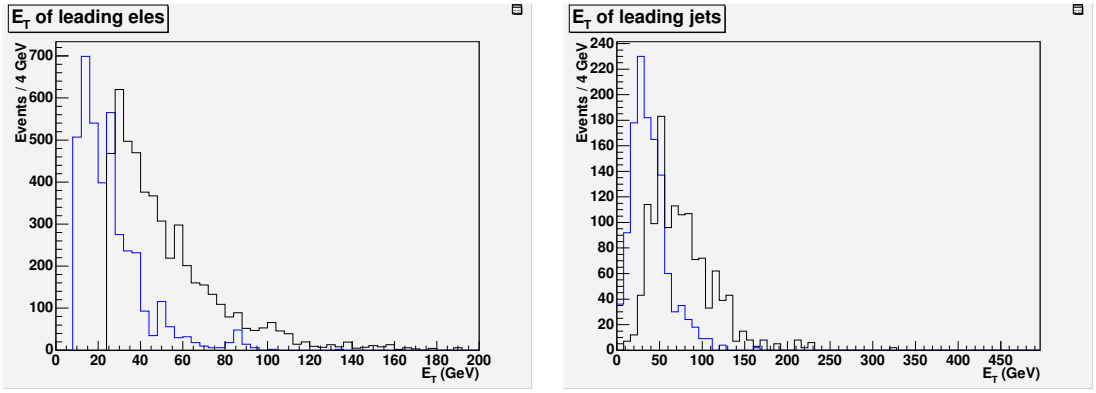

Figure 4.1: P_T and E_T distributions for leading (black) and second leading (light blue) electrons (left) and jets (right) for $M_{LQ} = 120$ GeV/c^2.

2. Two jets with $E_T(j_1) > 25$ and $E_T(j_2) > 15$ GeV - The requirement that both a tight and loose jet be present in the event significantly reduces the number of background events. We also require these two jets to stay in the central region of CDF detector ($|\eta_{detector}| < 2.0$), out of cone within two electrons mentioned above ($\Delta R(electron, jet) > 0.7$), plus having a EM fraction less than 0.9. The leading and second leading jet E_T distributions for a leptoquark mass of 120 GeV/c^2 are shown in Figure 4.1.

3. $E_T(j_1) + E_T(j_2) > 50$ GeV

4. Topology cut: $\Delta\phi(leptons + jets, \not\!\!E_T) > 120°$ - The angle cut is mainly to filter the Drell-Yan background out. Due to the lack of neutrinos, Drell-Yan won't have a balanced MeT with leptons plus jets. The balanced situation is more or less like a back-to-back case (180°). Here, after cut optimization, we set the lower limit of the angle between electrons plus jets and missing transverse energy to be 120 degrees.

5. Transverse kinematic variables cut - The purpose for this cut is to suppress the top production backgrounds. Top decays into W and b quark, while W decays into leptons. e.g. $W \to e\nu$. On the other hand, the third generation leptoquark decays to τ and b, while τ decays into neutrinos and an electron. Hence the different mass spectrum of W and τ becomes the key to filter top backgrounds out of the signal, and that is the motivation to put a transverse kinematic variable check here. More details about this check are discussed in section 4.3.2. After cut optimization, we set $M_T(e1, \not\!\!E_T) \leq 25GeV$ and $M_T(e2, \not\!\!E_T) \leq 25GeV$ as the cut condition for *eqeq* channel.

6. H_t cut - Here we define two variables, Et_sum and Ht_mag:
   Et_sum $= E_{T\,e1} + E_{T\,e2} + E_{T\,j1} + E_{T\,j2}$
   Ht_mag $= \sqrt{(E_{e1} + E_{e2} + E_{j1} + E_{j2})_x^{\,2} + (E_{e1} + E_{e2} + E_{j1} + E_{j2})_y^{\,2}}$
   Then we make a 2-D plot of Et_sum (as y) v.s. Ht_mag (as x). Because magnitude of vectors are always smaller than or equal to the sum of transverse values, a distribution plot of Et_sum v.s. Ht_mag within the region of the left top plane is expected. We found that this cut is an extremely effective filter for Drell-Yan and signal (See Figure 4.2.) From the plot we can see that Drell-Yan distribution dots stay closer to the y-axis, in other words, they are in a steeper slope region, while the LQ signal scatters more. Based on this difference, after optimization we set the cut condition as:

   Et_sum $\leq$ 3.0 * Ht_mag + 40.0

7. Removal of events with 75 $< M_{ee}$/GeV/c$^2 <$ 105 and $M_{ee} <$ 15 GeV/c^2 - This cut reduces the Drell-Yan backgrounds and low energy electron events from J/Ψ or Υ. We

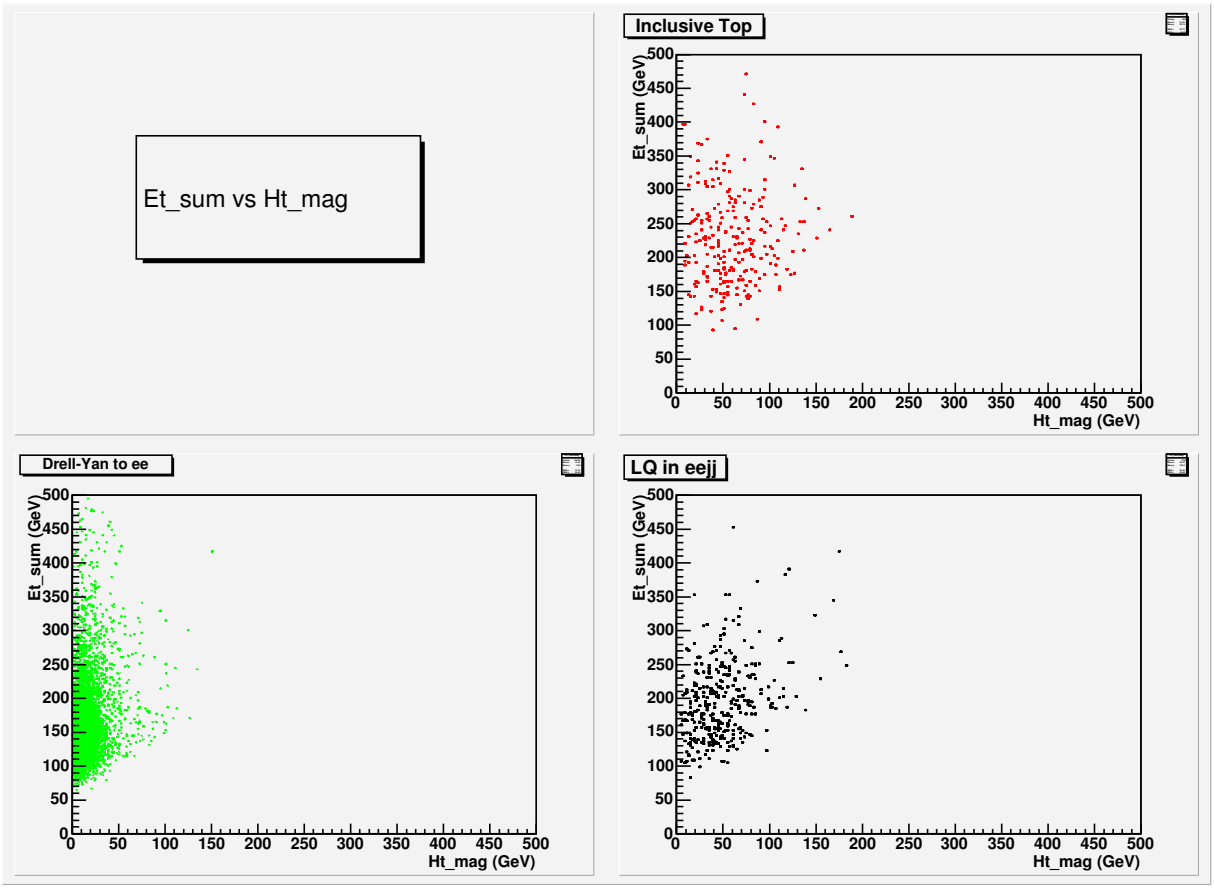

Figure 4.2: Et_sum v.s. Ht_mag, comparison among Inclusive Top (right top), Drell-Yan to di-electron + 2jets(left bottom), and Leptoquark mass @ 120 GeV in eqeq (right bottom). The size of the bins is 1 GeV by 1 GeV

also ask two electrons to have opposite electric charges to avoid a mass peak scan on wrong e-e pairs.

4.1.2 Acceptance and Kinematical Efficiency Calculation

After we set up and optimize the analysis cuts, the kinematic acceptance based on Monte Carlo study is calculated in this way:

$$A(LQ) = \frac{\text{N(events passing selection cuts)}}{\text{N(total events)}} \tag{4.1}$$

Since the electron ID and isolation efficiencies are calculated using real physics data, the efficiencies from these selection cuts will not be the same for simulated events. Therefore a correction factor accounting for this disparity must be applied to the signal and background Monte Carlo. Table 4.2 shows the scale factors for the leptoquark Monte Carlo for several leptoquark masses. Scale factors were also calculated for the various backgrounds.

Mass (GeV/c^2)	Tight	Loose	Medium
Ele ID: Data/MC			
80	0.9843	1.0589	1.0472
120	0.9914	1.0767	1.0590
160	1.0145	1.0695	1.0615
200	1.0021	1.0554	1.0623
240	0.9826	1.0328	1.0667
Ele Isolation: Data/MC			
80	1.0447	1.0103	1.0311
120	1.0490	1.0180	1.0349
160	1.0561	1.0384	1.0617
200	1.0523	1.0410	1.0758
240	1.0637	1.0619	1.1052

Table 4.2: The ratios of efficiences between data and leptoquark Monte Carlo. The ratio is defined as data/MC. Scale factors calculated for the background Monte Carlo are not shown here.

Furthermore, the total analysis cut efficiency is folded with Monte Carlo acceptance, and the efficiency of trigger, electron ID, electron reconstruction, Z-vertex cut and fractional isolation cut (Preselection efficiencies are discussed and listed in Appendix E, also see Table 3.5 for details).

$$\epsilon_{TOTAL} = A(LQ) \times SF(MC) \times \epsilon_{trigger} \times \epsilon_{ele\ ID} \times \epsilon_{recon} \times \epsilon_{vertex} \times \epsilon_{iso} \tag{4.2}$$

The result of analysis cut efficiencies is reported in Table 4.3. Figure 4.3 shows the kinematic acceptance as a function of the leptoquark mass.

Mass GeV/c^2	Acceptance	NLO σ (pb)	Expected events number at 361 pb^{-1}
80	1.30±0.1±0.3%	52.4	7.83
100	2.47±0.1±0.3%	15.8	4.48
120	3.02±0.1±0.4%	5.73	2.02
140	3.82±0.1±0.4%	2.38	1.04
160	4.18±0.1±0.4%	1.08	0.52
180	5.49±0.2±0.5%	0.525	0.33
200	6.08±0.2±0.5%	0.268	0.19
220	5.65±0.2±0.5%	0.141	0.09
240	5.23±0.2±0.5%	0.0762	0.05
260	5.12±0.2±0.5%	0.0419	0.025

Table 4.3: Kinematic efficiency as a function of the leptoquark mass. To normalize the expected event number with the same luminosity as real data, the cross-section has to be multiplied by the branching ratio $\tau\tau \to ee$, since we force such tau decay to electrons at the generator stage.

After our analysis cuts, four events remain in the real data. In Table 4.4 we report the number of events surviving each kinematical cut.

Kinematic Cut	$\mathbf{N_{obs}}$
2 electrons with $E_T(e1) > 25$ and $E_T(e2) > 10$ GeV	2646
2 jets with $E_T(j1) > 25$ and $E_T(j2) > 15$ GeV	96
$E_T(j1) + E_T(j2) > 50$ GeV	96
Topology cut	47
$M_T(e1, \not\!\!E_T)$ and $M_T(e2, \not\!\!E_T) \leq 25\ GeV/c^2$	26
Ht cut	4
Removal of events with $75 < M_{ee} < 105$ and $M_{ee} > 15$ GeV/c^2	4

Table 4.4: List of events passing the selection cuts in 361 pb^{-1} of data.

4.2 $\mu q \mu q$ channel analysis

The signature for the $\mu q \mu q$ channel is two high-p_T muons plus two energetic b-flavor jets. As for muon combinations, each event is required to be an opposite-sign *dimuon* event such that one muon is of type CMUP or CMX and the second muon is of type CMUP, CMX, or TRK.

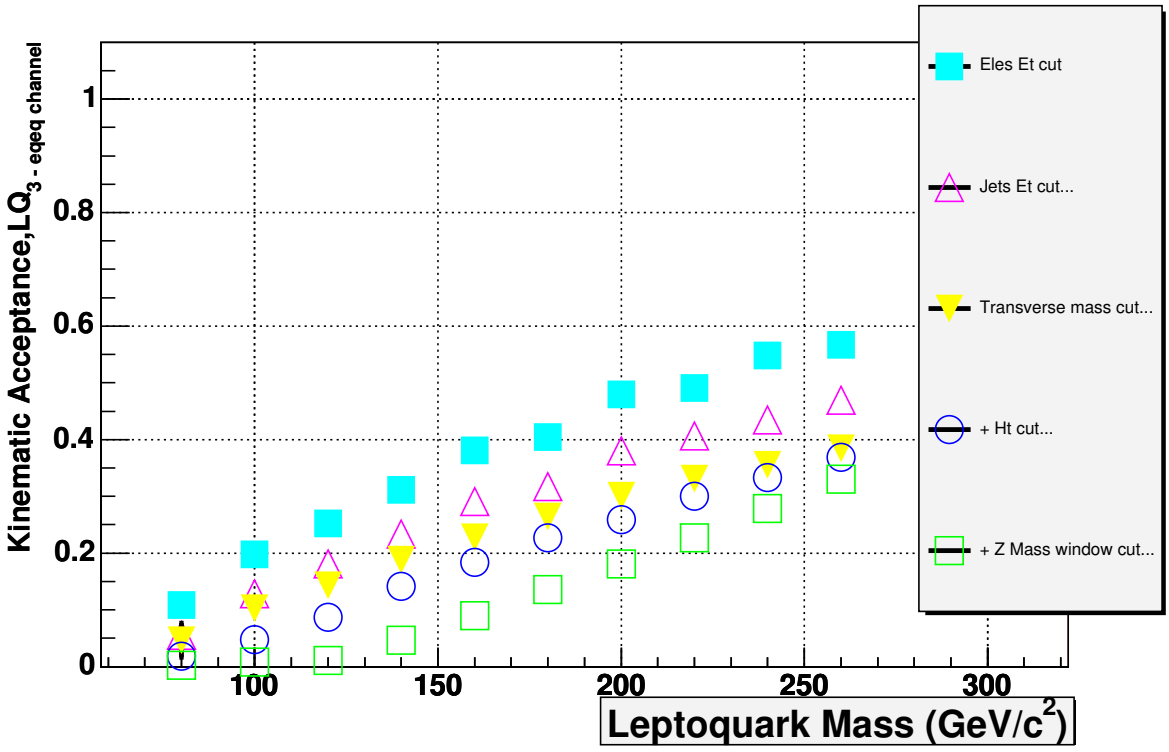

Figure 4.3: The selection cut efficiencies as a function of leptoquark mass in eqeq channel. The curve shows the final efficiency with scale factor of Data/MC included. The statistical errors are plotted.

The full data sample is reduced by preselecting events according to the criteria described in Appendix E. The di-muon pair could have five possible combinations:

- CMUP-CMUP where both the muons pass the selection criteria for a CMUP muon.
- CMUP-CMX where one muon passes the CMUP identification criteria and the other passes CMX.
- CMX-CMX where both the muons pass the selection criteria for a CMX muon. A CMX muon is demoted to the status of TRK if it fails to pass the COT exit radius requirement.
- CMUP-TRK where one muon passes the CMUP identification criteria and the other is neither a CMUP nor CMX muon.
- CMX-TRK where one muon passes the CMX identification criteria and the other is neither a CMUP nor CMX muon.

Five combinations, five corresponding event-type efficiencies. This is because the preselection efficiencies depend on the muon type, each dimuon event must be categorized separately so that its efficiency can be calculated correctly based on the proper candidate muon type.

The efficiencies of five different preselection combinations are shown as follows:

$$
\begin{aligned}
\epsilon_{PP} &= (\epsilon_P^{trig} \times (2 - \epsilon_P^{trig})) \times \epsilon^{fid} \times (\epsilon_P^{reco} \times \epsilon_P^{ID} \times \epsilon_P^{iso})^2 \\
\epsilon_{PX} &= (\epsilon_P^{trig} + \epsilon_X^{trig} - (\epsilon_P^{trig} \times \epsilon_X^{trig})) \times \epsilon^{fid} \times \epsilon_P^{reco} \times \epsilon_X^{reco} \times \epsilon_P^{ID} \times \epsilon_X^{ID} \times \epsilon_X^{iso} \times \epsilon_P^{iso} \\
\epsilon_{XX} &= (\epsilon_X^{trig} \times (2 - \epsilon_X^{trig})) \times \epsilon^{fid} \times (\epsilon_X^{reco} \times \epsilon_X^{ID} \times \epsilon_X^{iso})^2 \\
\epsilon_{PT} &= \epsilon_P^{trig} \times \epsilon_P^{ID} \times \epsilon_T^{ID} \times \epsilon_P^{reco} \times \epsilon^{fid} \times \epsilon_P^{iso} \times \epsilon_T^{iso} \\
\epsilon_{XT} &= \epsilon_X^{trig} \times \epsilon_X^{ID} \times \epsilon_T^{ID} \times \epsilon_X^{reco} \times \epsilon^{fid} \times \epsilon_X^{iso} \times \epsilon_T^{iso}
\end{aligned}
$$

There is no trigger efficiency associated with TRK muons since they are not triggerable muons. Using the values from Table 3.5, we obtain for the event-type efficiencies listed in Table 4.5.

4.2.1 Acceptance and Kinematical Efficiency Calculation

Once the dimuon events have been preselected, the events are required to pass a set of selection cuts designed to discriminate the preselected events from possible backgrounds mimicking the leptoquark signal. Section 4.3 discusses the various possible backgrounds in

Event-type Efficiencies, $\mu q \mu q$ channel	
$\epsilon_{PP} =$	0.637 ± 0.011
$\epsilon_{PX} =$	0.718 ± 0.011
$\epsilon_{XX} =$	0.807 ± 0.011
$\epsilon_{PT} =$	0.631 ± 0.008
$\epsilon_{XT} =$	0.761 ± 0.007

Table 4.5: The total event-type efficiencies calculated using values from Table 3.5.

the $\mu q \mu q$ channel. As discussed in previous Sections 3.3 and 3.4, we generate Monte Carlo events to simulate the signal and background and study the acceptance of the selection cuts. These selection cuts are applied to the data in the following order:

1. The first muon with $p_T > 25$ GeV/c, followed by another muon with $p_T > 10$ GeV/c - This cut ensures that the muon is a properly triggered muon and reduces the amount of QCD background associated with less energetic muons. The leading and second leading muon p_T distributions for a leptoquark mass of 220 GeV/c^2 are shown in Figure 4.4.

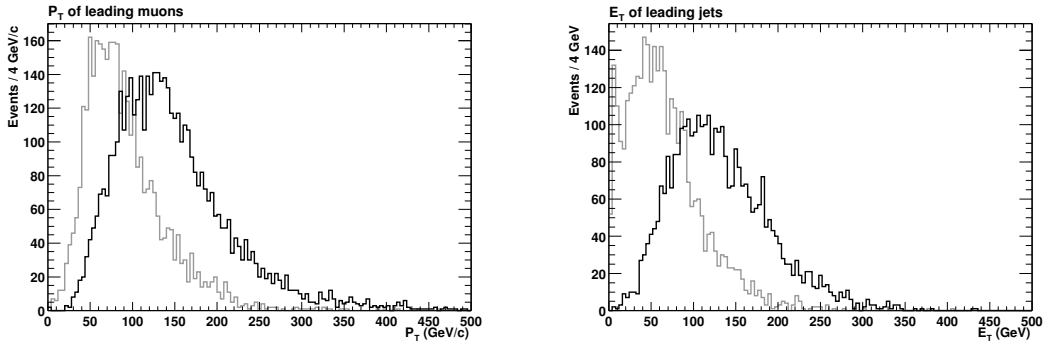

Figure 4.4: P_T and E_T distributions for leading (dark) and second leading (light) muons (left) and jets (right) for $M_{LQ} = 220$ GeV/c^2.

2. 2 jets with $E_T(j_1) > 25$ and $E_T(j_2) > 15$ GeV - The requirement that both a tight and loose jet be present in the event significantly reduces the number of background events. We also require these two jets to stay in the central region of CDF detector ($|\eta_{detector}| < 2.0$), out of cone within two muons mentioned above ($\Delta R(muon, jet) > 0.7$), plus having a EM fraction less than 0.9. The leading and second leading jet E_T distributions for a leptoquark mass of 220 GeV/c^2 are shown in Figure 4.4.

3. $E_T(j_1) + E_T(j_2) > 50$ GeV

4. Topology cut: $\Delta\phi(leptons+jets, \not\!\!E_T) > 120°$ - The angle cut is mainly to filter out the Drell-Yan background. Due to the lack of neutrinos, Drell-Yan won't have a balanced $\not\!\!E_T$ with leptons plus jets. The balanced situation is more or less like a back-to-back case (180°). Here, after cut optimization, we set the lower limit of the angle between muons plus jets and missing transverse energy to be 120 degrees.

5. Transverse kinematic variables cut - The purpose of this cut is to suppress the top production backgrounds. Top decays into W and b quark, while W decays to leptons, e.g. $W \to \mu\nu$. On the other hand, the third generation leptoquark decays to τ and b, while τ decays to neutrinos and a muon. Hence the different mass spectra of the W and the τ becomes the key to filter top background out of signal, and that provides the motivation to put a transverse kinematic variable check here. More details about this check are discussed in section 4.3.2. After cut optimization, we set $M_T(\mu 1, \not\!\!E_T) \leq 25 GeV$ and $M_T(\mu 1, \mu 2, \not\!\!E_T) \leq 80 GeV$ as the cut condition for the $\mu q \mu q$ channel.

6. H_t cut - The method is similar to the one used in channel eqeq.
   Et_sum $= E_{T\,\mu 1} + E_{T\,\mu 2} + E_{T\,j1} + E_{T\,j2}$
   Ht_mag $= \sqrt{(E_{\mu 1} + E_{\mu 2} + E_{j1} + E_{j2})_x^{\,2} + (E_{\mu 1} + E_{\mu 2} + E_{j1} + E_{j2})_y^{\,2}}$
   Except in $\mu q \mu q$, we set the cut condition as
   Et_sum $\leq$ 4.0 * Ht_mag + 50.0 for the best S/B.

7. Removal of events with $76 < M_{\mu\mu}/\mathrm{GeV/c^2} < 110$ and $M_{\mu\mu} < 15$ GeV/c^2 - This cut reduces the Drell-Yan background and low energy muon events from J/Ψ or Υ. Due to the large mass of the muon, the muon curvature for high-p_T muons is not a very reliable quantity. Therefore there is no requirement that the muons in this veto are of opposite charge.

Figure 4.5 shows the selection cut acceptances relative to the number of matched muons of type CMUP, CMX and TRK. The final selection cut acceptances are calculated relative to the total number of signal events in the Monte Carlo sample.

$$A(LQ) = \frac{\mathrm{N(CMUP,\ CMX\ or\ TRK\ muons\ passing\ selection\ cuts)}}{\mathrm{N(total\ events)}} \tag{4.3}$$

Similar to *eqeq* channel, the total efficiency must be folded with a scale factor, which stands for the disparity of selection efficiencies between Monte Carlo and the real data. Table 4.6 shows the scale factors for the leptoquark Monte Carlo for several leptoquark masses. Scale factors were also calculated for the various backgrounds.

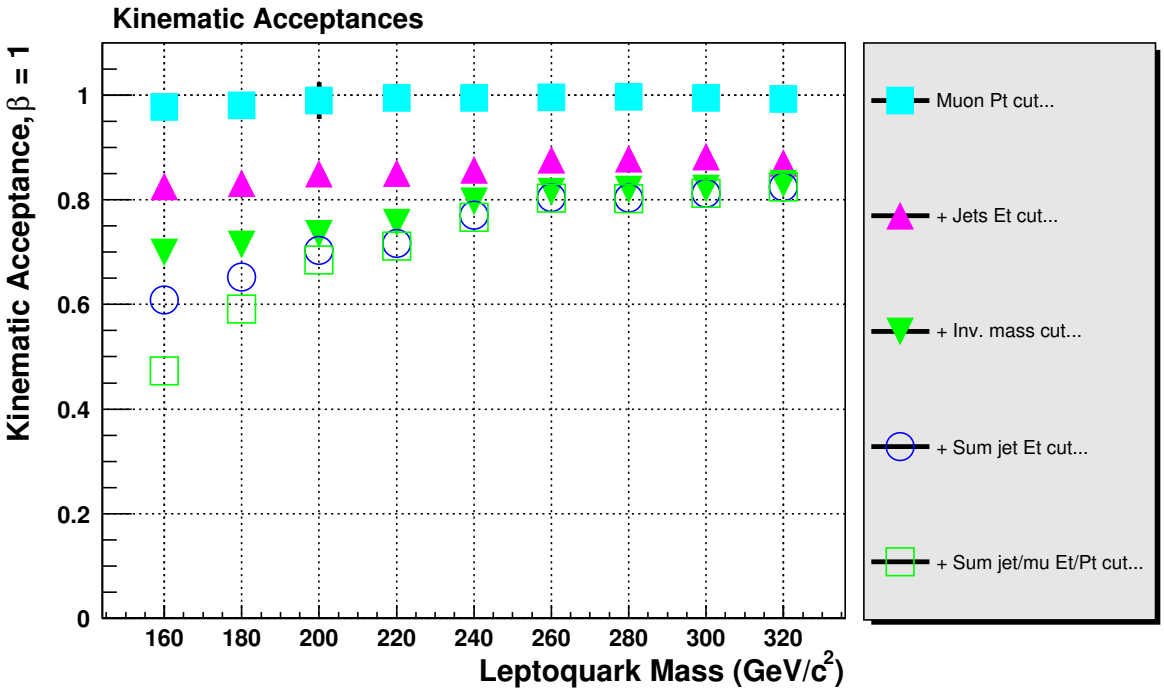

Figure 4.5: The selection cut efficiencies as a function of leptoquark mass. The top curves show the relative efficiencies of the cuts in sequence, independent of both the preselection and the geometric detector acceptance. The bottom curve shows the final efficiency with the geometric acceptance included. The statistical errors are plotted.

Mass (GeV/c^2)	CMUP	CMX	TRK
Muon ID: Data/MC			
80	0.9745	1.0162	1.0211
120	0.9810	1.0213	1.0385
160	0.9844	1.0478	1.0499
200	0.9859	1.0836	1.0570
240	0.9850	1.0691	1.0832
Muon Isolation: Data/MC			
80	1.0409	1.0053	1.0177
120	1.0478	1.0095	1.0545
160	1.0492	1.0127	1.0862
200	1.0501	1.0194	1.1288
240	1.0535	1.0306	1.1610

Table 4.6: The ratios of efficiences between data and leptoquark Monte Carlo. The ratio is defined as data/MC. Scale factors calculated for the background Monte Carlo are not shown here.

A previous leptoquark search in the $\mu q \mu q$ channel didn't take TRK muon into consideration (e.g.[103]) till 2004, when we analyzed 2nd generation leptoquarks with 197 pb^{-1} of Run II data ([100]). Since the geometric acceptance is related to the pseudorapidity coverage of the muon systems, selecting TRK muons will increase the total selection acceptance significantly (about 200% boost compare to CMUP selection only) due to the larger pseudorapidity coverage. The shortcoming however, is that loose η also allows more background or fake events to become candidates.

Mass (GeV/c^2)	CMUP/CMUP	CMUP/CMX	CMX/CMX	CMUP/TRK	CMX/TRK
80	1.9±0.1±0.2%	1.4±0.1±0.1%	0.2±0.0±0.0%	2.7±0.1±0.2%	0.9±0.1±0.1%
100	2.2±0.1±0.2%	1.6±0.1±0.1%	0.3±0.0±0.0%	3.2±0.1±0.3%	1.1±0.1±0.1%
120	2.8±0.1±0.3%	2.1±0.2±0.2%	0.5±0.0±0.0%	4.0±0.1±0.3%	1.6±0.1±0.2%
140	2.6±0.1±0.3%	2.2±0.2±0.2%	0.4±0.0±0.1%	4.4±0.2±0.3%	1.7±0.1±0.2%
160	3.1±0.2±0.3%	2.1±0.2±0.2%	0.5±0.0±0.1%	5.1±0.2±0.4%	1.8±0.1±0.2%
180	3.3±0.2±0.3%	2.5±0.2±0.2%	0.5±0.1±0.1%	5.9±0.2±0.4%	1.7±0.1±0.2%
200	3.7±0.2±0.4%	2.3±0.2±0.2%	0.4±0.0±0.1%	5.7±0.2±0.4%	1.8±0.1±0.2%
220	3.8±0.2±0.4%	2.5±0.3±0.2%	0.4±0.0±0.0%	5.8±0.2±0.4%	2.2±0.1±0.3%
240	3.1±0.2±0.3%	2.3±0.2±0.2%	0.5±0.0±0.1%	6.0±0.3±0.5%	2.1±0.1±0.3%

Table 4.7: Kinematic efficiency as a function of the leptoquark mass.

The selection acceptance for each leptoquark mass is multiplied by the event-type efficiencies. The results for each di-muon combination are listed in Table 4.7 and are shown

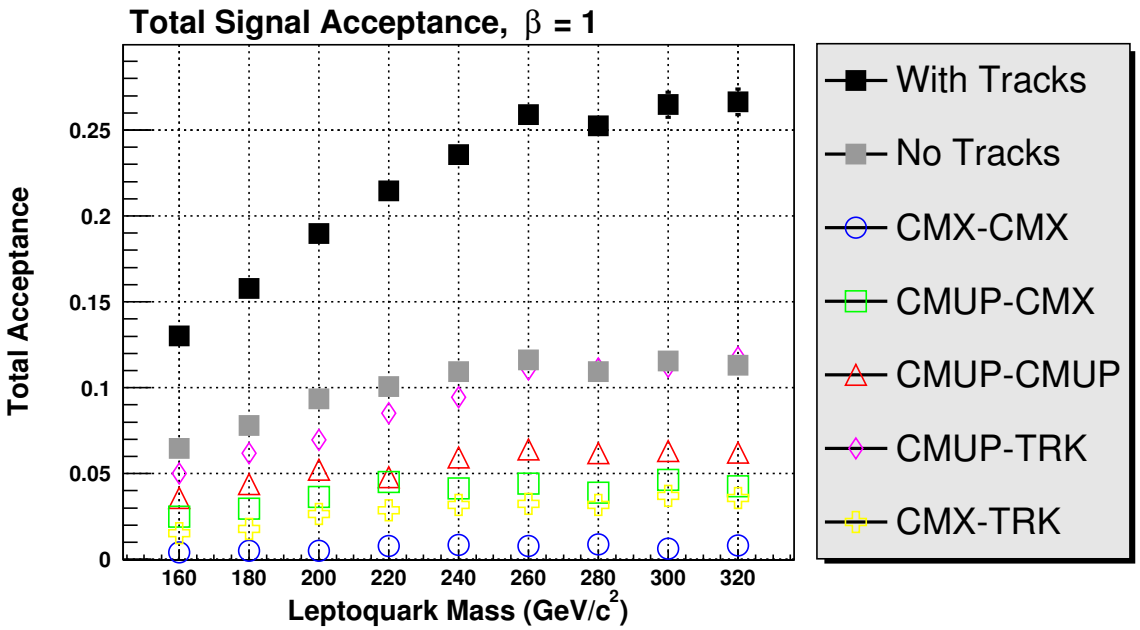

Figure 4.6: The total signal acceptance efficiencies for the $\mu q \mu q$ channel. The plot shows the contributions to the total acceptance (black) and the acceptance without TRK muons (grey) from the different muon detectors. The statistical errors are plotted.

in Figure 4.6. Keep in mind that to calculate the *total* acceptance, the final result is not the simple sum of these five types, instead we must combine five acceptances together with weighting factors:

$$A_{total} = A_{PP} \times \epsilon_{PP} + A_{PX} \times \epsilon_{PX} + A_{XX} \times \epsilon_{XX} + ... \tag{4.4}$$

The result of total acceptance for each leptoquark mass is listed in Table 4.12.

After our selection cuts, three events remain in the muon dataset. In Table 4.8 we report the number of events surviving each kinematical cut.

Kinematic Cut	$\mathbf{N_{obs}}$
2 muons with $p_T(\mu 1) > 25$ and $p_T(\mu 2) > 10$GeV/c	8029
2 jets with $E_T(j1) > 25$ and $E_T(j2) > 15$ GeV	147
Topology cut and $E_T(j1) + E_T(j2) > 50$ GeV	26
$M_T(\mu 1, \not\!\!E_T) \leq 25$ and $M_T(\mu 1, \mu 2, \not\!\!E_T) \leq 80$ GeV/c^2	4
Ht cut	3
Removal of events with $76 < M_{\mu\mu} < 110$ and $M_{\mu\mu} > 15$ GeV/c^2	3

Table 4.8: List of events passing the selection cuts in 361 pb^{-1} of data (From real dataset *bhmu0d*).

4.3 Background calculation in the *eqeq* and $\mu q \mu q$ channels

The main sources of background are due to $\gamma^*/Z \to e^+e^- + 2jets$ (for eqeq), $\gamma^*/Z \to \mu^+\mu^- + 2jets$ (for $\mu q \mu q$), $t\bar{t}$ production, W + $\geq$ 3 jets, cosmic ray events accompanied by jets due to radiation and events due to QCD/fakes. Other backgrounds from $b\bar{b}$, $Z \to \tau\tau$, W^+W^- are expected to be negligible due to the isolation cut and large lepton and jet transverse energy/p_T requirements. We list the results of the background calculation in Table 4.9.

4.3.1 DY + 2 jets

In the Drell-Yan process, which is the largest background contributor in the *eqeq* and $\mu q \mu q$ channels, a Z or photon is produced via quark-antiquark annihilation and decays leptonically into two electrons/muons. The additional jets in such events can come from other processes or from initial/final state radiation. Though the number of these events is abundant, they are easily accounted for since either the di-electron mass M_{ee} or dimuon mass $M_{\mu\mu}$, will peak approximately at the Z mass, M_Z. This background is eliminated

Process	N_{gen}	CDF dataset name	$\sigma \cdot BR$ (pb)	N_{exp}	Comments
$Z/\gamma* \to ee + jj$	100k	atop76	50.2 ± 0.09	1.72 ± 0.04	$10 < M_{ee} < 75$
	100k	atop4z	23.3 ± 0.03	0.84 ± 0.01	$75 < M_{ee} < 105$
	100k	atop71	0.631 ± 0.001	0.06 ± 0.002	$105 < M_{ee} < 800$
$Z/\gamma* \to \mu\mu + jj$	100k	atop86	65.5 ± 1.7	0.79 ± 0.05	$10 < M_{\mu\mu} < 75$
	100k	atop67	31.4 ± 1.0	0.16 ± 0.01	$75 < M_{\mu\mu} < 105$
	100k	atop72	1.04 ± 0.03	0.70 ± 0.05	$105 < M_{\mu\mu} < 800$
Top Production	100k	ttop0z	5.79 ± 0.04	0.14 ± 0.03	in eqeq
Top Production	100k	ttop0z	5.79 ± 0.04	1.04 ± 0.1	in $\mu q \mu q$
$W \to e\nu + 3p$	1M	ptop3w	5.59 ± 0.01	0.04 ± 0.01	in eqeq
$W \to \mu\nu + 3p$	1M	ptop8w	5.59 ± 0.01	0.05 ± 0.01	in $\mu q \mu q$
$Z/\gamma* \to \tau\tau + jj$	100k	atopxb	23.34 ± 0.03	negligible	both in eqeq and $\mu q \mu q$
QCD/Fakes	-	-	-	0.33 ± 0.33	from electron data
QCD/Fakes	-	-	-	0.29 ± 0.29	from muon data
Total	-	-	-	3.14 ± 0.25	in eqeq
	-	-	-	3.03 ± 0.20	in $\mu q \mu q$

Table 4.9: Significant background processes and signal contamination in eqeq and $\mu q \mu q$ channel.

by cuts on M_{ee} and $M_{\mu\mu}$; $\sum E_{T\ jets}$ cut helps too. Higher-order corrections allow the di-electron/dimuon mass to vary however, and it is necessary to calculate the Drell-Yan + 2jets cross section beyond leading order. For the same reason, although a di-electron/dimuon mass cut is effective in removing the majority of Drell-Yan processes, there will still be a significant number of events having a di-electron/dimuon mass shifted enough from M_Z to evade rejection. Moreover, as discussed in section 4.1.1, H_t is another effective cut to suppress Drell-Yan, especially in the higher E_T region where M_Z cut power is weakened.

We studied the distribution of this background by generating the process Z + 2 jets with ALPGEN [94] and using the Monte Carlo parton generator MCFM [78] to obtain the NLO cross section. (Note: $\gamma^*/Z \to e^+e^-$ and $\gamma^*/Z \to \mu^+\mu^-$ were separately generated and analyzed according to *eqeq* and $\mu q \mu q$ channel). In 361 pb^{-1} of data, we expect 2.62 ± 0.05 in *eqeq* channel, and 1.65 ± 0.02 events in $\mu q \mu q$ channel to be from DY + 2jets.

4.3.2 Top quark production: $t\bar{t}$

Another source of background is represented by $t\bar{t}$ production where both the W's decay into $e\nu$ or $\mu\nu$. If we look at the decay signature, top and third generation leptoquark in mode $\beta = 1$ are the same — both of them have 2 leptons, 2 jets and a large amount of missing Et. And, both of their decays are involved with b flavor quarks, which means b-tagging on jets won't be effective to filter them out. As discussed in section 4.1.1, the way to kill top

backgrounds from signal is by checking transverse variables. Although the final states are the same, the parent particle of two leptons in signature, W and τ, they have a different mass spectrum. The W boson, whose mass is around 80 GeV, is much heavier than the τ. Based on this difference, we made a series of checks on following transverse kinematic variables:

- $P_T(lepton1, \not\!\!E_T)$, defined as $\sqrt{(E_{lepton1}+ \not\!\!E_T)_x^{\ 2} + (E_{lepton1}+ \not\!\!E_T)_y^{\ 2}}$
- $P_T(lepton2, \not\!\!E_T)$
- $P_T(lepton1, lepton2)$
- $P_T(lepton1, lepton2, \not\!\!E_T)$
- $|\Delta\Phi(lepton1, \not\!\!E_T)|$, the angle between the first lepton and the missing Et
- $|\Delta\Phi(lepton2, \not\!\!E_T)|$
- $|\Delta\Phi(lepton1, lepton2)|$
- $|\Delta\Phi[P_T(lepton1, \not\!\!E_T), P_T(lepton2, \not\!\!E_T)]|$
- $M_T(lepton1, \not\!\!E_T)$, defined as the transverse mass of the first lepton and missing Et
- $M_T(lepton2, \not\!\!E_T)$
- $M_T(lepton1, lepton2, \not\!\!E_T)$

The performance of these variable checks varies with different channels. For examples, in the $eqeq$ channel $M_T(e1, \not\!\!E_T)$ and $M_T(e2, \not\!\!E_T)$ are good filters, while in the $\mu q \mu q$ channel $M_T(\mu 1, \not\!\!E_T)$ and $M_T(\mu 1, \mu 2, \not\!\!E_T)$ show the power of suppressing top backgrounds. Therefore, we need to set, tune and apply appropriate transverse cuts for each individual channel. We will mention this later in section 5.3 with $e\mu qq$ channel again.

We took 100K inclusive $t\bar{t}$ Monte Carlo events from the Top group ($M_{top} = 175$ GeV) as the study model. The expected number of background events from $t\bar{t}$ is 0.14 ± 0.03 for $eqeq$, 1.04 ± 0.1 for $\mu q \mu q$. To normalize simulated events to data we used the theoretical cross section for $t\bar{t}$, $\sigma(t\bar{t}) = 5.79$ pb.

4.3.3 W + jets

W+$\geq$ 3jets can be another background contributor, in case that the third jet is mismeasured and treated as the second lepton. From real data, as shown in Figure 4.7, it's clear to see that the region $20 < \not\!\!E_T/\text{GeV} < 40$ and fractional lepton isolation below 0.1 is heavily contaminated by W + jets events. However after applying two lepton ID cuts and setting a high threshold on $\sum E_T$, we are able to kill most of W+jets backgrounds.

W+$\geq$ 3jets was studied with a Monte Carlo sample from lepton+jets background, stripping from Top group. The expected number of background events from W+$\geq$ 3jets is 0.04 ± 0.01 for $eqeq$, 0.05 ± 0.01 for $\mu q \mu q$. To normalize simulated events to data we used the theoretical cross sections $\sigma(W \to e\nu + 3p) = 5.59$ pb, $\sigma(W \to \mu\nu + 3p) = 5.59$ pb.

4.3.4 QCD/Fakes

The QCD multijet background contaminates all leptoquark channels. In this section we estimate its contribution on the *$\mu q \mu q$channel* and the *eqeq* channel, and a similar strategy will be applied to the *$eq\mu q$* channel in the next chapter.

Let's start with the *$\mu q \mu q$* channel first. Since we have a muon stub-track match requirement in the muon selection procedure, the probability of energetic jets or pion decay being misidentified as "muons" and passing the trigger condition will be small, or negligible. However it's still a possible source of signal contamination, especially in the low $\not\!\!E_T$ region.

The method we used to estimate the QCD multijet background is to examine the phase-space of the $\not\!\!E_T$ versus the muon fractional isolation (Defined as E_T^{iso}/P_T in the cone with R = 0.4; from now on we denote it as $I_{0.4}$). This examination is for data events in which the muon isolation requirement is not enforced. Figure 4.7 shows the candidate events in the real dataset *bhmu0d* prior to any kinematic cuts.

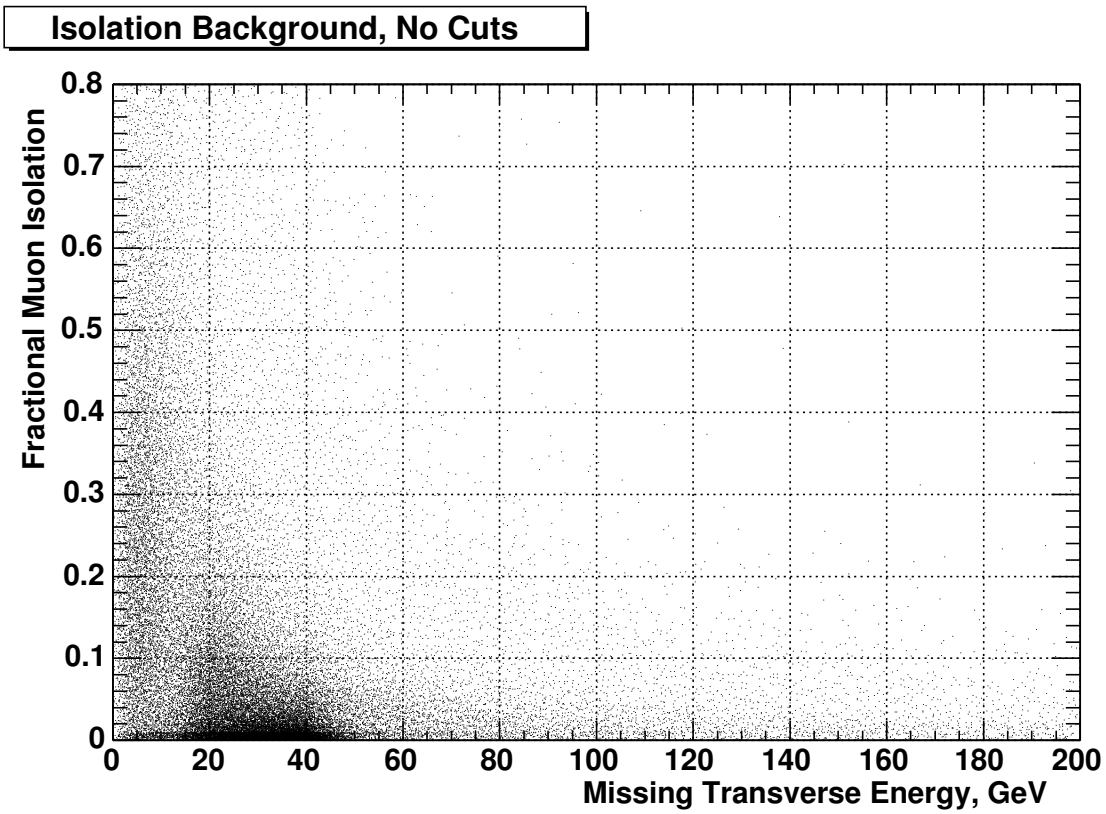

Figure 4.7: The fractional muon isolation versus $\not\!\!E_T$ in 361 pb^{-1} of data before any kinematic cuts. The QCD background dominates the region $\not\!\!E_T < 10$ GeV; the W + jets and ℓ+ jets dominates the region $10 < \not\!\!E_T/\text{GeV} < 60$.

Leptoquarks leave isolated high-p_T leptons and large missing transverse energy as decay products, therefore the region of $\not\!\!E_T > 60$ GeV and $I_{0.4} < 0.1$ is the signal region in Figure 4.7. We also see that the QCD multijet events dominate the region $\not\!\!E_T < 10$ GeV, while the $W+ \geq 2$ jets and $\ell+ \geq 2$ jets events dominate the region $10 < \not\!\!E_T/\text{GeV} < 60$.

We define four control regions as follows:

- Region I – $\not\!\!E_T > 60$ GeV, $I_{0.4} < 0.1$
- Region II – $\not\!\!E_T > 60$ GeV, $I_{0.4} > 0.2$
- Region III – $\not\!\!E_T < 10$ GeV, $I_{0.4} > 0.2$
- Region IV – $\not\!\!E_T < 10$ GeV, $I_{0.4} < 0.1$

If the lepton fractional isolation is not correlated with $\not\!\!E_T$ distribution, we can assume that the normalization factor between Region II and III will be same as the factor between Region I and IV. Therefore to estimate the number of QCD events in the signal region I $\not\!\!E_T > 60$ GeV, $I_{0.4} < 0.1$, we could calculate the number of QCD events in the region $\not\!\!E_T < 10$ GeV which defines the QCD contamination up to a normalization factor, followed by this relation:

$$N(\text{region I}) = N(\text{region IV}) \times \frac{N(\text{region II})}{N(\text{region III})}, \tag{4.5}$$

Figure 4.8 shows the events surviving the kinematic cuts before the transverse mass cut. The number of events in each region and the calculated QCD contamination is reported after each kinematic cut in Table 4.10. This sample is then further reduced by subtracting

Kinematic Cut	I	II	III	IV
$p_T(\mu 1) > 25$ and $p_T(\mu 2) > 10$ GeV	56922	755	52661	23193
$E_T(j1) > 25$ and $E_T(j2) > 15$ GeV	281	49	474	135
Topology Cuts	118	21	350	76
$\Sigma E_T(jets) > 50$ GeV	107	19	313	72
Ht cut	7	9	1	1
$M_T(\mu 1, \not\!\!E_T) \leq 25$ GeV/c^2	4	5	0	0
Z Mass Cut	2	0	0	0

Table 4.10: Events surviving the kinematic cuts in four control regions. The number of events surviving the mass cut in region I is for $M_{LQ} = 120$ GeV/c^2.

the contributions of the $W+ \geq 2$ jets and $\ell+$ jets backgrounds.

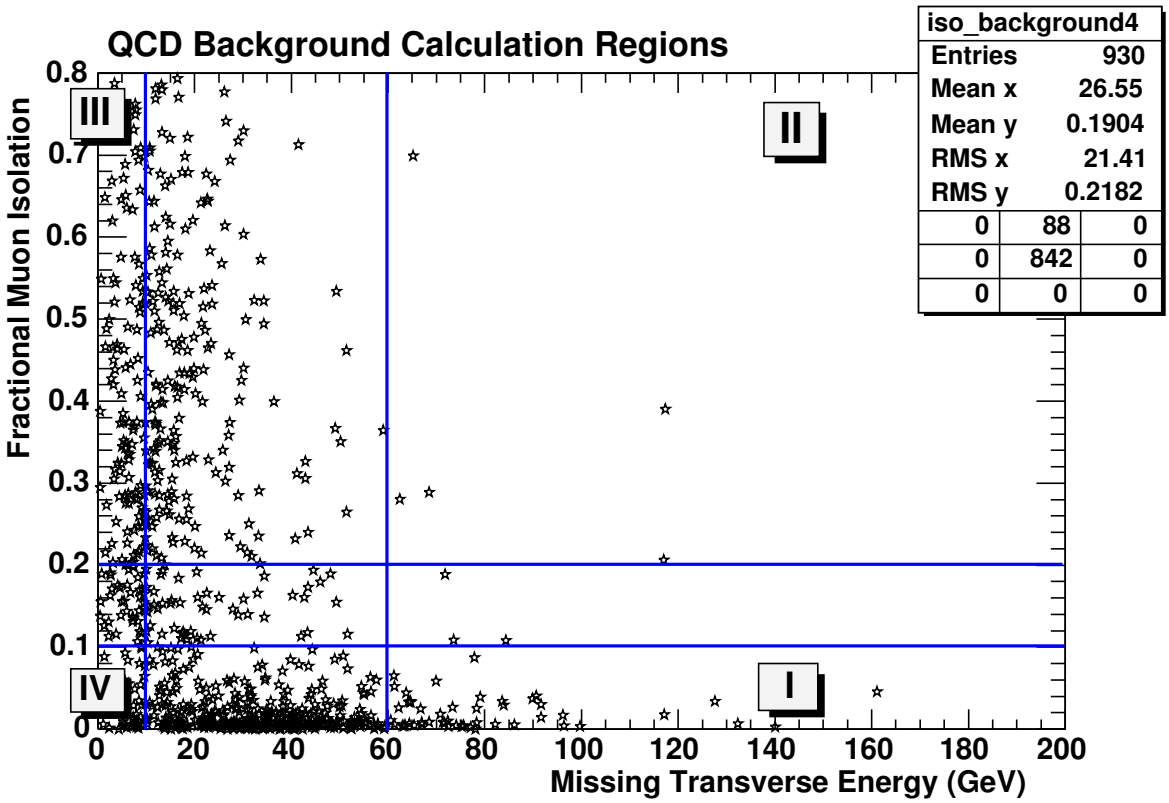

Figure 4.8: The fractional muon isolation versus $\not\!\!E_T$ in 361 pb^{-1} of data before the transverse mass cut.

The cut on the transverse mass reduces the number of events such that Equation 4.5 is not well behaved. To determine the final number of QCD background events, we calculate the ratio of events in the small $\not\!\!E_T$ region III and IV after the cut on $\Sigma E_T(jets)$. Assuming the *ratio* is independent of the transverse mass, this normalization factor can then be applied to the number of events in the high-$\not\!\!E_T$ region with large isolation to determine the number of QCD events in the signal region. However, the number of events in Region II surviving the mass cuts for all leptoquark mass contours is zero. We therefore estimate the number of QCD events in the signal region by applying the normalization factor to the error on the mean of the one-sigma Poisson distribution after the cut on transverse mass. We estimate 0.29 ± 0.29 QCD events in our data sample after all selection cuts in the $\mu q \mu q$ channel.

As for the *eqeq* channel, the procedure is the same except that it's applied to electron data instead of muon data. Figure 4.9 shows the candidate events in the real dataset *bhel0d* prior to any kinematic cuts.

From the plot we see a similar distribution like $\mu q \mu q$, however it seems that QCD multijet

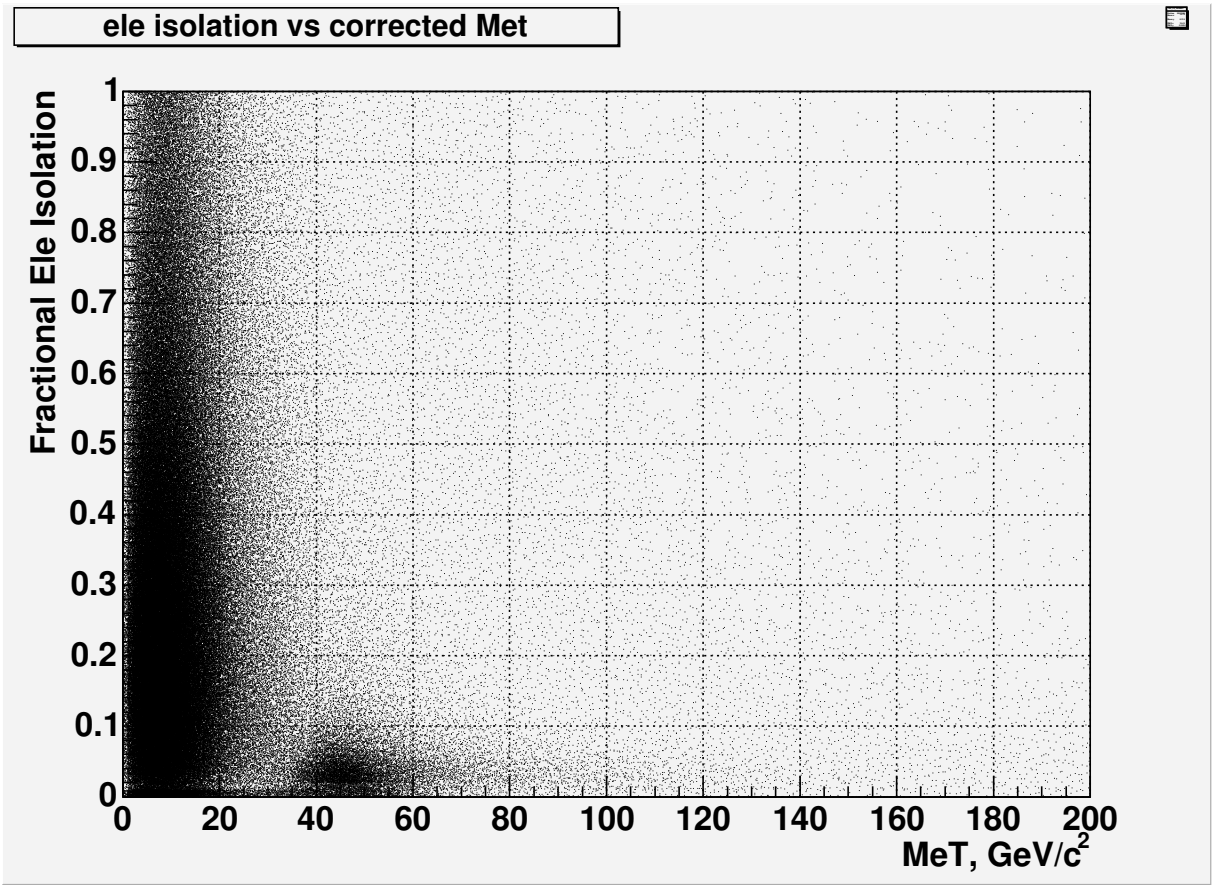

Figure 4.9: The fractional electron isolation versus $\not\!\!E_T$ in 361 pb^{-1} of data before any kinematic cuts. The QCD background dominates the region $\not\!\!E_T < 20$ GeV; the W + jets and ℓ+ jets dominates the region $20 < \not\!\!E_T/\text{GeV} < 60$.

background expands its boundary to $\not\!\!E_T$ - 20 GeV. Thus we define four control regions for *eqeq* channel as shown in Table 4.11:

Then we apply the same counting strategy and use fomula 4.5 again, eventually we estimate 0.33 ± 0.33 QCD events in our data sample after all selection cuts in the *eqeq* channel.

4.4 Systematic Uncertainty

The following systematic uncertainties are considered:

- Luminosity [65]: 5%
- Acceptance

Region	Condition
I	$\not\!\!E_T > 60$ GeV, $I_{0.4}/p_T < 0.1$
II	$\not\!\!E_T > 60$ GeV, $I_{0.4}/p_T > 0.2$
III	$\not\!\!E_T < 20$ GeV, $I_{0.4}/p_T > 0.2$
IV	$\not\!\!E_T < 20$ GeV, $I_{0.4}/p_T < 0.1$

Table 4.11: QCD background calculation regions in *eqeq* channel.

Mass	A(M_{LQ})%		Statistical%		Systematic%	Combined Rel.%
80	3.13	±	0.4	±	1.0	8.5
100	5.47	±	0.4	±	1.2	8.2
120	6.86	±	0.6	±	1.4	8.2
140	7.29	±	0.5	±	1.6	7.9
160	8.19	±	0.6	±	1.7	8.0
180	9.41	±	0.7	±	1.9	7.9
200	10.08	±	0.6	±	1.9	7.8
240	11.36	±	0.7	±	2.0	8.0
260	12.23	±	0.8	±	2.0	8.0

Table 4.12: The total acceptance percentages for each leptoquark mass in $\mu q \mu q$, listed with the statistical, systematic and combined relative errors.

  - PDF: 2.1%
  - Statistical Error of Monte Carlo: 2.2%
  - Jet Energy Scale: $< 1\%$

- Electron ID efficiency [90]
  - electron reconstruction: 0.5%
- Muon ID efficiency [21, 22]
  - muon reconstruction: 0.3%
- Event vertex cut [106]: 0.5%

Adding the above systematic uncertainty in quadrature will give a total systematic uncertainty of about 8%. The statistical, systematic, and combined relative errors are listed in Table 4.12.

4.5 Cross Section Upper Limit Calculation

In the analysis performed in the *eqeq* and $\mu q \mu q$ channel, the numbers of events surviving after all selection conditions are consistent with the expected numbers from backgrounds. This means we don't observe a new scalar leptoquark signal based on the current CDF II experiment.

Based on non-observation, we set an upper limit on the number of observed events, and so on the cross section of third generation scalar leptoquark production. By comparing the upper limit of the leptoquark cross section with the theoretical cross section for such leptoquarks, we exclude the mass region for which the theoretical cross section exceeds the observed upper limit.

The production cross section σ of the process $LQ\overline{LQ} \to \tau q \tau q \to eqeq$ and $LQ\overline{LQ} \to \tau q \tau q \to \mu q \mu q$ can be written as follows:

$$\sigma \times Br(\tau q \tau q \to eqeq) = \sigma \times \beta_1^2 = \frac{N}{\epsilon_{tot} \times \mathscr{L}} \tag{4.6}$$

$$\sigma \times Br(\tau q \tau q \to \mu q \mu q) = \sigma \times \beta_2^2 = \frac{N}{\epsilon_{tot} \times \mathscr{L}} \tag{4.7}$$

where β_1, β_2 are the branching ratios of tau decaying into electron and muon, respectively. N is the number of observed data events after our selection, ϵ_{tot} is the leptoquark mass-dependent total selection efficiency and $\mathscr{L}$ is the time-integrated measured luminosity. (Note, the $\tau q \tau q$ mode already took the $\beta = 1$ factor into consideration from leptoquark decay state.)

The upper limit on the observed leptoquark cross section is determined by estimating the number of possible leptoquark events observed for a specific probability or confidence level (CL):

$$\sigma^{lim} = \frac{N^{lim}}{\epsilon_{tot} \times \mathscr{L}}. \tag{4.8}$$

By taking Bayesian approach to calculate the 95% confidence level limits (Details about Bayes Statistical Method can be found in Appendix F), in Table 4.13 we report the expected number of events of signal in 361 pb^{-1} given the above efficiencies and the NLO theoretical cross section for different values of the renormalization/factorization scale is reported in Table 4.13. The second column shows the upper limit on the expected number of background subtracted signal events at 95% CL.

In the *eqeq* channel we find 4 candidate events and 3 events in $\mu q \mu q$ channel after selection. We set an upper limit on the scalar leptoquark cross section as a function of

Mass (GeV/c^2)	$N_{95\%}$	$Q^2 = M_{LQ}^2/4$	$Q^2 = 4M_{LQ}^2$
80	4.86	30.62	24.39
100	4.85	17.84	14.31
120	4.85	10.82	8.76
140	4.85	6.41	5.18
160	4.85	3.80	3.07
180	4.85	2.31	1.85
200	4.85	1.25	1.00
220	4.85	0.74	0.59
240	4.85	0.42	0.33

Table 4.13: The measured upper limit on the expected number of background subtracted signal events in 361 pb^{-1} for $LQ\overline{LQ} \to eqeq$. The right two columns show the theoretical expected number of scalar leptoquark events for different factorization/renormalization scales.

M_{LQ}. We calculate the upper limit on the observed leptoquark events, N^{lim}, at a 95% CL. The limit calculation was carried out using the `bayes.f` fortran code provided by the CDF statistics committee [14] which follows the previously discussed Bayesian prescription for calculating upper limits.

In Table 4.14 we report the $\beta = 1$ values of the cross-section limits in $eqeq$ and $\mu q \mu q$ for each M_{LQ} and the theoretical calculations at NLO for pair production of scalar leptoquarks at the Tevatron using the CTEQ6.1 PDF with different choices of scale. In Figure 4.10 the

Mass (GeV/c^2)	95% CL σ (pb)	σ Theory CTEQ6.1 (pb)	
		$Q^2 = M_{LQ}^2/2$	$Q^2 = 2M_{LQ}^2$
80	0.524E+02	0.601E+02	0.441E+02
100	0.158E+02	0.179E+02	0.134E+02
120	0.573E+01	0.640E+01	0.494E+01
140	0.238E+01	0.263E+01	0.207E+01
160	0.108E+01	0.119E+01	0.947E+00
180	0.525E+00	0.557E+00	0.460E+00
200	0.268E+00	0.293E+00	0.235E+00
220	0.141E+00	0.154E+00	0.124E+00
240	0.762E-01	0.832E-01	0.664E-01
260	0.419E-01	0.457E-01	0.364E-01

Table 4.14: Values of the upper limits at 95% CL of the production cross-section of third generation leptoquarks decaying into $\mu q \mu q$ as a function of M_{LQ}. The last 2 columns on the right report the result of the theoretical calculations at Next-To-Leading order with CTEQ6.1 for different choices of the scale multiplied by a factor of $\beta = 1$.

limit cross-section as a function of M_{LQ} is compared with the theoretical expectations for *eqeq*, and in Figure 4.11 the limit cross-section as a function of M_{LQ} is compared with the theoretical expectations for $\mu q \mu q$.

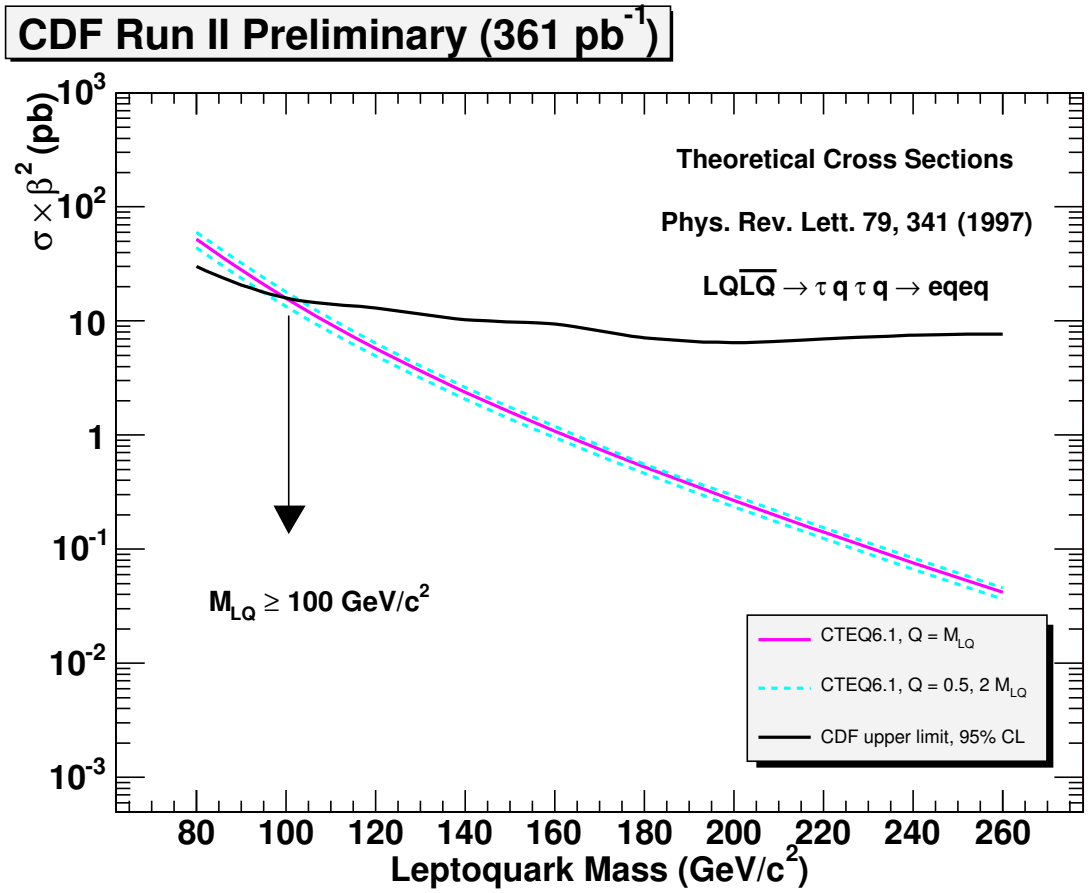

Figure 4.10: Limit cross-section as a function of M_{LQ} compared with the theoretical expectations calculated at NLO accuracy. At the intersection points between experimental and theoretical curves we find a lower limit on M_{LQ} at 100 GeV/c^2.

At the intersection point between experimental and theoretical curves we find the lower limit on M_{LQ} at 100 GeV/c^{2}for the *eqeq* channel and 108 GeV/c^{2}for the $\mu q \mu q$ channel.

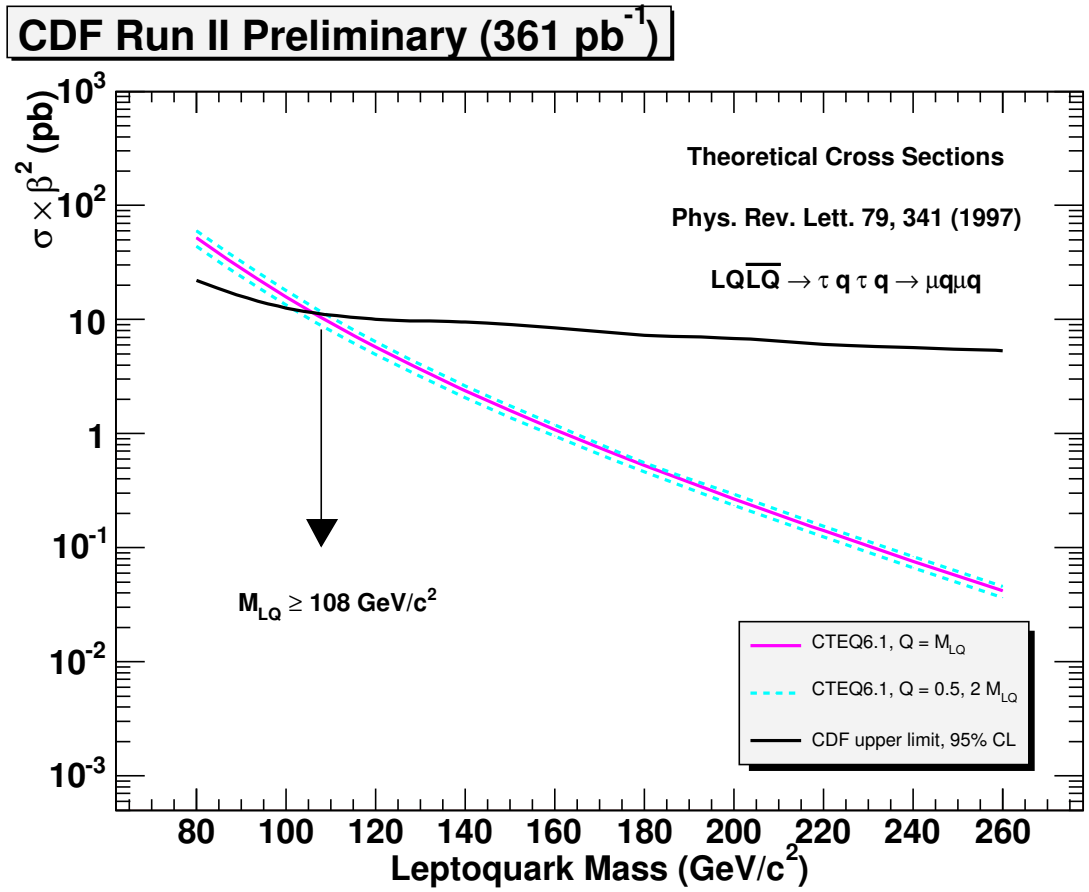

Figure 4.11: Limit cross-section as a function of M_{LQ} compared with the theoretical expectations calculated at NLO accuracy. At the intersection points between experimental and theoretical curves we find a lower limit on M_{LQ} at 108 GeV/c^2.

Chapter 5

Search for Scalar Leptoquarks in the $eq\mu q$ Channel

In this chapter a search for pair-produced scalar leptoquarks decaying into $eq\mu q$ is presented. A preselection efficiency and a kinematic acceptance efficiency are separately calculated and then combined to determine a total leptoquark signal acceptance efficiency. An estimate of the expected number of background events in this channel is then calculated. Next, an outline of the systematic uncertainties in the signal acceptance and data sample is presented. The chapter concludes with a calculation of the upper limit on the leptoquark cross section. Finally, the theoretical scalar leptoquark cross section is compared with this upper limit and a new scalar leptoquark mass exclusion limit in the $eq\mu q$ channel is presented.

5.1 Event-type efficiency calculation

The experimental signature of a third generation scalar leptoquark for the $\tau q \tau q \to eq\mu q$ case consists of one isolated high-p_T electron, plus one isolated medium-p_T muon, and two energetic jets. The full data sample is reduced by preselecting events according to the criteria described in Appendix E. Each event is required to have one tight central electron, followed by one muon of type CMUP or CMX.

The efficicency of tight electron ID is discussed in section 3.5.1. Regarding muon type efficiency, we have:

$$\epsilon_{CMUP} = \epsilon_{trig}^{CMUP} \times \epsilon_{fid} \times \epsilon_{reco}^{CMUP} \times \epsilon_{ID}^{CMUP} \times \epsilon_{iso}^{CMUP} \quad (5.1)$$

$$\epsilon_{CMX} = \epsilon_{trig}^{CMX} \times \epsilon_{fid} \times \epsilon_{reco}^{CMX} \times \epsilon_{ID}^{CMX} \times \epsilon_{iso}^{CMX} \quad (5.2)$$

Using the values from Table 3.5, in this $e\mu qq$ channel we determine the lepton event-type efficiencies as:

Event-type Efficiencies, $eq\mu q$ channel	
$\epsilon_{tight\ ele}$	0.825 ± 0.05
$\epsilon_{CMUP} =$	0.695 ± 0.009
$\epsilon_{CMX} =$	0.837 ± 0.008

5.2 Acceptance and kinematical efficiency calculation

After event preselection, the number of events is further reduced in order to discriminate the leptoquark signal from the backgrounds discussed in Section 4.3. Because the leptoquark mass is relatively higher than the masses associated with the backgrounds, the leptoquark signal is characterized by one tight central electron, one central medium muon, and two energetic jets. The discriminating cuts are optimized to give the highest limit results. As a result the following cuts are placed:

- One electron with $E_T > 25$ GeV and one muon with $p_T(\mu) > 10$ GeV/c.
  This cut selects two identified leptons. It ensures that the electron and the following muon is a properly triggered physics object. The energy threshold set here can reduce QCD background greatly. The leading electron E_T distribution and leading muon p_T distribution for a leptoquark mass of 120 GeV/c^2 are shown in Figure 5.1.

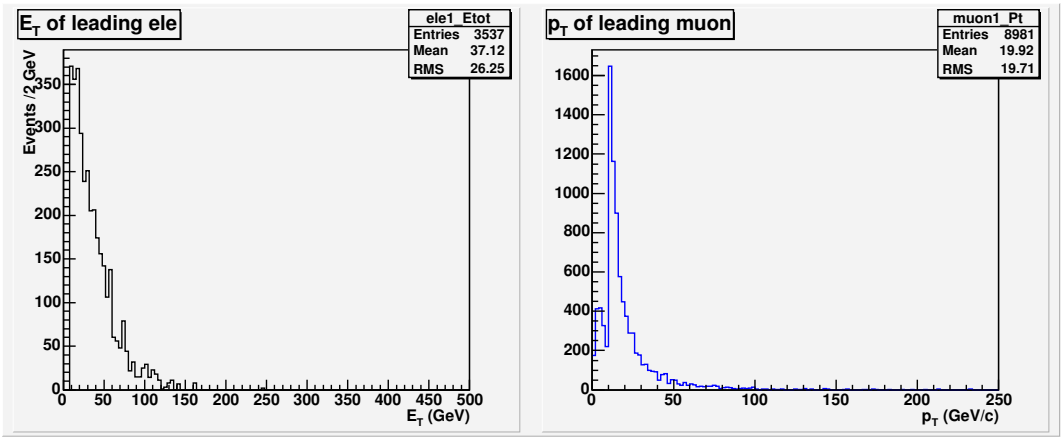

Figure 5.1: E_T and P_T distributions for leading electrons (left) and muon (right) for $M_{LQ} = 120$ GeV/c^2.

- Two jets with $E_T(j1) > 25$, $E_T(j2) > 15$ GeV and $E_T(j1) + E_T(j2) > 50$ GeV.

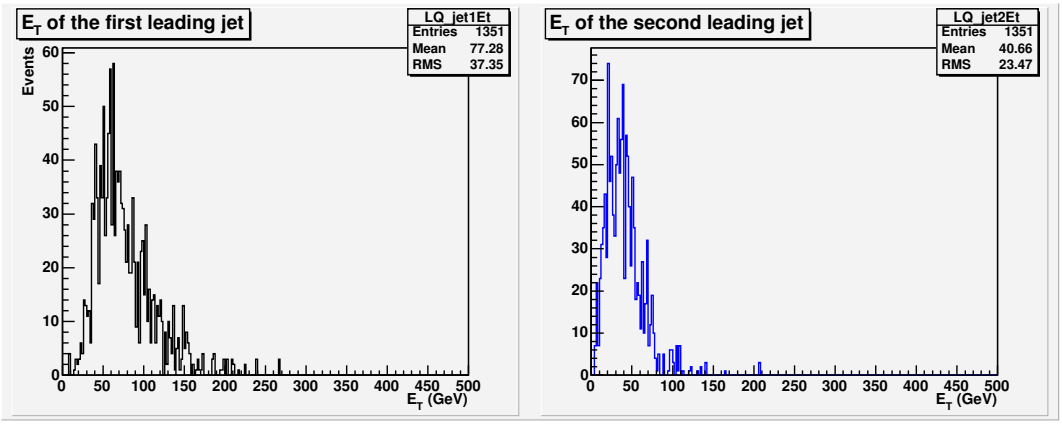

Figure 5.2: E_T distributions for the first leading jet (left) and the second leading jet (right), for $M_{LQ} = 120$ GeV/c^2.

- Topology cut: $\Delta\phi(leptons + jets, \not\!\!E_T) > 120°$, $\Delta\phi(leadingjets, \not\!\!E_T) > 5^o$
  This topology cut rejects events in which the jets are not isolated from the neutrino. Also the angle cut is mainly to filter the Drell-Yan background out. Due to the lack of neutrinos, Drell-Yan won't have a balanced $\not\!\!E_T$ with leptons plus jets. The balanced situation is more or less like a back-to-back case (180°). Here, after cut optimization, we set the lower limit of the angle between muons plus jets and missing transverse energy at 120 degrees.

- Transverse kinematic variables cut
  The purpose of this cut is to suppress the top production backgrounds. Top decays into W and b quark, while W decays to leptons. e.g. $W \to e\nu$ or $W \to e\nu$. On the other hand, the third generation leptoquark decays to τ and b, while τ decays to neutrinos and an electron or a muon. Hence the different mass spectra of the W and the τ becomes the key to filter top backgrounds out of the signal, and that is the motivation for transverse kinematic variable check here. More details about this check are already discussed in section 4.3.2. After cut optimization, we set $M_T(\mu, \not\!\!E_T) \leq 20GeV$ and $M_T(e, \mu, \not\!\!E_T) \leq 80GeV$ as the cut condition. See distribution plot in Figure 5.3.

  Furthermore, unlike in $eqeq$ and $\mu q\mu q$ where Drell-Yan + 2 jets dominates the background. $t\bar{t}$ production is the main background contributor in $eq\mu q$ channel. Since Drell-Yan process cannot produce a pair of leptons with different flavors, there is no signature like one electron plus one muon in Drell-Yan decay. Leptoquark decay doesn't have such a limitation. Therefore the transverse variable cut plays a more important role in this channel.

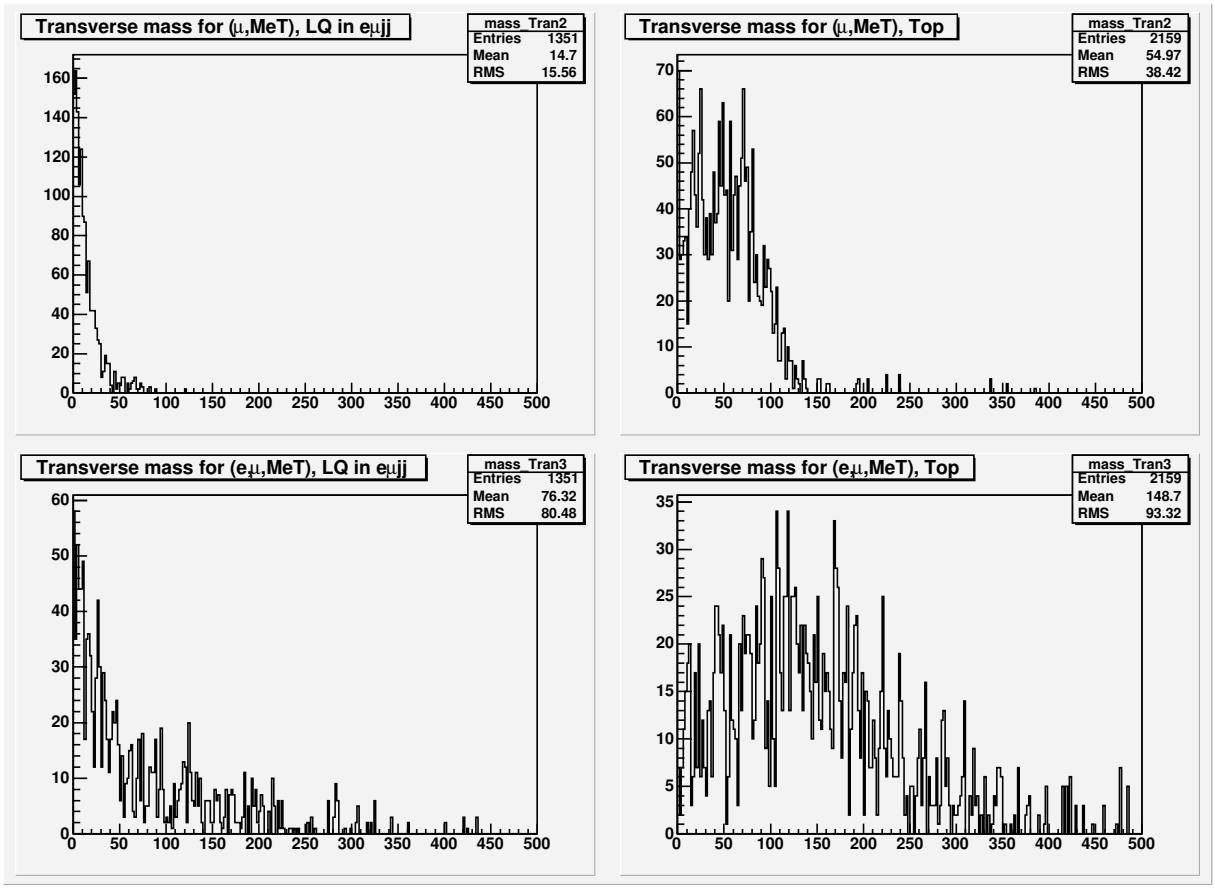

Figure 5.3: Transverse mass distributions for $M_{LQ} = 120$ GeV/c^2. (left two) and the inclusive top (right two).

- H_t cut - Definition and method is similar to the one we used in *eqeq* and $\mu q \mu q$:
  Et_sum $= E_{T\,e} + p_{T\,\mu} + E_{T\,j1} + E_{T\,j2}$
  Ht_mag $= \sqrt{(E_e + E_\mu + E_{j1} + E_{j2})_x^{\,2} + (E_e + E_\mu + E_{j1} + E_{j2})_y^{\,2}}$

  Except that we set Et_sum $\leq$ 4.0 * Ht_mag + 50.0 for the best ratio of S/B in this channel.

- Removal of events with $75 < M_{e\mu}/\mathrm{GeV/c^2} < 105$ and $M_{e\mu} < 15$ GeV/c^2
  We don't expect the combination of electron and muon can form a Z mass peak. However we still put this cut in the end to avoid mis-identification from leptons (e.g. A fake electron from muon event).

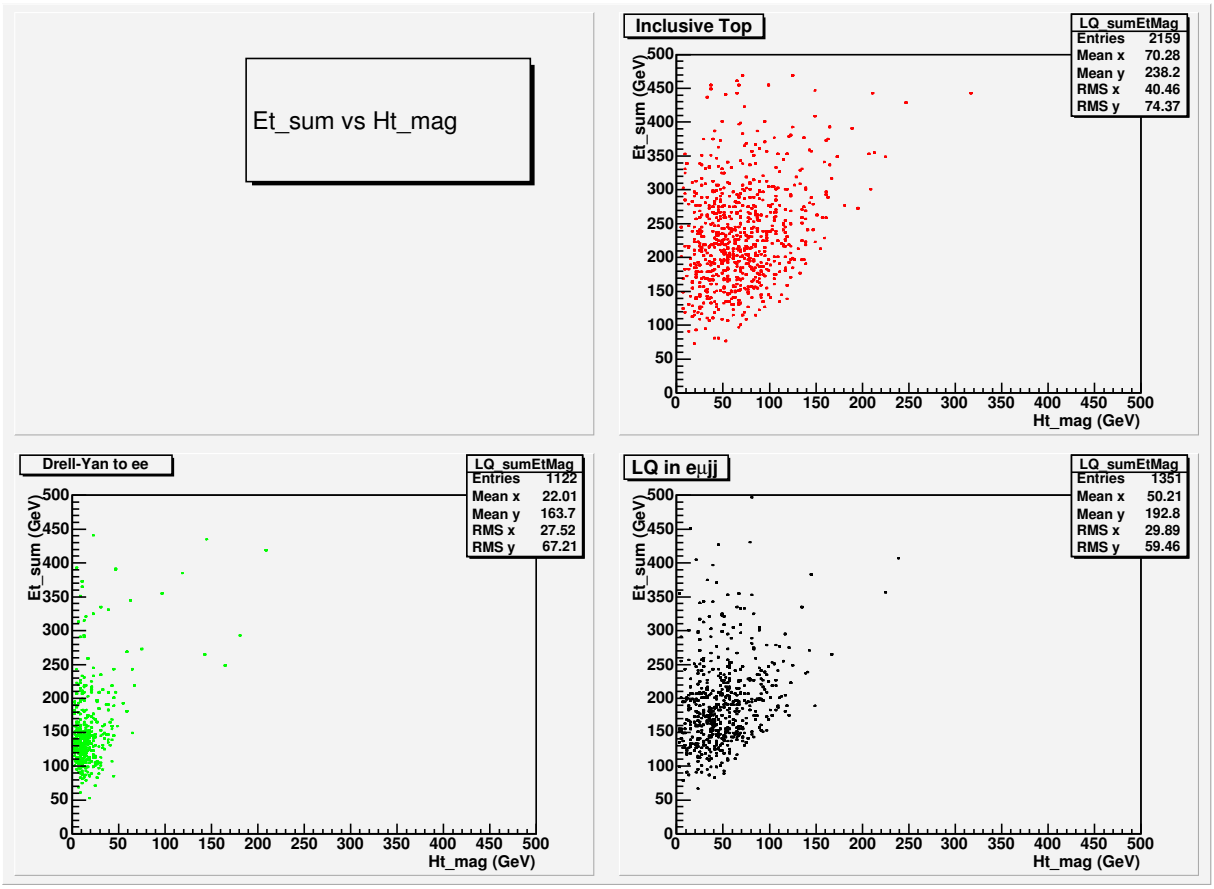

Figure 5.4: Et_sum v.s. Ht_mag, comparison among Inclusive Top (right top), Drell-Yan to di-electron + 2jets(left bottom), and Leptoquark mass @ 120 GeV in $eq\mu q$ (right bottom). The size of the bins is 1 GeV by 1 GeV

5.2.1 Total Acceptances

The analysis cut efficiencies are calculated relative to the number of events of type CMUP or CMX and are reported in Figure 5.5 and Table 5.1. The analysis cut efficiencies are then folded with the Z-vertex cut (fiducial) [106], trigger [111], muon reconstruction, and fractional isolation cut efficiencies. The expected number of signal events in 361 pb^{-1}, given the above efficiencies and the NLO theoretical cross section for different values of the renormalization/factorization scale, is reported in Table 5.2.

Mass (GeV/c^2)	CMUP $\pm$ stat $\pm$ sys(%)	CMX $\pm$ stat $\pm$ sys (%)	Total $\pm$ stat $\pm$ sys (%)
80	2.86 $\pm$ 0.02 $\pm$ 0.16	0.82 $\pm$ 0.01 $\pm$ 0.09	3.68 $\pm$ 0.03 $\pm$ 0.25
100	3.82 $\pm$ 0.03 $\pm$ 0.19	1.36 $\pm$ 0.02 $\pm$ 0.11	5.18 $\pm$ 0.05 $\pm$ 0.30
120	3.98 $\pm$ 0.03 $\pm$ 0.25	1.44 $\pm$ 0.02 $\pm$ 0.12	5.42 $\pm$ 0.05 $\pm$ 0.37
140	4.59 $\pm$ 0.05 $\pm$ 0.31	1.59 $\pm$ 0.02 $\pm$ 0.13	6.18 $\pm$ 0.07 $\pm$ 0.44
160	5.36 $\pm$ 0.07 $\pm$ 0.41	1.97 $\pm$ 0.03 $\pm$ 0.16	7.33 $\pm$ 0.10 $\pm$ 0.57
180	6.79 $\pm$ 0.09 $\pm$ 0.50	2.66 $\pm$ 0.04 $\pm$ 0.20	9.45 $\pm$ 0.13 $\pm$ 0.70
200	7.73 $\pm$ 0.10 $\pm$ 0.54	3.15 $\pm$ 0.04 $\pm$ 0.22	10.9 $\pm$ 0.14 $\pm$ 0.76
220	9.14 $\pm$ 0.12 $\pm$ 0.62	3.39 $\pm$ 0.05 $\pm$ 0.23	12.5 $\pm$ 0.17 $\pm$ 0.85
240	8.76 $\pm$ 0.11 $\pm$ 0.59	3.57 $\pm$ 0.05 $\pm$ 0.24	12.3 $\pm$ 0.16 $\pm$ 0.83
260	10.2 $\pm$ 0.13 $\pm$ 0.68	4.14 $\pm$ 0.06 $\pm$ 0.28	14.3 $\pm$ 0.19 $\pm$ 0.96

Table 5.1: Kinematic efficiency as a function of the leptoquark mass.

Mass (GeV/c^2)	$N_{95\%}$	Expected Events $\times\beta$	
		$Q^2 = M_{LQ}^2/2$	$Q^2 = 2M_{LQ}^2$
140	5.51	13.64	10.72
160	5.20	8.63	6.88
180	4.48	5.34	4.28
200	3.04	3.10	2.51
220	3.04	1.87	1.51
240	3.04	0.99	0.80
260	3.04	0.64	0.51

Table 5.2: The measured upper limit on the expected number of background subtracted signal events in 361 pb^{-1} for $LQ\overline{LQ} \to eq\mu q$. The right two columns show the theoretically expected number of scalar leptoquark events for different factorization/renormalization scales.

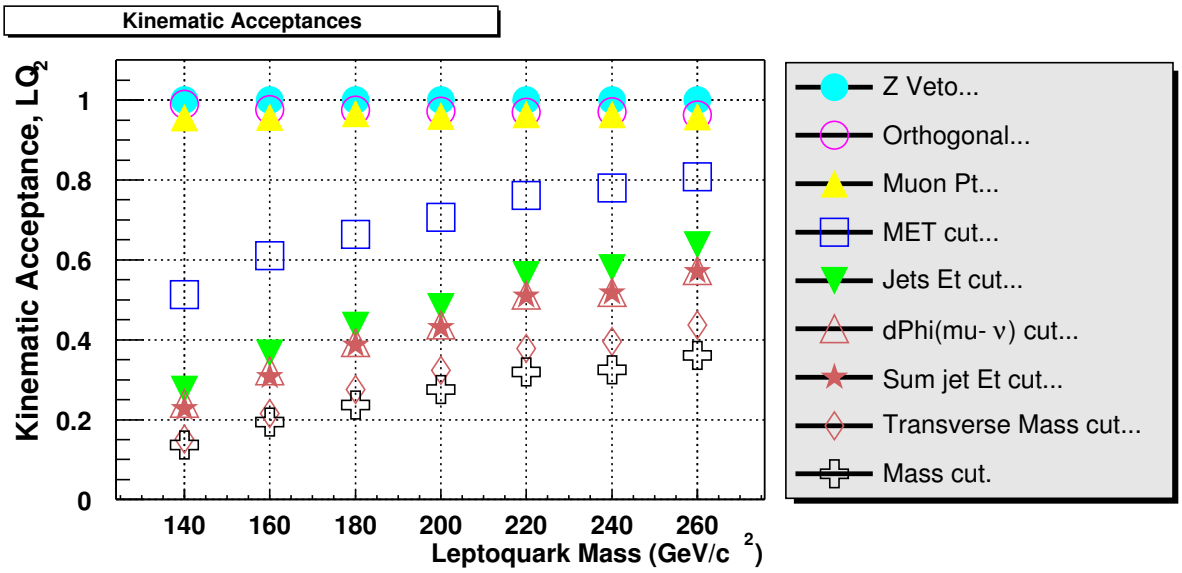

Figure 5.5: Cumulative efficiencies of the kinematic cuts for a range of leptoquark masses. The statistical errors are plotted.

5.3 Background calculation in the $eq\mu q$ channel

The main sources of background are due to $t\bar{t}$ production, $W+ \geq 3$jets with $W \to \mu\nu$ or $W \to e\nu$, Drell-Yan + 2jets, cosmic ray events accompanied by jets due to radiation and events due to QCD/fakes. Other backgrounds from $b\bar{b}$, $Z \to \tau\tau$, W^+W^- are expected to be negligible due to the isolation cut and large lepton and jet transverse energy requirements. Table 5.3 summarizes the background estimation in the $eq\mu q$ sample.

The following Monte Carlo samples are generated to determine the number of expected background events in the data sample:

- $t\bar{t}$ production

  As discussed in previous section 5.2, instead of Drell-Yan, in the $eq\mu q$ channel the major source of background is represented by $t\bar{t}$ production where both the W's decay into $e\nu$ and $\mu\nu$. If we look at the decay signature, the top and the third generation leptoquark in mode $\beta = 1$ are the same — both of them have 2 leptons, 2 jets and a large amount of missing Et. And, both of their decays are involved with b flavor quarks, which means b-tagging on jets won't be effective to filter them out. Table 5.4 shows the acceptance comparison between the selection with b-tagging and without b-tagging. The result shows that adding b-tagging into selection criteria does not result in a significant boost in the selection efficiency. Instead, adding b-tagging gives us a slightly worse S/B ratio when comparing the numbers of signal and background

$M_{LQ} = 120$ GeV/c^2					
Process	N_{gen}	CDF dataset name	$\sigma \cdot BR$ (pb)	N_{exp}	Comments
Top Production	100k	ttop0z	5.79 ± 0.04	0.87 ± 0.1	
$Z/\gamma* \to ee + jj$	100k	atop76	50.2 ± 0.09	1.26 ± 0.1	$10 < M_{ee} < 75$
	100k	atop4z	23.3 ± 0.03	0.76 ± 0.05	$75 < M_{ee} < 105$
	100k	atop71	0.631 ± 0.001	0.05 ± 0.002	$105 < M_{ee} < 800$
$W \to e\nu + 3p$	1M	ptop3w	5.59 ± 0.01	0.24 ± 0.05	
$W \to \mu\nu + 3p$	1M	ptop8w	5.59 ± 0.01	0.05 ± 0.01	
$Z/\gamma* \to \tau\tau + jj$	100k	atopxb	23.34 ± 0.03	negligible	
QCD/Fakes	-	-	-	0.29 ± 0.29	from data
Total	-	-	-	3.54 ± 0.55	

Table 5.3: The background processes considered for the signal contamination. The expected background events column shows values obtained for a leptoquark mass $M_{LQ} = 120$ GeV/c^2.

	Acceptance (LQ)	Expected number (LQ)	Top acceptance (Top)	Expected number (Top)	S/B
B-tagging ON	5.01%	6.42	0.036%	0.783	1.83
B-tagging OFF	5.42%	6.94	0.04%	0.87	1.96

Table 5.4: The efficiency comparison between b-tagging method and non b-tagging in $eq\mu q$ channel. Signal sample is LQ Monte Carlo @ 120 GeV. All expected numbers are normalized to 361 pb^{-1} as same as data. S/B ratio in the table includes all backgrounds, not the top events only.

events passing the cut.

As discussed in section 4.1.1, the way to kill top backgrounds from signal is by checking transverse variables. Although the final states are the same, the parent particle of the two leptons in the signature, W and τ, have a different mass spectrum. The W boson, whose mass is around 80 GeV, is much heavier than the τ. Based on this difference, we made a series of checks on following transverse kinematic variables:

- $P_T(e, \not\!\!E_T)$, defined as $\sqrt{(E_{electron} + \not\!\!E_T)_x^{\,2} + (E_{electron} + \not\!\!E_T)_y^{\,2}}$
- $P_T(\mu, \not\!\!E_T)$
- $P_T(e, \mu)$
- $P_T(e, \mu, \not\!\!E_T)$
- $|\Delta\Phi(e, \not\!\!E_T)|$, the angle between the electron and the missing Et
- $|\Delta\Phi(\mu, \not\!\!E_T)|$
- $|\Delta\Phi(e, \mu)|$
- $|\Delta\Phi[P_T(e, \not\!\!E_T), P_T(\mu, \not\!\!E_T)]|$

- $M_T(e, \not\!\!E_T)$, defined as the transverse mass of the electron and missing Et
- $M_T(\mu, \not\!\!E_T)$
- $M_T(e, \mu, \not\!\!E_T)$

For the $eq\mu q$ channel $M_T(\mu, \not\!\!E_T)$ and $M_T(e, \mu, \not\!\!E_T)$ are effective filters to suppress top backgrounds, as shown in Figure 5.3. Other transverse variables are compared the chapter Appendix G.

Moreover, we found that the behavior of transverse mass $M_T(\mu, \not\!\!E_T)$ and $M_T(e, \mu, \not\!\!E_T)$ doesn't vary too much by changing the mass of the leptoquark in the Monte Carlo, so we keep the fixed mass cut condition among all samples. Figure 5.6 compares the sample with $M_{LQ} = 120$ GeV/c^{2}and $M_{LQ} = 220$ GeV/c^2.

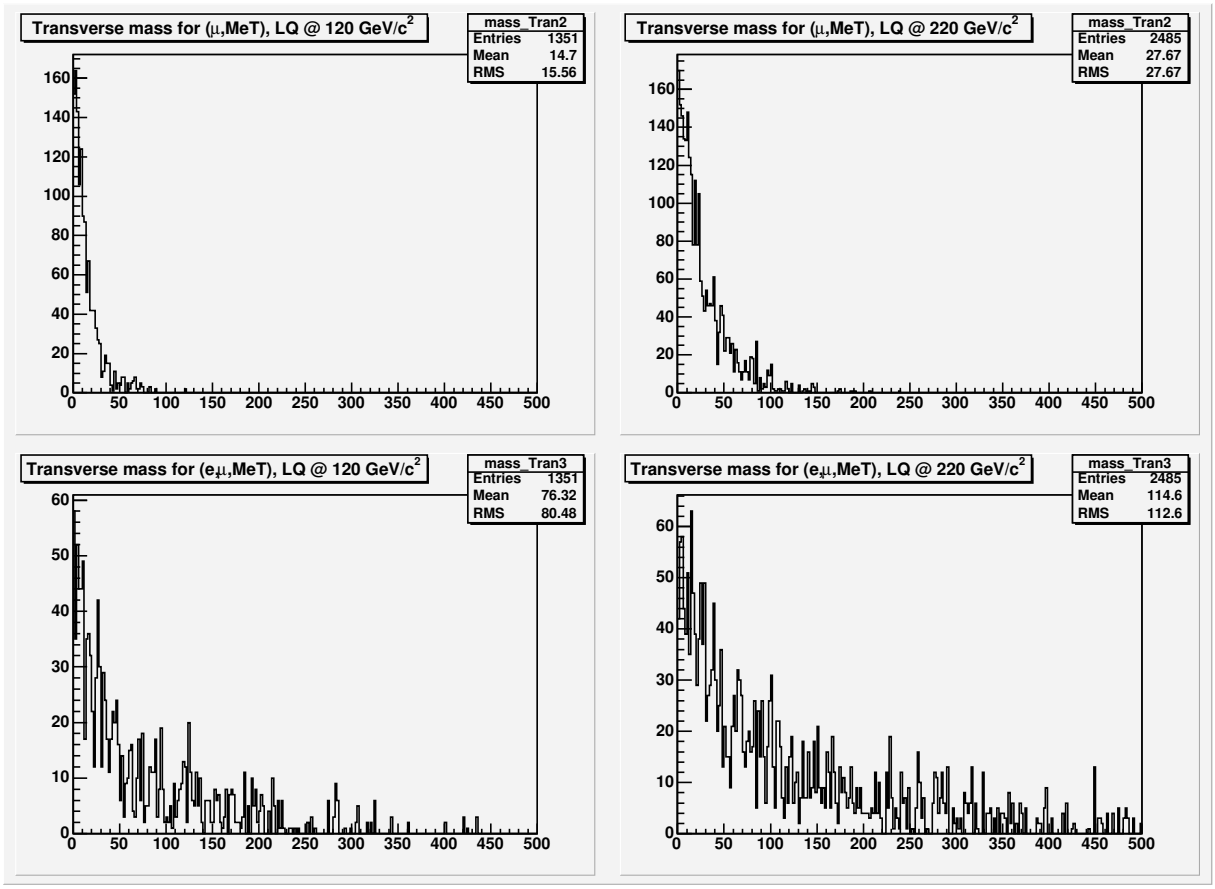

Figure 5.6: Transverse mass distribution plot from $M_{LQ} = 120$ GeV/c^2. (Left two) and $M_{LQ} = 220$ GeV/c^2(right two).

We took 100K inclusive $t\bar{t}$ Monte Carlo events from the Top group ($M_{top} = 175$ GeV)

as the study model. The expected number of background events from $t\bar{t}$ is 0.87 ± 0.1. To normalize simulated events to data we used the theoretical cross section for $t\bar{t}$, $\sigma(t\bar{t}) = 5.79$ pb.

- Drell-Yan + 2jets

  Because the Drell-Yan process can not produce two leptons with different flavor such as one electron plus one muon, it is no longer the dominant background contributor in the $eq\mu q$ channel. However, the effect still can not be totally neglected (In fact in the lower Z mass sample, it still has a significant contribution to backgrounds). So again, as we did for $eqeq$ and $\mu q\mu q$, we studied the distribution of this background by generating the process Z + 2 jets with ALPGEN [94] and using the Monte Carlo parton generator MCFM [78] to obtain the NLO cross section. This time we need to consider $\gamma^*/Z \to e^+e^-$ and $\gamma^*/Z \to \mu^+\mu^-$ together since both processes could make background contributions in the $eq\mu q$ channel. However the result turns out that the contribution from $\gamma^*/Z \to \mu^+\mu^-$ is trivial, since fake electrons from $\gamma^*/Z \to \mu^+\mu^-$ barely passed the first tight ele ID selection.

  In 361 pb^{-1} of data, we expect 2.07 ± 0.08 events from $\gamma^*/Z \to e^+e^-$, 0.007 ± 0.001 events from $\gamma^*/Z \to \mu^+\mu^-$, altogether 2.08 ± 0.08 events from DY + 2jets.

- $W+ \geq$ 3jets

  W+$\geq$ 3jets can be another background contributor, in case the third jet is mis-measured and treated as the second lepton. From real data, as shown in Figure 4.7, it's clear that the region $20 < \not\!\!E_T/\text{GeV} < 40$ and fractional lepton isolation below 0.1 is heavily contaminated by W + jets events. However after applying two lepton ID cuts and setting a high threshold on $\sum E_T$, we are able to kill most of W+jets backgrounds.

  W+$\geq$ 3jets were studied with the Monte Carlo sample from lepton+jets background, stripping from the Top group. The expected number of background events from $W \to e\nu + 3p$ is 0.24 ± 0.02, and from $W \to \mu\nu + 3p$ is 0.05 ± 0.01. Altogether we expect 0.29 ± 0.03 events to be from W + $\geq$ jets.

  To normalize simulated events to data we used the theoretical cross section $\sigma(W \to e\nu + 3p) = 5.59$ pb, $\sigma(W \to \mu\nu + 3p) = 5.59$ pb.

- QCD/Fakes

  The QCD multijet background is estimated by examining the phase-space of the $\not\!\!E_T$ vs the lepton fractional isolation for data events in which the lepton isolation requirement is not enforced. The evaluation method is same as the one used in the $eqeq$ and the

	80	120	160	200	240
$t\bar{t}$	1.69 ± 0.21	1.84 ± 0.23	1.35 ± 0.17	1.00 ± 0.37	0.80 ± 0.29
Z+ jets	0.18 ± 0.01	0.22 ± 0.02	0.19 ± 0.01	0.18 ± 0.01	0.14 ± 0.01
QCD multijet	0.29 ± 0.29	0.29 ± 0.29	0.29 ± 0.29	0.29 ± 0.29	0.29 ± 0.29
Total	3.09 ± 0.35	3.74 ± 0.36	3.22 ± 0.34	3.08 ± 0.33	2.83 ± 0.32
Data	4	4	4	3	2

Table 5.5: The final events calculated for expected backgrounds and observed events in the data for several scalar leptoquark masses.

$\mu q \mu q$ channels. (See previous discussion in section 4.3.4). The result of QCD/Fake estimation is reported in Table 5.3.

Table 5.5 shows the estimated background events and the number of events surviving selection.

5.4 Systematic uncertainty

The following systematic uncertainties are considered:

- Luminosity [65]: 6%
- Acceptance
  - PDF: 2.1%
  - ISR/FSR: 1.8%
  - Statistical Error of Monte Carlo: 2.2%
  - Jet Energy Scale: $< 1\%$
- Lepton ID efficiency [90, 21, 22]
  - electron reconstruction: 0.5%
  - muon reconstruction: 0.3%
- Event vertex cut [106]: 0.5%

Adding the above systematic uncertainties in quadrature will give a total systematic uncertainty of about 7-8%. The statistical, systematic, and combined relative errors are listed in Table 5.6.

Mass	A(M_{LQ})%	±	Statistical%	±	Systematic%	Combined Rel.%
80	3.68	±	0.07	±	0.44	8.44
100	5.18	±	0.10	±	0.58	7.92
120	5.42	±	0.13	±	0.72	7.61
140	6.18	±	0.2	±	0.8	7.23
160	7.33	±	0.2	±	0.9	7.01
180	9.45	±	0.2	±	0.9	6.93
200	10.9	±	0.2	±	1.0	6.91
220	12.5	±	0.3	±	1.2	6.77
240	12.3	±	0.3	±	1.2	6.79
260	14.3	±	0.4	±	1.3	6.25

Table 5.6: The total acceptance percentages for each leptoquark mass listed with the statistical, systematic and combined relative errors.

5.5 Cross section limit

The production cross section σ of the process $LQ\overline{LQ} \to eq\mu q$ can be written as follows:

$$\sigma \times BR(LQ\overline{LQ} \to eq\mu q) = \sigma \times 2\beta_1\beta_2 = N/(\epsilon \times \mathscr{L}),$$

where β_1 is the branch ratio of tau decay into electron, β_2 is the branch ratio of tau decay into muon, N is the number of observed data events after our selection, ϵ is the total selection efficiency as a function of M_{LQ} and $\mathscr{L}$ is the integrated luminosity. The numbers of candidate events in our leptoquark mass-dependent selections are shown in Table 5.5. We observe no excess of events and thus set a 95% C.L. upper limit on the cross section as a function of M_{LQ} defined as:

$$\sigma^{lim} = \frac{N^{lim}}{\epsilon_{tot} \times \mathscr{L}}.$$

In Table 5.7 we report the $\beta = 1$ values of the cross section limits in $eq\mu q$ for each M_{LQ} and the theoretical calculations at NLO for pair production of scalar leptoquarks at the Tevatron using the CTEQ6.1 PDF with different choices of scale. In Figure 5.7 the limit cross section as a function of M_{LQ} is compared with the theoretical expectations for $LQ\overline{LQ} \to eq\mu q$. At the intersection point between experimental and theoretical curves we find the lower limit on M_{LQ} at 115 GeV/c^2.

Mass (GeV/c^2)	95% CL σ (pb)	σ Theory CTEQ6.1 (pb)	
		$Q^2 = M_{LQ}^2/2$	$Q^2 = 2M_{LQ}^2$
80	0.524E+02	0.601E+02	0.441E+02
100	0.158E+02	0.179E+02	0.134E+02
120	0.573E+01	0.640E+01	0.494E+01
140	0.238E+01	0.263E+01	0.207E+01
160	0.108E+01	0.119E+01	0.947E+00
180	0.525E+00	0.557E+00	0.460E+00
200	0.268E+00	0.293E+00	0.235E+00
220	0.141E+00	0.154E+00	0.124E+00
240	0.762E-01	0.832E-01	0.664E-01
260	0.419E-01	0.457E-01	0.364E-01

Table 5.7: Values of the upper limits at 95% CL of the production cross section of third generation leptoquarks decaying into $eq\mu q$ channel as a function of M_{LQ}. The last 2 columns on the right report the result of the theoretical calculations at Next-To-Leading order with CTEQ6.1 for different choices of the scale.

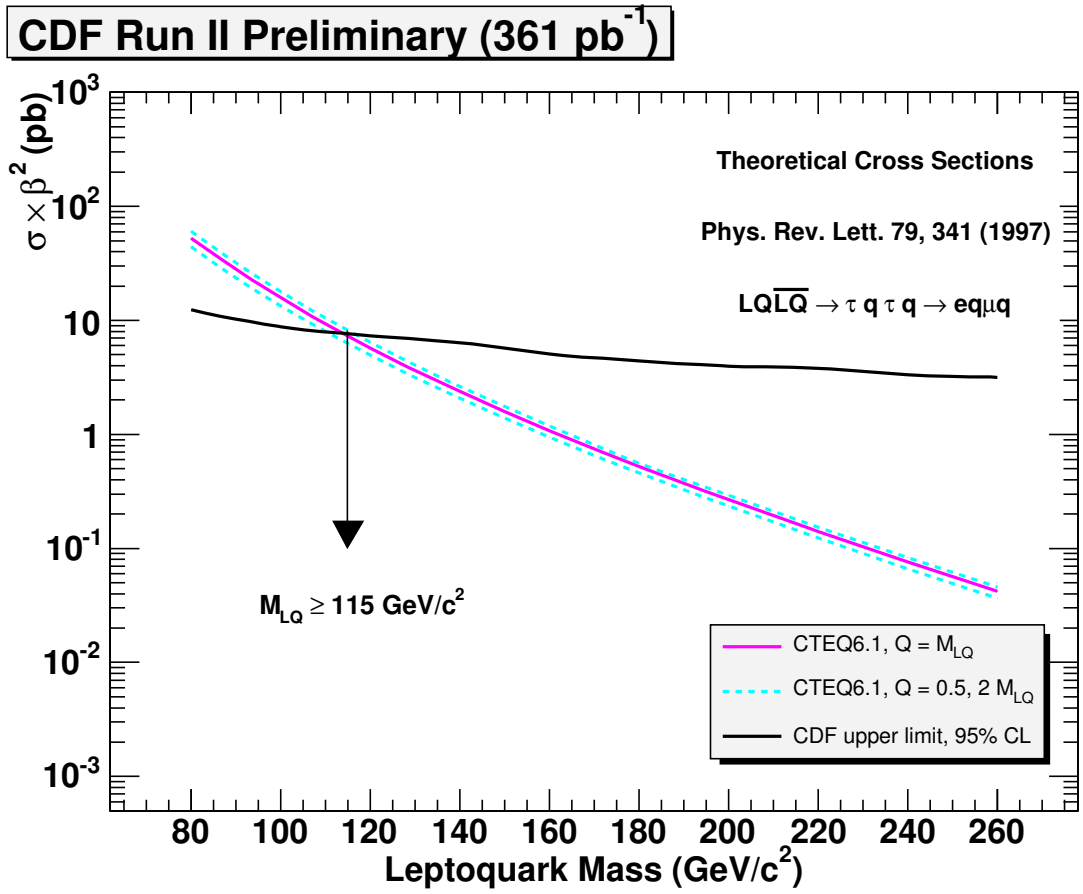

Figure 5.7: Limit cross section as a function of M_{LQ} compared with the theoretical expectations calculated at NLO accuracy. At the intersection points between experimental and theoretical curves we find a lower limit on M_{LQ} at 115 GeV/c^2 in $eq\mu q$ channel.

Appendix A

Lagrangian approach for the theory of Gauge Fields

We will take Lagrangian approach to describe gauge field theory. The advantage in this approach is, it is a familiar construct in classical mechanics, and many of its practical application can be understood already at the classical level. Lagrangian field theory is also particularly suited to the systematic discussion of invariance principles and the conservation laws to which they are related. In addition, a variational principle provides a direct link between the Lagragian and the equations of motion. This is what exactly employed by the Standard Model to account for the phenomenology of the particles and their interactions described in the last section.

The motivation for using the theory of gauge fields to describe particle interactions lies in its ability to connect conserved quantities with symmetries. Noether's Theorem (See [74]) proved that, for each type of continuous transformation that leaves a given physical system's equations of motion unchanged, or in other words, if the system is *invariant* under such transformation, then there must exist a conserved quantity. For example:

- The invariance of physical systems with respect to spatial translation (in other words, that the laws of physics do not vary with locations in space) gives the law of conservation of linear momentum;
- Invariance with respect to rotation gives law of conservation of angular momentum;
- Invariance with respect to time translation gives the well known law of conservation of energy.

In quantum field theory, the analog to Noether's theorem, the Ward-Takahashi identities, yields further conservation laws, such as the conservation of electric charge from the invariance with respect to the gauge invariance of the electric potential and vector potential.

Generally speaking, the Lagrangian approach is characterized by a simplicity in that field theory may be regards as the limit of a system with n degrees of freedom as n tends toward infinity. In gauge field theory particles are described as quantized fields appearing in the Lagrangian density, $\mathscr{L}$. Any continuous field transformation which leaves unchanged the action of the Lagrangian, $\mathcal{S} \equiv \int d^4x \mathscr{L}(\psi, \partial\psi)$, corresponds to a conserved quantity.

Construction of a field theory begins from the Lagragian density $\mathscr{L}(\psi(x), \partial_\mu\psi(x))$, a function of the field $\psi(x)$ and its four-gradient $\partial_\mu\psi(x) = \partial\psi(x)/\partial x^\mu$. The field itself, $\psi(x)$ can be treated as a seperate generalized coordinate at each value of its argument, the space-time coordinate x.

Similar to classic mechanics, we define a least action as

$$S \equiv \int_{t1}^{t2} dt \int d^3x \mathscr{L}(\psi, \partial_\mu\psi) \tag{A.1}$$

The action is required to be stationary,

$$\delta S = \delta \int_{t1}^{t2} d^4x \mathscr{L}(\psi, \partial_\mu\psi) = 0 \tag{A.2}$$

subject as always to the constraint that the variations in the fields vanish at the endpoints $t1$ and $t2$.

By applying Euler-Lagrange equation in the form

$$\frac{\partial L}{\partial q} = \frac{d}{dt}(\frac{\partial L}{\partial \dot{q}}) \tag{A.3}$$

Switching coordinate $q(t)$ by the generalized coordinate $\psi(x)$, the requirement of least action is now ensured for the Lagrangian density as follows:

$$\frac{\partial \mathscr{L}}{\partial \psi(x)} = \partial_\mu \frac{\partial \mathscr{L}}{\partial(\partial_\mu\psi(x))} \tag{A.4}$$

The equation (A.4) will lead in turn to explicit equations of motion for the fields. Just like the case in classic mechanics that you can eventually recover Newton's equation of motion $F \equiv -dV/dx = m\ddot{x}$ from one-dimension Lagrangian $L = \frac{1}{2}m\dot{x}^2 - V(x)$. Moreover, the equations of motion are unchanged if a total divergence is added to the Lagrangian density. And for problems involving with several fields ψ_i, the variational principle applied separately to each field leads to a set of equations (A.4), just as for mechanical problems with several generalized coordinates. This is another big convenience by taking Lagragian approach in the description of gauge field theory for Standard Model.

For our purpose of constructing gauge theories from physical symmetries, it will often be the Lagrangian that comes first and the equations of motion that appear as consequence. However when we proceed in this manner, the construction of the Lagrangian is tricky. Because other than a impractical toy, your Lagrangian better can reproduce certain characteristics of simpler equations of motion. Therefore it is natural to take a look at those most commonly occuring Lagrangians at beginning.

Let's start from Dirac Lagrangian for a free particle having mass m:

$$\mathscr{L}_{Dirac} = i\,\bar{\psi}\,\gamma^{\mu}\,\partial_{\mu}\psi - m\,\bar{\psi}\,\psi \tag{A.5}$$

Equation (A.5) is manifestly globally invariant under phase transformations. In group theory phase transitions are described by the $U(1)$ gauge group transformations which are the set of all one-dimensional unitary matrices: $U(\theta) = e^{iq\theta}$. For the transformation $\psi \rightarrow e^{iq\theta}\psi$, the Lagrangian (A.5) remains unchanged, and the charge, q, is a conserved quantity. However, this is not the case when requiring (A.5) to be invariant under a *local* $U(1)$ gauge transformation which, unlike a global gauge transformation, is space-time dependent: $\psi \rightarrow e^{iq\theta(x)}\psi$.

Equation (A.5) can be made locally gauge invariant by introducing an extra term in the Lagrangian which will cancel the factor resulting from the derivative of the space-time dependent $\theta(x)$. This extra term is folded into the derivative to make a "covariant derivative":

$$\mathcal{D}_{\mu} \equiv \partial_{\mu} + iqA_{\mu}. \tag{A.6}$$

where A_{μ} is a vector gauge field and as a rule transforms under gauge transformations as $A_{\mu} \rightarrow A_{\mu} - \partial_{\mu}\theta$. The gauge field A_{μ} can be fixed in this way since the derivatives of fields will not affect the Euler-Lagrangian equations. The result of using this covariant derivative in (A.5) is

$$\mathscr{L}' \;=\; i\psi\,\gamma^{\mu}\,\partial_{\mu}\psi - q\psi\,\gamma^{\mu}\,\psi\,A_{\mu} - m\,\bar{\psi}\,\psi. \tag{A.7}$$

Equation (A.5) is promoted to a locally invariant Lagrangian by replacing the derivative with a covariant one. However, since the covariant derivative introduces a new vector gauge field, A_{μ}, the full Lagrangian must have a corresponding free Lagrangian term for this field. Since A_{μ} is a vector field, it can be described by the Lagrangian for a vector field (see [71]), i.e.

$$\mathscr{L}_{Free} = -\frac{1}{4}F_{\mu\nu}F^{\mu\nu} + \frac{1}{2}m_A^2 A^{\mu}A_{\mu}. \tag{A.8}$$

By checking the second term in (A.8), it would stand for a photon mass term

$$\mathscr{L}_\gamma = \frac{1}{2} m_A^2 A^\mu A_\mu \tag{A.9}$$

which is not locally gauge invariant because

$$A^\mu A_\mu \to (A^\mu - \partial^\mu \theta)(A_\mu - \partial_\mu \theta) \neq A^\mu A_\mu \tag{A.10}$$

Therefore it is necessary to require that the mass of the vector gauge field be zero, i.e. $m_A = 0$. Thus we find that local gauge invariance has led us to the existence of a massless photon. The change to a covariant derivative and the addition of a free term for the resulting vector field results in a new Lagrangian:

$$\mathscr{L}_{QED} = \bar{\psi}(i\,\gamma^\mu \partial_\mu - m)\psi - \frac{1}{4} F_{\mu\nu} F^{\mu\nu} - q\bar{\psi}\,\gamma^\mu\,\psi\,A_\mu \tag{A.11}$$

Equation (A.11) is well known as the Lagrangian for an electromagnetic field, where A_μ is the electromagnetic potential, and q is the electric charge which couples the electromagnetic field (photons) to the spinor fields (electrons and positrons) by a factor of q.

By requiring that the Dirac Lagrangian for a free spinor field be locally invariant under phase transformations, the Lagrangian for spinor fields interacting with the electromagnetic potential is obtained. The last two terms in (A.11) appear in the Maxwell Lagrangian, where the charge density is given by $J^\mu = q(\bar{\psi}\,\gamma^\mu \psi)$. Though it is sufficient to only require global phase invariance to explain conservation of charge, it takes local phase invariance of (A.5) to reproduce the Maxwell Lagrangian (last 2 terms of (A.11)) for charged currents.

A side-note: For $SU(2)_L \times U(1)_Y$, the electroweak Lagrangian density must include the interaction terms as:

$$\mathscr{L}_{ewk} = \bar{\psi}_L \gamma^\mu (i\,\partial_\mu - g\mathbf{T}\cdot\mathbf{W}_\mu - g'\frac{Y}{2}\,B_\mu)\psi_L + \bar{\psi}_R \gamma^\mu (i\,\partial_\mu - g'\frac{Y}{2}\,B_\mu)\psi_R - \frac{1}{4}\mathbf{W}_{\mu\nu}\cdot\mathbf{W}^{\mu\nu} - \frac{1}{4}B_{\mu\nu}B^{\mu\nu} \tag{A.12}$$

For $SU(3)_C$, the Lagrangian densiy takes the form:

$$\mathscr{L}_{QCD} = \bar{q}_j(i\,\gamma^\mu \partial_\mu - m)q_j - \frac{1}{4} G^a_{\mu\nu} G^{\mu\nu}_a - g_s(\bar{q}_j\,\gamma^\mu\,T_a\,q_j)G^a_\mu \tag{A.13}$$

Similarly, the interaction terms in SU(5) Lagrangian may be written:

$$\begin{aligned}
\mathscr{L}_{int} = & -\frac{g_5}{2} G^a_\mu (\bar{u}\,\gamma^\mu\,\lambda^a\,u + \bar{d}\,\gamma^\mu\,\lambda^a\,d) \\
& -\frac{g_5}{2} W^i_\mu (\bar{L}_u\,\gamma^\mu\,\tau^i\,L_u + \bar{L}_e\,\gamma^\mu\,\tau^i\,L_e) \\
& -\frac{g_5}{2}\frac{3}{5}\mathscr{A}_\mu \sum_{\substack{fermion \\ species}} \bar{f}\,\gamma^\mu Y f \\
& -\frac{g_5}{\sqrt{2}}[X^-_{\mu;\alpha}(\bar{d}^\alpha_R\,\gamma^\mu\,e^c_R + \bar{d}^\alpha_L\,\gamma^\mu\,e^c_L + \epsilon_{\alpha\beta\gamma}\bar{u}^{c\gamma}_L\,\gamma^\mu\,u^\beta_L) + h.c.] \\
& +\frac{g_5}{\sqrt{2}}[Y^-_{\mu;\alpha}(\bar{d}^\alpha_R\,\gamma^\mu\,\nu^c_R + \bar{u}^\alpha_L\,\gamma^\mu\,e^c_L + \epsilon_{\alpha\beta\gamma}\bar{u}^{c\beta}_L\,\gamma^\mu\,d^\gamma_L) + h.c.]
\end{aligned}$$

where SU(2) doublets are:

$$L_u = \begin{pmatrix} u \\ d_\theta \end{pmatrix}_L,\ L_e = \begin{pmatrix} \nu_e \\ e \end{pmatrix}_L. \tag{A.14}$$

Appendix B

Other models that predict signatures similar to Leptoquarks

- **Dynamic Symmetry Breaking and Composite Models**
  In dynamic symmetry breaking models (known as Technicolor Models), the Higgs mechanism of the electroweak symmetry breaking is replaced by a dynamical symmetry breaking [118] from a confining strong force at an energy scale $\Lambda \sim G_F^{-1/2}$ [63]. The need for a Higgs Model scalar vacuum expectation value is obviated by a strong-coupling, confining, non-abelian gauge theory:

  $$G_{TC} \times SU(3)_c \times SU(2)_L \times U(1).$$

  The symmetry breaking of the technicolour group results in Goldstone bosons which may have leptoquark properties. The estimate for their mass is $\sim \mathcal{O}(200\mathrm{GeV/c^2})$ for $\Lambda_{TC} \sim 1\mathrm{TeV/c^2}$[108].

  The concept of endowing masses to the fermions and gauge bosons via a dynamical symmetry breaking has led to the formulation of a number of composite theories [25, 63, 109, 37] which theorize a low-energy, strong-confining $SU(2)_L$ gauge. In composite models fermions and gauge bosons are composite states of a set of fundamental fields which interact through a confining strong force. The behavior of weak interactions at currently accessible energy levels are thus analogous to the interactions of strongly bound meson states. The exact gauge group structure is model dependent. In the simplest model by Abbott and Farhi (AF) the gauge Lagrangian is formally identical to the standard electroweak model [25]. All left-handed fermions are $SU(2)_L$ singlets of this strong electroweak gauge force, while right-handed particles are still point-like. Left-handed fermions are bound states of the left-handed fundamental fields

called "preons". Leptoquarks appear in the AF model as bound states of preons [81]. Other strong confining gauge groups are also possible. For example there is a double confining $SU(2)_L \times SU(2)_R$ technicolour gauge theory [37, 38] which has only fundamental fermions and different confinement scales. In strong confining gauge theories leptoquarks appear as Goldstone bosons and can be naturally light, having a mass from a few 100 GeV/c^2 to a few TeV/c^2[108].

- **Supersymmetry Models**

  A very well motivated candidate for new physics beyond the Standard Model is *Supersymmetry* (SUSY), which is needed to connect the Standard Model with an ultimate perturbative unification of the fundamental interactions. Supersymmetry refers to a fermion-boson symmetry for which each fermion(boson) shares the same coupling with a boson(fermion) partner. This symmetry, denoted as R-symmetry in the SUSY models. In the context of high energy colliders, the consequences of R-parity conservation are significant. The R-parity of a particle is given by the spin j, baryon number B and lepton number L:

  $$R = (-1)^{3B+L+2j},$$

  hence giving ordinary particles $R = +1$ and super-symmetric particles $R = -1$. If R-parity is conserved, then at today's particle colliders, SUSY-particles would be produced in pairs and there would be a lightest-state stable SUSY-particle unable to decay to non-super-symmetric particles. If R-parity is not conserved, then SUSY-particles are allowed to decay completely into non-supersymmetric particles. Such a decay would imply that supersymmetry-particles could have leptoquark-like properties as would be the case for a scalar-quark, $\tilde{q}$ decaying to a lepton-quark pair, e.g. $\tilde{q} \to \ell q$.

Appendix C

The Higgs Mechanism

The Higgs mechanism is also employed in another sector of the Standard Model Lagrangian. The method of requiring local $SU(2)$ gauge invariance for the final Standard Model Lagrangian is problematic for spin-1/2 particles. The left and right-handed helicity states of the fermions transform differently under rotations of the $SU(2)$ type, which makes it impossible to construct a Lagrangian which is locally $SU(2) \times U(1)$ invariant. The local gauge invariance of the Lagrangian could be restored by replacement of the partial derivatives with covariant ones having a particular helicity, i.e.:

$$\begin{aligned} D_\mu \psi_R &= (\partial_\mu + ig' B_\mu)\psi_R \\ D_\mu \psi_L &= (\partial_\mu + \frac{i}{2} g' B_\mu - \frac{i}{2} g \sigma_i W^i_\mu)\psi_L. \end{aligned} \tag{C.1}$$

However the mass term is a scalar operator which mixes the left/right-helicity states. This spoils the $SU(2)$ invariance of the Lagrangian unless the mass terms vanish. The Standard Model treats this problem by endowing masses to the fermions using the same method that was used to endow masses to the gauge bosons. The fermion interactions can be given by [29]:

$$\begin{aligned} i\gamma^\mu D_\mu \psi_R - \lambda_f \phi^\dagger \psi_L &= 0 \\ i\gamma^\mu D_\mu \psi_L - \lambda_f \phi^\dagger \psi_R &= 0. \end{aligned} \tag{C.2}$$

Once the field shifts such that $\langle \phi \rangle_0 \neq 0$, the fermion will absorb the resulting Goldstone boson and acquire mass.

Though this method will keep the Lagrangian locally $SU(2)$ invariant, it comes at the price of inelegance. There is nothing to fix the coupling constants, λ_f, in (C.2). Therefore, for each different massive fermion there must correspond a different coupling constant, i.e. λ_{f_e} for elections, $\lambda_{f_{\nu_e}}$ for electron-neutrinos, etc. Each must be tuned to achieve the exper-

imentally measured fermion mass. This is a good indication that the Standard Model is an incomplete theory. In all, the Higgs mechanism endows masses for 15 discovered particles in the Standard Model. However, a physical Higgs particle has yet to be experimentally detected.

The Higgs Mechanism is the means by which the particles appearing in the Standard Model Lagrangian acquire a mass and is one if its distinctive features. The Higgs mechanism is achieved by the spontaneous symmetry breaking of the vacuum expectation value. The discrete case of symmetry breaking can be seen in the example of a scalar field with a ϕ^4 interaction:

$$\mathcal{L} = \frac{1}{2}\partial_\mu \phi\, \partial^\mu \phi - V(\phi), \quad \text{where} \tag{C.3}$$

$$V(\phi) = \frac{1}{2}\mu^2\phi^2 - \frac{1}{4!}\lambda\phi^4, \tag{C.4}$$

and λ is a dimensionless constant representing the coupling of the 4-boson vertex. The Lagrangian is symmetric in $\phi = -\phi$, and the potential has 3 possible minimums. If $\mu^2 > 0$, then the local minimum is $\phi_{min} = 0$. However, if $\mu^2 < 0$, then $\phi_{min} = \pm\sqrt{-\frac{\lambda}{6}\mu^2} = \pm\nu$. Since we are concerned with evaluating small perturbations about the energy minimum, we prefer to expand about one of these new minimum, $\phi = \pm\nu$. Normally, we require the vacuum expectation of the scalar field to be zero. However, we have instead, $\langle\phi\rangle_0 = \nu$. This is easily corrected by shifting the value of the scalar field by ν. The new scalar field is given by, $\tilde{\phi} = \nu + h(x)$, where $h(x)$ is the value of the scalar field over and above the constant, uniform value ν. This shifted scalar field gives $\langle\tilde{\phi}\rangle_0 = 0$. Substituting this into our Lagrangian (C.4) gives:

$$\mathcal{L} = \frac{1}{2}(\partial_\mu h)^2 + \frac{1}{2}V^{(2)}(\nu)\, h^2 + \frac{1}{3!}V^{(3)}(\nu)\, h^3 + \frac{1}{4!}V^{(4)}(\nu)\, h^4 ... \tag{C.5}$$

where $V^{(2)}(\nu) = \mu^2 - \frac{1}{2}\lambda\nu^2 = -2\mu^2$, $V^{(3)}(\nu) = -\lambda\nu$, and $V^{(4)}(\nu) = -\lambda$. So finally we get:

$$\mathcal{L} = \frac{1}{2}(\partial_\mu h)^2 - \frac{1}{2}(2\mu^2)h^2 - \frac{1}{3!}\lambda\,\nu\, h^3 - \frac{1}{4!}\lambda\, h^4. \tag{C.6}$$

The last 2 terms of (C.6) are the same for either value of ν. The first 2 terms are the Lagrangian for a free particle with a mass given by $m_h^2 = 2\mu^2$. Since $\mu^2 < 0$, then $m_h = \sqrt{-2\mu^2}$ and the mass is positive. Notice that the symmetry $\phi = -\phi$ has been broken once the field shifts to either $\pm\nu$ (see for example [83] [101]).

The continuous case of symmetry breaking can be seen in the example of an $O(2)$ scalar

field theory with a ϕ^4 interaction:

$$\mathscr{L} = \frac{1}{2}\partial_\mu \phi^\dagger \partial^\mu \phi - \frac{\lambda}{4!}(\phi^\dagger \phi - \nu^2)^2, \tag{C.7}$$

and the scalar field now has two components:

$$\phi = \begin{pmatrix} \phi_1 \\ \phi_2 \end{pmatrix}. \tag{C.8}$$

Equation C.7 has a circle of degenerate minima at $|\phi_{min}| = \nu$. In order to expand about a particular ground state, we prefer to expand about this minimum. This minimum is degenerate, so we are free to choose:

$$\langle\phi\rangle_0 = \begin{pmatrix} 0 \\ \nu \end{pmatrix}. \tag{C.9}$$

Normally, one requires the vacuum expectation value of a scalar field to be zero. This is easily corrected by shifting the value of the scalar field by ν:

$$\tilde{\phi} = e^{i\theta(x)} \begin{pmatrix} 0 \\ \nu + h(x) \end{pmatrix}. \tag{C.10}$$

This new vacuum state is now invariant only under the group which leaves the shifted field invariant. In general, when a field is shifted, the symmetry is broken from O(N) down to O(N-1). In the current case, there are only 2 components to ϕ, so we have broken the symmetry group O(2) to O(1).

Substituting the new field (C.10) into our Lagrangian results in :

$$\mathscr{L} = (\partial h)^2 + \nu^2(\partial\theta)^2 + 2\nu h(\partial\theta)^2 + h^2(\partial\theta)^2 - \frac{\lambda}{6}\nu^2 h^2 - \frac{\lambda}{6}\nu h^3 - \frac{\lambda}{4!}h^4. \tag{C.11}$$

By making the substitutions $h = 1/\sqrt{2}\ \phi_A$, $\nu\theta = 1/\sqrt{2}\ \phi_B$, and $m = \sqrt{\lambda/6}\ \nu$, Equation (C.11) becomes:

$$\mathscr{L} = \frac{1}{2}(\partial_\mu\phi_A\partial^\mu\phi_A) - \frac{1}{2}m^2\phi_A^2 + \frac{1}{2}(\partial_\mu\phi_B\partial^\mu\phi_B) + \mathscr{L}_{int}, \tag{C.12}$$

where $\mathscr{L}_{int}$ are the 3 and 4 point interactions between the fields ϕ_A and ϕ_B. The first two terms in (C.12) comprise the Lagrangian for a massive scalar field ϕ_A, and the second term a free Lagrangian for the field ϕ_B which apparently has no mass. In addition to the breaking of symmetry of Equation (C.7) by choosing a particular vacuum state, one of the fields automatically becomes massless. Such a massless scalar field is known as a "Goldstone

Boson". It can be shown vigorously that for each broken generator of a symmetry group, there will correspond a creation of a massless scalar particle. Breaking the symmetry of a theory from $O(N)$ to $O(N-1)$ will result in $N-1$ Goldstone Bosons. For the case at hand, we broke the O(2) symmetry of (C.7) which resulted in a Lagrangian which is still symmetric under global O(1) but now has a massless scalar boson.

Returning to (C.7), we see that the Lagrangian is globally phase invariant. As discussed, this symmetry is not broken under the spontaneous symmetry breaking. Equation (C.7) can be made locally phase invariant by replacing the derivatives with a covariant one (A.6), and giving the new gauge field a free term, i.e. $\partial_\mu \to \mathcal{D}_\mu = \partial_\mu + ieA_\mu$, where $A_\mu \to A_\mu - \frac{1}{e}\partial_\mu \alpha(x)$ under $\phi \to e^{i\,\alpha(x)}\phi$. Equation (C.7) will then become,

$$\mathscr{L} = \frac{1}{2}\mathcal{D}_\mu \phi^\dagger \mathcal{D}^\mu \phi + \frac{\lambda}{4!}(\phi^\dagger\,\phi - \nu^2)^2 - \frac{1}{4}F^{\mu\nu}F_{\mu\nu}, \tag{C.13}$$

which is locally $U(1)$ gauge invariant. Now we break the symmetry by shifting the field: $\phi \to \phi = \nu + h(x)$. Inserting into (C.13) by parts (and dropping the dependence on x), we find,

$$\begin{aligned} \mathcal{D}_\mu &= \partial_\mu h - ie(\nu h)A_\mu \\ \mathcal{D}_\mu \phi^\dagger \mathcal{D}^\mu \phi &= (\partial_\mu h)^2 + e^2(\nu + h)^2 A_\mu A^\mu \\ \frac{\lambda}{4!}(\phi^\dagger \phi - \nu^2)^2 &= \frac{\lambda}{4!}(2\nu + h)^2 h^2 \end{aligned}$$

Putting all the pieces together, (C.13) becomes:

$$\begin{aligned} \mathscr{L} &= (\partial_\mu h)^2 + e^2(\nu+h)^2 A_\mu A^\mu - \frac{1}{4}F_{\mu\nu}F^{\mu\nu} - \frac{\lambda}{4!}(2\nu+h)^2 h^2 \\ &= (\partial_\mu h)^2 - \frac{\lambda}{6}\nu^2 h^2 - \frac{1}{4}F_{\mu\nu}F^{\mu\nu} + e^2\nu^2 A_\mu A^\mu + \mathscr{L}_{int}. \end{aligned} \tag{C.14}$$

Again, we make the substitutions $h = 1/\sqrt{2}\ \phi_A$, $\nu\theta = 1/\sqrt{2}\ \phi_B$, and $m = \sqrt{\lambda/12}\ \nu$. The result is,

$$\mathscr{L} = \frac{1}{2}(\partial_\mu \phi_A \partial^\mu \phi_A) - m^2\phi_A + \frac{1}{4}F_{\mu\nu}F^{\mu\nu} + e^2 m^2 \frac{12}{\lambda}A_\mu A^\mu + \mathscr{L}_{int}. \tag{C.15}$$

By requiring local phase invariance and invoking continuous spontaneous symmetry breaking of (C.12), we have recovered a massive scalar particle ϕ_A and a massive gauge field A^μ with mass $m_B = \sqrt{12e^2m^2/\lambda}$. In essence, by an astute choice of gauge, we have eliminated the massless Goldstone boson in (C.12) and recovered a massive vector field. Metaphorically, the gauge field "ate" up Goldstone boson and acquired a mass. This phenomenon is also explained through degrees of freedom (see for example [71]). A massless vector field, A_μ

has 2 degrees of freedom, one for each polarization state. When it acquires mass, it has 3 degrees of freedom: 2 transverse states, and 1 longitudinal state. By fixing the gauge of the scalar field ϕ a degree of freedom is freed. It is precisely the local gauge invariance of the scalar field ϕ which afforded the vector field this third degree of freedom. This process is known as the "Higgs Mechanism."

Appendix D

Electron and Muon ID Efficiencies

D.1 Electrons

First for electron ID, we select the following sample to study the ID cut efficiencies in the central region:

- One leg with all "tight" central cuts
- Second leg with "probe" central cuts

Then we refer to the number of events in this sample as N_CC. Then one by one we apply the "tight" central ID cuts on the second leg, and measure the efficiencies of these cuts. For the individual efficiencies, we use:

$$\epsilon_c^i = \frac{N_{Ti} + N_{TT}}{N_{CC} + N_{TT}} \tag{D.1}$$

where N_{TT} is the number of events that both legs pass the tight central cuts and N_{Ti} is the number of events that one leg passes the tight cute and the other passes the ith electron ID cut.

For the total efficiency, when both leg pass the tight cuts, the equation above becomes:

$$\epsilon_c = \frac{2N_{TT}}{N_{CC} + N_{TT}} \tag{D.2}$$

D.2 Muons

In this section, we verify the validity of using the beam-constrained COT muon ID and isolation efficiencies by following the 1-leg based or "tight-loose" method described in [21].

The method looks for dimuon events with $80 < M_{\mu\mu}/\mathrm{GeV/c^2} < 100$ containing same type (CMUP-CMUP, CMX-CMX) and mixed type (CMUP-CMX, CMUP-TRK, CMX-TRK)

events. For this study only the 179 pb^{-1} of CMX included events is used. The efficiency is determined by starting with a base sample of events, R_{tot}, to which the ID or isolation cuts are not applied. In these events a tight muon (1st leg) is selected based on the i number of ID or isolation cuts. A loose muon (2nd leg) is then searched for by applying the i cuts and seeing whether it passes or fails. To determine the event yield per cut R_i, the set of events are selected by requiring that all cuts other than the i'th cut are passed, i.e.

$$R_i = \epsilon - i \cdot (2 - \epsilon_i) \cdot \prod_j \epsilon_j^2 \cdot R_{tot}, \quad (j \neq i) \tag{D.3}$$

in which R_i contains all possible combinations of tight (T) and loose (L) muons. To determined the total event yield, R_0, we require that all cuts are applied and all cuts are passed by both muons:

$$R_0 = \prod_i \epsilon_i^2 \cdot R_{tot} \tag{D.4}$$

Using Equations D.3 D.4, one can solve for the individual efficiencies, ϵ_i. They are related to the ratio of the event yield per cut and the total event yield by:

$$\epsilon_i = \frac{2 \times R}{1 + R}, \tag{D.5}$$

where $R \equiv R_0/R_i$. The errors on the efficiencies are calculated via their moments:

$$\sigma_\epsilon^2 = \left(\frac{\delta\epsilon}{\delta R}\right)^2 \cdot \sigma_R^2 \tag{D.6}$$

Solving for (D.6) we find:

$$\sigma_\epsilon = \frac{\epsilon \cdot R}{(1 + R)} \sqrt{\frac{(1 - R)}{R_0}}. \tag{D.7}$$

For the mixed muon-type events (CMUP-CMX, CMUP-TRK, CMX-TRK), the event yields are slightly different to account for a T or L second leg of different type than the first T leg:

$$R_0 = \prod_i \epsilon_i \cdot R_{tot} \tag{D.8}$$

$$R_i = (\epsilon_i + (1 - \epsilon_i)) \cdot \prod_j \epsilon_j \cdot R_{tot}, \quad (j \neq i). \tag{D.9}$$

In this case the ratio $R = R_0/R_i = \epsilon$(1st Leg) and the efficiencies can be calculated right away. The errors are determined from the binomial error on R. Table D.1 lists the effi-

ciencies for each cut for both same and mixed-type dimuon events. The muon isolation and ID efficiencies are calculated separately. A total efficiency for muon ID and isolation is determined by combining the same and mixed-type efficiencies in quadrature, i.e. they are treated as separate measurements.

The results shown in Table D.1 are in close agreement with [88, 89]. The COT hit requirements were enforced in this analysis in consideration of the TRK muons, and were folded into its ID efficiency.

SAME TYPE	CMUP	CMX	TRK
16(ST), 20(AX)	1.000 ± 0.000	1.000 ± 0.000	
$E_{HAD} < 6$ GeV	0.984 ± 0.003	0.984 ± 0.005	
$E_{EM} < 2$ GeV	0.963 ± 0.005	0.977 ± 0.005	
dx(CMU) < 3 cm	0.950 ± 0.005	-	
dx(CMP) < 5 cm	0.979 ± 0.004	-	
dx(CMX) < 6 cm	-	0.971 ± 0.007	
ID eff	0.882 ± 0.007	0.933 ± 0.010	
ISO eff	0.988 ± 0.003	0.979 ± 0.006	
MIXED TYPE			
16(ST), 20(AX)	1.000 ± 0.001	1.000 ± 0.001	0.988 ± 0.000
$E_{HAD} < 6$ GeV	0.987 ± 0.001	0.979 ± 0.002	0.981 ± 0.000
$E_{EM} < 2$ GeV	0.966 ± 0.001	0.979 ± 0.002	0.970 ± 0.000
dx(CMU) < 3 cm	0.963 ± 0.001	-	
dx(CMP) < 5 cm	0.976 ± 0.001	-	
dx(CMX) < 6 cm	-	0.971 ± 0.001	
ID eff	0.895 ± 0.001	0.930 ± 0.001	0.940 ± 0.000
ISO eff	0.976 ± 0.000	0.976 ± 0.006	0.978 ± 0.000
combined ID eff	0.888 ± 0.007	0.932 ± 0.010	0.940 ± 0.000
combined Iso eff	0.982 ± 0.003	0.977 ± 0.006	0.957 ± 0.000

Table D.1: Efficiencies obtained from the 1-leg method using 179 pb^{-1} of data. The EM and HAD slide with the muon P_T as described in Table 3.5.

D.3 ID and Isolation Dependence

In this section, we check the muon ID efficiency as a function of isolation fraction. The events have been chosen in the same way as the efficiency study described in Section D. The muon ID distribution is shown in Figure D.1. Since we apply the muon ID efficiency factor to

the leptoquark acceptance, we wish to check whether this convolution has a significant effect in the Monte Carlo samples. In the discrete case, this is done by weighting the muon ID efficiency relative to the number of muons passing the isolation cuts with a specific fractional isolation, i.e.:

$$< \epsilon_{iso} > \quad = \quad \sum_{j}^{M(LQ)} \sum_{i}^{no.bins} \frac{\epsilon_{iso}(i) \times N(i)}{N_{TOT}}. \tag{D.10}$$

For this study, we chose a binning of $i = 5$ and the deconvoluted efficiency was averaged over the $j = 9$ LQ samples. Figure D.2 shows the normalized isolation distributions for CMUP, CMX and TRK for a LQ mass of 240 GeV/c^2. The deconvoluted muon ID efficiencies along with the scale factor are listed in Table D.2.

Muon Type	$<\epsilon_{ID}^{deconv.}>$	ϵ_{ID}^{DATA}	Scale Factor
CMUP	0.880	0.889 ± 0.006	0.9898
CMX	0.935	0.952 ± 0.005	0.9821
TRK	0.950	0.929 ± 0.000	1.0226

Table D.2: The muon ID efficiencies deconvoluted from the muon isolation.

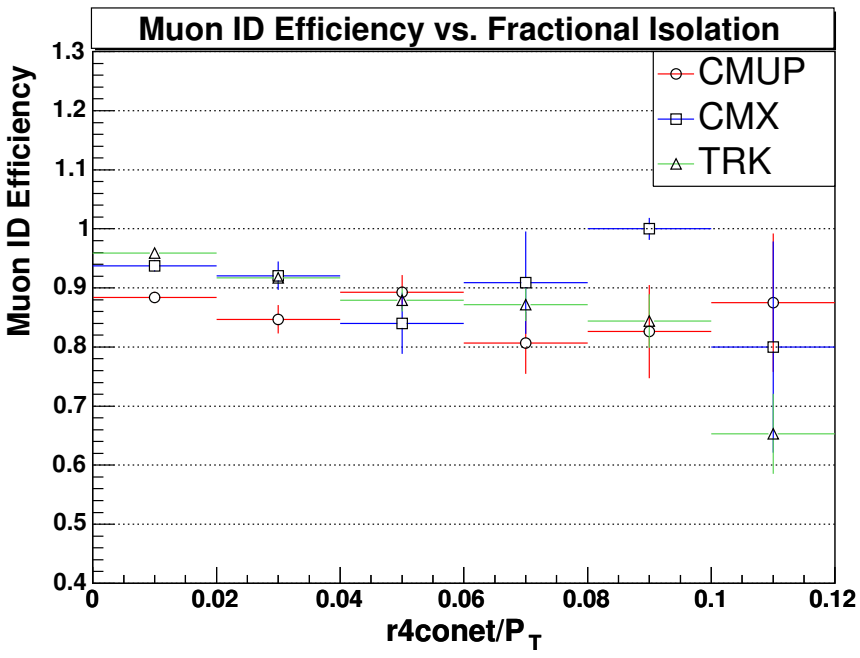

Figure D.1: The muon ID efficiency versus the muon fractional isolation. Each event is required to have at lease one tight muon.

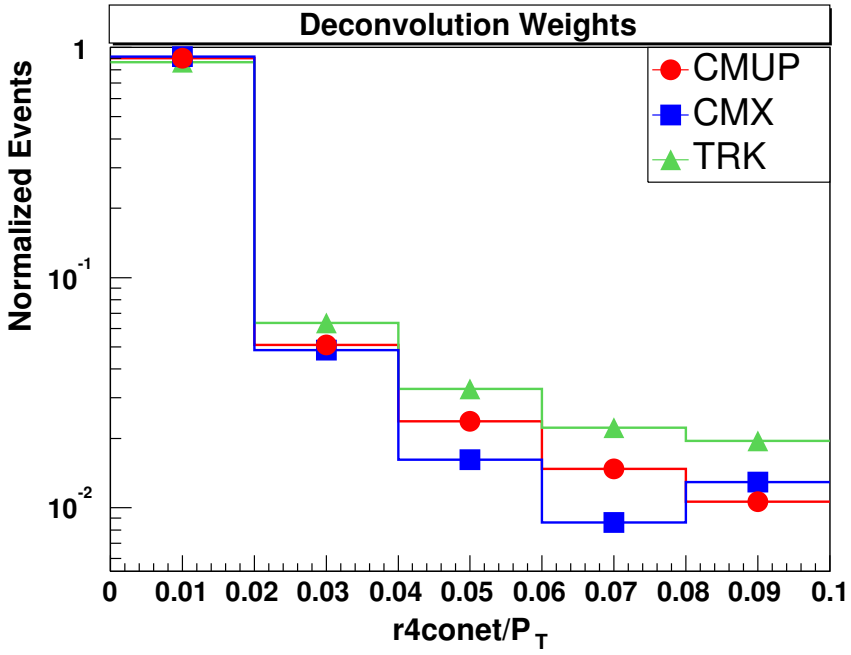

Figure D.2: The M(LQ) = 240 GeV/c^2 normalized isolation distributions for CMUP, CMX and TRK muons.

Appendix E

Preselection Efficiencies

E.1 Muon Trigger Efficiency

The muon trigger efficiency values are taken from [88, 89]. The dimuon candidates were required to pass the Muon ID requirements and the efficiency was calculated by considering two separate dimuon candidates having same and opposite types. The two samples are:

- CMUP-CMX(CMX-CMUP) Dimuon events with a CMX(CMUP) trigger. The efficiency is defined as the fraction of events which also have a CMUP(CMX) trigger:

$$\epsilon(I) = \frac{N(\text{with CMX and CMUP triggers})}{N(\text{with CMX(CMUP) triggers})}$$

- CMUP-CMUP(CMX-CMX) Dimuon events with a CMUP trigger only. The efficiency is defined as:

$$\epsilon(II) = \frac{2 \cdot R}{1+R}, \quad \text{where} \qquad R = \frac{N(\text{with 2 CMUP(CMX) triggers})}{N(\text{with at least 1 CMUP(CMX) trigger})}$$

The final trigger efficiency is calculated by combining the $\epsilon(I)$ and $\epsilon(II)$ efficiencies in quadrature.

In June 2003, the CDF Muon Offline Group proposed a COT exit radius (ρ_{COT}) cut for CMX muon tracks. Due to the trigger design, the trigger acceptance is not the same as the detector acceptance. The XFT trigger requires a muon track to leave hits in at least 4 COT axial superlayers, but a muon track can be reconstructed offline without meeting this requirement. A cut on the COT exit radius, defined by the pseudorapidity and event vertex of the track, selects a detector region where the data and Monte Carlo are in agreement:

$$\rho_{COT} \quad = \quad \frac{sign(\eta) \cdot z_{COT} - z_0}{\tan(\lambda)} > 140cm. \tag{E.1}$$

The COT length, z_{COT}, is 155 cm and $\lambda = \pi/2 - \theta$ where $\theta = 2 \cdot \tan^{-1}(e^{\eta})$. The COT exit radius cut lowers the CMX muon acceptance to obtain the correct trigger efficiency. In this analysis, if a CMX muon passes the ID cuts, but fails the COT exit radius cut, then its status is demoted to a TRK posterior to the muon and event selection cuts. The efficiency of the COT exit radius cut is folded into the definition of the trigger efficiency, and the values taken from [88, 89] are from ρ_{COT} cut efficiencies.

E.2 Lepton Reconstruction Efficiency

The reconstruction efficiencies for CMUP and CMX muons are scaled by the differences in Monte Carlo and data due to discrepancies in the Monte Carlo geometry description. We again use the values reported in [88, 89] for the muon reconstruction efficiency. Cuts are made on the fiduciality of the track inside the CMX and CMUP detectors and are included in the efficiency.

E.3 Z-Vertex Efficiency

The events selected are required to have an event vertex no larger than ± 60 cm along the z-direction from the center of the detector. Events whose vertices are outside this range are likely to have tracks that go undetected by the silicon or even the COT tracking. However, the full luminous $p\bar{p}$ region, which is used by CLC to determine the luminosity, extends outside of this z-range. A study measuring the efficiency of this fiducial cut is reported in [106]. The study reports an efficiency of $\epsilon = 0.951 \pm 0.005$.

E.4 Cosmic Ray Rejection

To remove the cosmic rays contaminating the sample, the di-cosmic bit is used which is based on the use of the COT timing information to deduce if the muons are compatible with an outgoing pair as one would expect in a physics process. The bit is taken from the cosmic bit word stored in the CosmicRayTaggerInfo object [113] and is 100% efficient in removing cosmic rays in dilepton events.

Appendix F

Derive Confidence Level Limits with Bayes Method

To determine the limit on the observed number of leptoquark events using the classical or frequentist approach, one could formulate the limit based on a repeated number of experiments, i.e:

$$P(X^l) = \lim_{N\to\infty} \frac{N_l}{N}, \tag{F.1}$$

where $P(X_l)$ is the probability of measuring X^l, N is the number of repeated identical experiments, and N_l is the limit of the frequency of measuring X^l. The alternative to the frequentist approach is to use Bayesian statistics which allows for an interpretation of the probability as a degree of belief. Heuristically, Bayes' Theorem states that the probability of observing an event belonging to class C_k after observing an event X with feature l is proportional to product of the likelihood of an event X^l belonging to class C_k and the prior probability of there being events of class C_k. The complete theorem is stated by:

$$P(C_k|X^l) \quad = \quad \frac{P(X^l|C_k)P(C_k)}{P(X^l)}, \tag{F.2}$$

The probabilities $P(C_k)$ and $P(X^l)$ are the fraction of events belonging to class C_k and having feature X^l respectively. The probability on the left, $P(C_k|X^l)$, is the posterior probability. It gives the probability that a data point having a feature variable X^l belongs to the class C_k *after* a measurement of X. The probability $P(X^l|C_k)$ is the conditional probability. This function represents the probability that a given data point belonging to a class C_k has feature X^l. This probability can be expressed as a likelihood function. The term $P(C_k)$ allows for the incorporation of knowledge of features of the data prior to

making a determination of the classification of a measurement. Since the probability $P(X^l)$ is independent of the classification of a measurement, it can be seen as a normalization factor. Hence, Equation F.2 can be summarized as:

$$\text{posterior probability} \quad = \quad \frac{\text{likelihood function} \times \text{prior}}{\text{normalization factor}}.$$

The results obtained from the two methods are not always identical (for discussion see [51]). There are several reasons for using a Bayesian versus a frequentist approach to calculate the upper limit on the number of observed leptoquark events. The first is purely aesthetic. In the Bayesian approach a posterior probability is expressed by a likelihood function modified by the result of the experience itself. By using the likelihood, a distinction is implied that given an experimental measurement m, what is considered is the behavior of varying the true value m_t. The frequentist approach makes no such distinction. Instead it implies that no matter what is the true value, m_t, the probability expresses the percentage of time a limit calculated by an infinite ensemble of measurements contains m_t. The second argument is pragmatic: Limits obtained by the Bayesian approach are often more conservative than the frequentist approach. This becomes especially acute in the case where errors are included. In the frequentist approach, introducing errors from the signal acceptance or background calculation actually tightens the limit result. Intuitively this is contrary to the notion that including errors should weaken the limit. Finally, for reasons not exploited in this dissertation, the Bayesian approach allows for a more elegant combination of results.

There are also arguments for not using a Bayesian approach. As pointed out by Cousins in [51], it is not always clear what should be the appropriate choice of a prior distribution when nothing is known about it. A semiclassical approach which avoids this issue is proposed in [70], however it does not incorporate the errors from both the signal acceptance and background calculation.

In this analysis we follow a Bayesian approach which incorporates errors from the signal acceptance and background calculation [14]. We calculate the posterior probability distribution for observing n_0 events with μ_S expected signal events and μ_B expected background events as,

$$P(\mu_S|n_0,\mu_B) \quad = \quad \frac{\mathscr{L}(n_0|\mu_S+\mu_B)P(\mu_S)}{\int_0^\infty \mathscr{L}(n_0|\mu_S+\mu_B)P(\mu_S)d\mu_S}, \tag{F.3}$$

where $\mathscr{L}(n_0|\mu_S+\mu_B)$ is the likelihood distribution of observing n_0 given an expected value of $\mu_S+\mu_B$. We choose a uniform prior probability, $P(\mu_S)$ such that $P(\mu_s)=1$ for $\mu_S \geq 0$. As stated before, the denominator in Equation F.3 may be regarded as a normalization

factor so that Equation F.3 can be written as:

$$P(\mu_S|n_0,\mu_B) \quad \propto \quad \mathscr{L}(n_0|\mu_S+\mu_B) \tag{F.4}$$

Because the number of expected signal events is very small, the Poisson distribution is chosen for the likelihood function describing the conditional probability. If n_0 is the observed number of events, then in the absence of background the likelihood of observing n_0 events given that a mean number of signal events, μ_S, are expected is given by:

$$\mathscr{L}(n_0|\mu) \quad = \quad \frac{\mu_S^{n_0}e^{-\mu_S}}{n_0!} \tag{F.5}$$

Since n_B background events are expected in the final event selection, the likelihood needs to be modified to accommodate the possibility of other types of event classification. In this case it is straightforward to include the background:

$$\mathscr{L}(n_0|\mu_S+\mu_B) \quad = \quad \frac{(\mu_S+\mu_B)^{n_0}e^{-(\mu_S+\mu_B)}}{n_0!}, \tag{F.6}$$

where μ_B is the expected mean number of background events and must be known exactly. However in experiments μ_B is not exactly known but is calculated within an overall uncertainty, σ_B, from statistical and systematic errors. Likewise there is an additional error associated with the signal acceptance denoted by σ_A. To incorporate these errors, the likelihood is "smeared" by these errors which are assumed to have a gaussian distribution. This is done by multiplying the probability distributions by gaussians having widths proportional to the corresponding signal and background acceptance uncertainties and summing over values of the expected signal and background events:

$$P(\mu_S|n_0,\mu_B) \propto \frac{1}{2\pi\sigma_B\sigma_S}\int_0^\infty\int_0^\infty \mathscr{L}(n_0|\mu'_B+\mu'_S)e^{\frac{-(\mu_B-\mu'_B)^2}{2\sigma_B^2}}e^{\frac{-(\mu_S-\mu'_S)^2}{2\sigma_S^2}}d\mu'_Bd\mu'_S, \tag{F.7}$$

where $\sigma_S = \mu_S(\sigma_A/A)$. To compute the confidence level of the upper limit, we sum over the possible Poisson likelihoods. The confidence level is given by $\epsilon = 1-$ CL, where $1-\epsilon$ is the probability of observing more than n_0 events. The upper limit on μ_S is defined as that value, μ_S^{lim} for which we expect to observe n_0 events or fewer for a desired CL, i.e.:

$$1-CL \quad = \quad \frac{\int_{\mu_S^{lim}}^\infty P(\mu_S|n_0,\mu_B)d\mu_S}{\int_0^\infty P(\mu_S|n_0,\mu_B)d\mu_S}. \tag{F.8}$$

n_0	$\epsilon =$ 10%	$\epsilon =$ 5 %	n_0	$\epsilon =$ 10 %	$\epsilon =$ 5%
0	2.30	3.00	6	10.53	11.84
1	3.89	4.74	7	11.77	13.15
2	5.32	6.30	8	13.00	14.44
3	6.68	7.75	9	14.21	15.71
4	7.99	9.15	10	15.41	16.96
5	9.27	10.51	11	16.60	18.21

Table F.1: The Poisson upper limit N for n_0 observed events.

Appendix G

Transverse kinematic variables check between LQ and Top

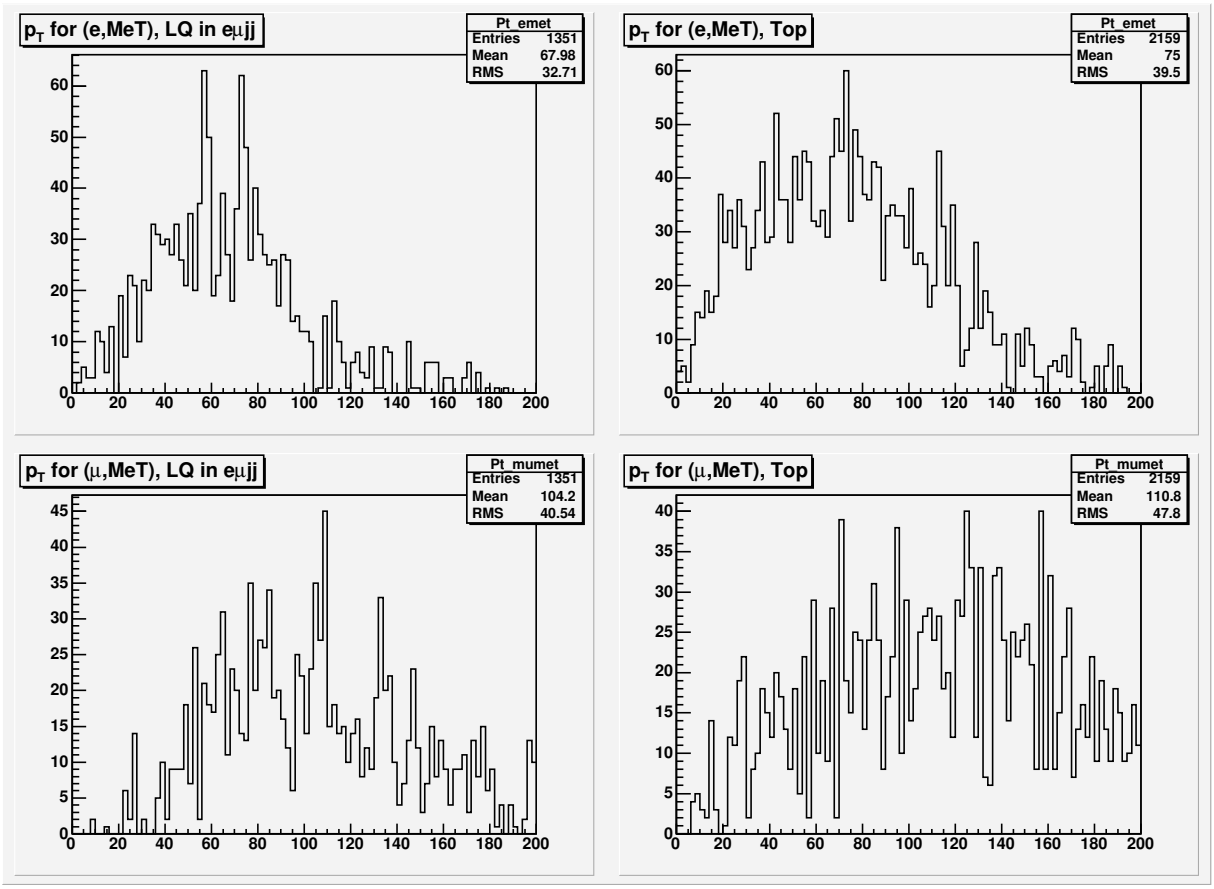

Figure G.1: The left top, $p_T(e, \not\!\!E_T)$ distribution of LQ @ 120 GeV/c^2, right top is for inclusive Top. The bottom two are $p_T(\mu, \not\!\!E_T)$ distributions for LQ and Top, from left to right.

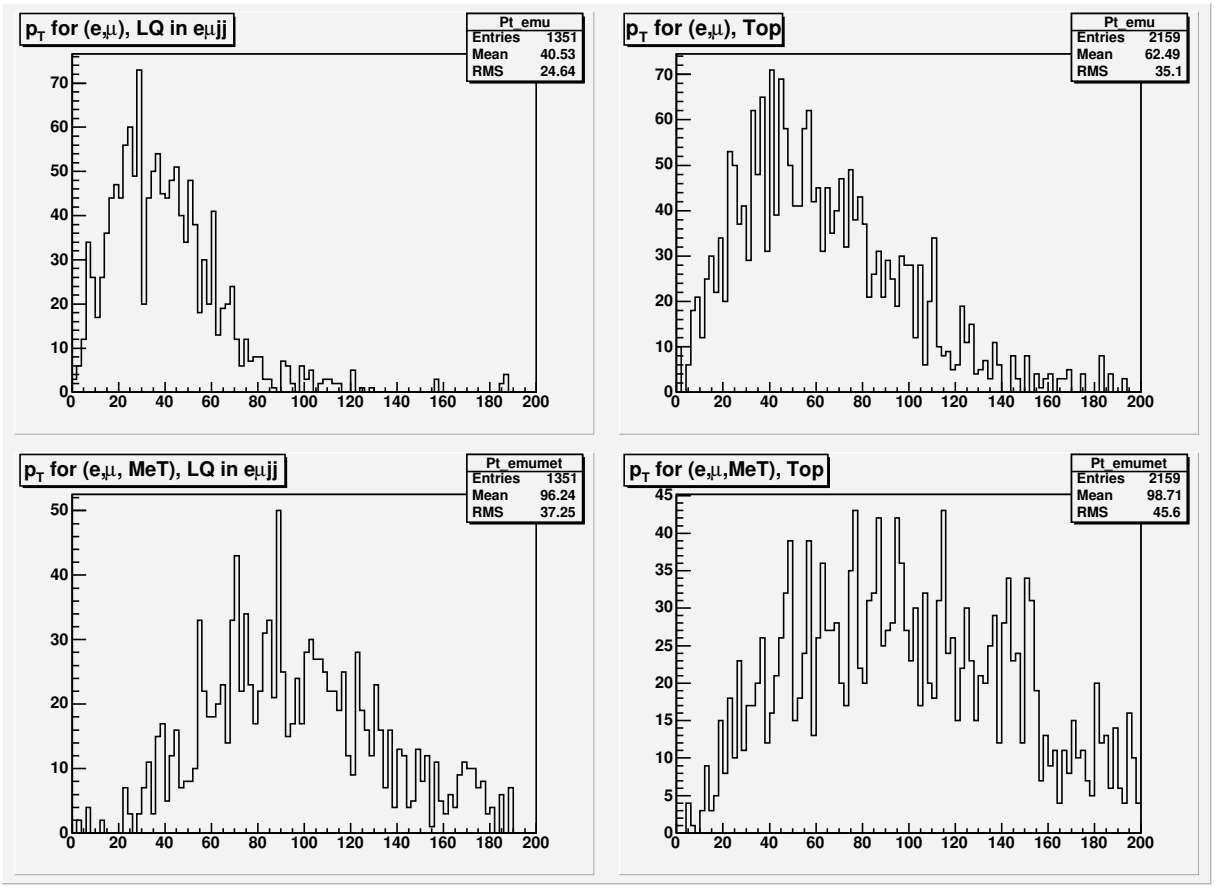

Figure G.2: The left top, $p_T(e,\mu)$ distribution of LQ @ 120 GeV/c^2, right top is for inclusive Top. The bottom two are $p_T(e,\mu,\not\!\!E_T)$ distributions for LQ and Top, from left to right.

List of Tables

List of Figures

Bibliography

[1] The CDF II Collaboration. Homepage at `http://www-cdf.fnal.gov`

[2] M. Krämar *et al.*, *Pair Production of Scalar Leptoquarks at the TeVatron*, Phys. Rev. Lett. **79**, 341 (1997).

[3] J.A. Grifols and A. Méndez, Phys. Rev. D **26**, 324 (1982); I. Antoniadis, L. Baulieu, and F. Delduc, Z. Phys. C **23**, 119 (1984); E. Eichten, I. Hinchliffe, K.D. Kane, and C. Quigg, Rev. Mod. Phys. C **56**, 579 (1984); G. Altarelli and R. Rückl, Phys. Lett. B **144**, 126 (1984); S. Dawson, E. Eichten, and C. Quigg, Phys. Rev. D **31**, 1581 (1985); J. Blümlein, E. Boos, and A. Kryukov in [34].

[4] P. Arnold and C. Wendt, Phys. Rev. D **33**, 1873 (1986); G.V. Borisov, Y.F. Pirogov, and K.R. Rudakov, Z. Phys. C **36**, 217 (1987); J.L. Hewett, T.G. Rizzo, S. Pakvasa, H.E. Haber, and A. Pomarol, Argonne Accel. Phys., 539 (1993); J. Blümlein, E. Boos, and A. Kryukov in [34].

[5] Chris Quigg. *Quantum Theories of the Strong, Weak, and Electromagnetic Interactions.* Westview Press, New York, NY, (1997).

[6] H. Georgi and S.L. Glashow. *Unity of All Elementary-Particle Forces*, Phys. Rev. Lett. **32**, 438 (1974).

[7] H1 Collaboration, Adloff C. *et al.* Z. Physics C **74**, 191 (1997).

[8] Nucl. Instr. and Meth. **A425** 86.

[9] L. Balka *et al.*, Nucl. Instr. and Meth. **A267**, 272 (1988).

[10] F. Abe *et al.*, Phys. Rev. D **50**, 2296 (1994).

[11] Nucl. Instr. and Meth., **A267**, 272.

[12] Nucl. Instr. and Meth., **A267**, 301.

[13] Y. Seiya *et al.*, Nucl. Instr and Meth. **A480**, 524 (2002).

[14] J. Conway. and K. Maeshima, *Upper Limits on Poisson Processes Incorporating Uncertainties in Acceptance and Background*, CDF Internal Note 4476, Version 2 (1998).

[15] M. Kuze, Y. Sirois, *Search for Particles and Forces Beyond the Standard Model at HERA ep and Tevatron pp Colliders*, DESY 02-165 (2002).

[16] A. Mehta, *HERA Upgrade and Prospects*, X International Workshop on Deep Inelastic Scattering (DIS2002), Cracow, Poland (2002).

[17] J. Blümlein, E. Boos and A. Kryukov, *Leptoquark pari production cross-sections at hadron colliders*, [hep-ph/9811271].

[18] B. Dion, G. Simon Marleau and M. de Montigny, Eur. Phys. J. C2, 497 (1998); O.J.P. Éboli, R.Z. Runchal and T.L. Lungov, Phys. Rev. D **57**, 1517 (1998).

[19] Atlas Collaboration, *Atlas Technical Proposal*, CERN/LHCC/99-15 (1999).

[20] Description of data samples for Top and Electroweak groups for Summer 2003. *Description of data samples for Top and Electroweak groups for Summer 2003*, CDF Note 6548 (2003).

[21] Searches for New Particles in High Mass Dimuon Channel in CDF Run II Data. *Searches for New Particles in High Mass Dimuon Channel in CDF Run II Data*, CDF Note 6344 (2003).

[22] Searches for New Particles in High Mass Dimuon Channel in CDF Run II Data. *Searches for New Particles in High Mass Dimuon Channel in CDF Run II Data*, CDF Note 6602 (2003).

[23] *ROOT - An Object Oriented Data Analysis Framework*, AIHENP conference, Lausane, (1996).

[24] *New Results on Neutral and Charged Current Scattering at high Q^2 from H1 and ZEUS*, Hamburg, Germany, July 28 - August 1 1997.

[25] L.F. Abbott and E. Farhi. *Are the Weak Interactions Strong?*, Phys. Lett. B **101**, 69 (1981).

[26] Abid Patwa. Personal correspondence.

[27] D. Acosta, D. Konigsberg, J. Tsybychev, and Wang S.M. *Update on the Search for First-Generation Leptoquarks in the Jets and MET Topology*, CDF Internal Note 6593 (2003).

[28] A.D. Martin, R.G. Roberts, W.J. Stirling and R.S Thorne. Parton Distributions: a New Global Analysis. see also `http://consult.cern.ch/writeup/pdflib/`.

[29] I.J.R. Aitchison and A.J.G. Hey. *Gauge Theories in Particle Physics.* Institute of Physics Publishing, Ltd, Bristol, UK, (1989).

[30] The CDF Trigger and Datasets Working Group Albrow, M. *et al. CDF Run-II Trigger Table and Datasets Plan*, CDF Internal Note 4718 (2001).

[31] B. Ashmankas. *et al. Open-cell Chamber to Replace the CTC*, CDF Internal Note 3648 (1996).

[32] W. Beenakker, H. Kuijf, and W.L. van Neervan. *QCD corrections to heavy-quark production in $p\bar{p}$ collisions*, Phys. Rev. D **40**, 1 (1989).

[33] A. Bhatti, M.D. Shapiro, and Lamoureux J. *Combined Calorimetry Tower Elements*, CDF Internal Note 3952 (1996).

[34] J. Blümlein, E. Boos, and A. Kryukov. *Leptoquark Pair Production in Hadronic Interactions*, [hep-ph/9610408] (1996).

[35] J. Botts, J.G. Morfin, J.F. Owens, J. Qiu, W. Tung, and H. Weerts. *CTEQ Parton Distributions and Flavor Dependence of Sea Quarks*, Phys. Lett. B **304**, 159 (1993) [hep-ph/9303255].

[36] `http://www-clued0.fnal.gov/~nunne/cross-sections/lq-xsect-1.96TeV_sc2M_cteq61.out`
`http://www-clued0.fnal.gov/~nunne/cross-sections/lq-xsect-1.96TeV_sc1M_cteq61.out`
`http://www-clued0.fnal.gov/~nunne/cross-sections/lq-xsect-1.96TeV_sc0.5M_cteq61.out`

[37] S.T. Buchmüller, R.D. Peccei, and T. Yanagida. *The Structure of Weak Interactions for Composite Quarks and Leptons*, Nuclear Physics B **244**, 186 (1984).

[38] W. Buchmüller, S.T. Love, R.D. Peccei, and T. Yanagida. "Quasi Goldstone Fermions", Phys. Lett. B **115**, 233 (1982).

[39] W. Buchmüller, R. Rückl, and D. Wyler. *Leptoquarks in lepton-quark collisions*, Phys. Lett. B **191**, 442 (1987).

[40] CDF and DØ Collaborations. *Combined Limits on First Generation Leptoquarks from the CDF and DØ Experiments*, Fermilab Report Number FERMILAB-PUB-98-312-E (1997) [hep-ex/9810015].

[41] CDF Collaboration,A. Bhatti, F.Canelli, B. Heinemann *et al. Determination of the Jet Energy Scale at the Collider Detector at Fermilab* hep-ex/0510047 (2005).

[42] CDF Collaboration, F. Abe *et al.* Phys. Rev. Lett. **79**, 4327 (1997).

[43] CDF Collaboration, F. Abe *et al.* Phys. Rev. Lett. **81**, 4806 (1998).

[44] CDF Collaboration, F. Abe *et al.* Phys. Rev. Lett. **78**, 2906 (1997).

[45] CDF Collaboration, F. Abe *et al. The CDF Run II Silicon Tracking System*, Nucl. Instrum. Meth. A447 (2000), pp. 1-8.

[46] CDF Collaboration, T. Affolder *et al. Search for Second and Third Generation Leptoquarks Including Production via Technicolor Interactions in $p\bar{p}$ collisions at $\sqrt{s} = 1.8$ TeV*, Submitted to Phys. Rev. Lett., [hep-ex/0004003].

[47] The CDF Collaboration. *The CDF II Detector Technical Design Report*, Fermilab Report No. Fermilab-Pub-96/390-E (1996).

[48] The CDF Collaboration. *The CDF IIb Detector Technical Design Report*, Fermilab `http://www-cdf.fnal.gov/upgrades/run2b/Documents/tdr_sep02.pdf`, September 2002.

[49] S.Jadach, Z.Was, R.Decker, J.Kuhn. *The Tau Decay Library Tauola: Version 2.4.*, Nucl.Phys.Proc.Suppl. 98 (2001) 96-102, [cern/th-6793-93].

[50] T.Moulik, K. Jieun, P.Murat. *CDF Run II interface to TAUOLA, a decay library for polarized tau leptons*, CDF note 5719 (2002).

[51] R. Cousins. *Why isn't every physicist a Bayesian?*, Am. J. Phys. **65**, 398 (1995).

[52] D. Amidei *et al. Measurements of $\sigma \cdot W \to \mu\nu$ and $Z \to \mu\mu$ and $\frac{W\to\mu\nu}{Z\to\mu\mu}$ using CDF Run II Data*, CDF Note 6711 (2004).

[53] D. Bogert, W. Foster, W. Fowler, S. Holmes, G. Jackson, P. Martin, T. Pawlak. *The Status of the Fermilab Main Injector Project*, Prepared for 5th European Particle Accelerator Conference (EPAC 96), Sitges, Spain, 10-14 Jun (1996).

[54] DØ Collaboration, B. Abbott *et al.* Phys. Rev. D **64**, 092004 (2001).

[55] DØ Collaboration, B. Abbott *et al.* Phys. Rev. Lett. **79**, 4321 (1998).

[56] DØ Collaboration, B. Abbott *et al.* Phys. Rev. Lett., **84**, 2088 (2000).

[57] DØ Collaboration, B. Abbott *et al.* Phys. Rev. Lett. **83**, 2896 (1999).

[58] DØ Collaboration, B. Abbott *et al.* Phys. Rev. Lett. **81**, 38 (1998).

[59] DØ Collaboration, V.M. Abazov *et al.* Phys. Rev. Lett. **88**, 191801 (2002).

[60] Manuel Drees. *An Introduction to Supersymmetry*, [hep-ph/9611409v1] (1996).

[61] O.J.P. Éboli and T.L. Lungov. "Single production of leptoquarks at the Tevatron", Phys. Rev. D **61**, 75015 (2000).

[62] F. Abe *et al., CDF Collaboration. Search for First Generation Leptoquark Pair Production in $p\bar{p}$ Collisions at $\sqrt{s} = 1.8$ TeV*, [hep-ex/9707033v1] (1997).

[63] E. Farhi and L. Susskind. *Technicolour*, Phys. Rep. **74** No. 3, 277 (1981).

[64] Stephen P. Martin. *A Supersymmetry Primer*, hep-ph/9709356 (1997).

[65] *Averaging of the inelastic cross sections measured by the CDF and the E811 experiments*, Fermilab Report No. Fermilab-FN-0741 (2003).

[66] Y. Fukuda and *et al. Evidence for Oscillation of Atmospheric Neutrinos*, Phys. Rev. Lett. **81**, 1562 (1999).

[67] G. Ascoli *et al. CDF Central Muon Detector*, Nucl. Inst. and Meth. **A269**, 33 (1988).

[68] G. Brandenburg *et al. . The CDF Run 1 Muon System Upgrade*, CDF Internal Note 6362 (2002).

[69] H. Georgi and S.L. Glashow. *Unified theory of elementary-particle forces*, Physics Today, 30-39 (1980).

[70] G.J. Feldman and R.D. Cousins. *Unified approach to the classical statistical analysis of small signals*, Phys. Rev. D **57**, 3873 (1998).

[71] David Griffiths. *Introduction to Elementary Particles.* John Wiley and Sons, Inc., New York, NY, (1987).

[72] S.L. Glashow H. Georgi. *Gauge Theories Without Anomalies*, Phys. Rev. D **6**, 429 (1972).

[73] H1 BSM Working Group. *New Results on NC and CC-like Events at Very High Q^2 in DIS Collisions at HERA*, July 1997.

[74] Brian Hatfield. *Quantum Field Theory of Point Particles and Strings.* Addison-Wesley, Reading, MA, (1992).

[75] J.L. Hewett and S. Pakvasa. *Sclalar-leptoquark production at hadron colliders*, Phys. Rev. D **37**, 3165 (1988).

[76] R. Hughes, E. Thomson, and B. Winer. *Performance Study of the eXtremely Fast Tracker at High Luminosity*, CDF Internal Note 5986 (2002).

[77] J. Abbott *et al., DØ Collaboration. Search for Scalar Leptoquark Pairs Decaying to Electrons and jets in $p\bar{p}$ Collisions*, [hep-ex/9707033v1] (1997).

[78] J. Campbell, R.K. Ellis and D. Rainwater. *Next-to-leading order QCD predictions for $W + 2$ jet and $Z + 2$ jet production at the CERN LHC*, Fermilab Report No. FERMILAB-Pub-03/234-T, [hep-ph/0308195] (2003); see also `http::/mcfm.fnal.gov/`.

[79] J. Elias. *et al. Luminosity monitor based on Cherenkov counters for $p\bar{p}$ colliders, Submitted to* Nucl. Inst. Meth.

[80] J. Konsigsberg J. *et al. Luminosity Information in Run II*, CDF Internal Note 4831 (1999).

[81] José Wudka. *Composite Leptoquarks*, Phys. Lett. B **167**, 337 (1986).

[82] K. Byrum *et al.* Nucl. Inst. and Meth. **A364**, 144 (1995).

[83] Michio Kaku. *Quantum Field Theory.* Oxford University Press, New York, NY, (1993).

[84] Hisanori Kambara. PhD thesis. Ph.D. Thesis: *Search for Second Generation Leptoquarks in $\sqrt{s} = 1.8$ TeV $p\bar{p}$ at CDF*, University of Genève (1998).

[85] B. Kilminster, K. McFarland, and K. Tollefson. *Design and Specifications for the CDF run II Conumer-Server/Logger*, CDF Internal Note 4794 (1998).

[86] M. Krämar. *Leptoquark Production at the Tevatron*, Talk presented at "Beyond the Desert 97", Accelerator and Non-Accelerator Approaches, Castl Ringberg, Tegernsee, Germany, [hep-ph/9707422] (1997).

[87] La Biodola. *Event Builder and Level 3 at the CDF Experiment*, 9th Pisa Meeting on Advanced Detectors, Isola d'Elba, Italy, May 2003. FERMILAB-CONF-03/172-E.

[88] V. Martin and L. Cerrito. *High-pT Muon ID Cuts and Efficiencies for use with 5.3.1 Data and 5.3.3 MC*, CDF Note 7367 (2004).

[89] U. Grundler and A. Taffard. *High-pT Muons Recommended cuts Efficiencies for Summer 2006*, CDF Note 8262 (2006).

[90] M. Coca and E. Halkiadakis. *Central Electron Identification Efficiencies for CDF Run II Analyses*, CDF Note 6580 (2004).

[91] Robert G. Wagner. *Electron Identification for Run II: Algorithms*, CDF Note 5456

[92] M.Griffiths, B.Heinemann and G.Manca *Central Electron ID Efficiencies at Medium Energy*, CDF Note 7233

[93] S.Baroiant, M. Chertok *et al. Measurement of the 8 GeV Inclusive Electron Level 3 Trigger Efficiency Using Conversions*, CDF Note 6324

[94] M.L. Mangano, M. Moretti, F. Piccinini, R. Pittau, A. Polosa. JHEP 0307:001, (2003) [hep-ph/0206293]; see also `http://mlm.home.cern.ch/mlm/alpgen/`.

[95] Lorenzo Moneta. *Combined Results of Searches for Second Generation Leptoquarks*, CDF Internal Note 5790 (2001).

[96] Lorenzo Moneta. *Searches for Second Generation Leptoquarks in $\mu\nu qq$ channel*, CDF Internal Note 5572 (2001).

[97] B. Heinemann and A. Wyatt. *Correction for Leakage Energy in the Central nad Plug Calorimeters in Run II*, CDF Note 6167.

[98] R.G. Wagner. *Understanding and Using Lshr*, CDF Note 6249.

[99] L. Nodulman. *Central Electron Issues for Summer 03*, CDF Internal Note 5572, version 0.2 (2003).

[100] S.Rolli, D. Ryan and H. Sun *run II Second Generation Leptoquark Searches*, CDF Internal Note 7216, (2004).

[101] Donald H. Perkins. *Introduction to High Energy Physics*. Cambridge University Press, Cambridge, UK, 4th edition, (2000).

[102] S. Rolli. Search for First Generation Leptoquarks Pair Production in the eejj Channel. March 2003. *Search for First Generation Leptoquarks Pair Production in the eejj Channel*, CDF Note 6338 (2003).

[103] S. Rolli, D. Ryan, and H. Sun. *Search for 2nd Generation Scalar Leptoquarks*, CDF Note 6733 (2003).

[104] S. Eidelman *et al.* Phys. Lett. B **592** (2004).

[105] W. Sakamoto. *W/Z Cross Section Predictions for $\sqrt{s} = 1.96$ TeV*, CDF Note 6341 (2003).

[106] W.K. Sakumoto and A. Hocker. *Event |Zvtx| < 60 cm Cut Efficiency for Run II*, CDF Note 6331 (2003).

[107] P.C. Salam and A. Salam. *Lepton Number as a Fourth Color*, Phys. Rev. D **10**, 275 (1974).

[108] B. Schrempp and F. Schrempp. *Light Leptoquarks*, Phys. Lett. B **153**, 101 (1985).

[109] B. Schrempp and F. Schrempp. *A Confining $SU(2)_L \times SU(2)_R$ Gauge Model of the Weak Interactions*, Nuclear Physics B 231, 109 (1984).

[110] Federica Strumia. PhD thesis. *Searches for First Generation Leptoquarks in the eeqq and enuqq channels*, University of Geneva (2002).

[111] T. Pratt *et al. Search for Resonances in High Mass Dielectron*, CDF Note 6073 (2003).

[112] T. Sjöstrand, P. Edén, C. Friberg, L. Lönnblad, G. Miu, S. Mrenna and E. Norrbin. see also `http://www.thep.lu.se/~torbjorn/Pythia.html`.

[113] A. Taffard. *Run II Cosmic Ray Tagger*, CDF Internal Note 6100 (2003).

[114] CDF Data Quality Monitoring Team. `http://www-cdf.fnal.gov/internal/dqm/goodrun/good.html`.

[115] The CDF Run II Jet Corrections Group, J.F. Arguin *et al. Generic Jet Energy Corrections for Run II data used for the Winter Confrerences*, CDF Internal Note 6280, version 0.2 (2003).

[116] Thomson, E. and *et al. Online Track Processor for the CDF Upgrade*, IEEE Transactions on Nuclear Science **49**, No. 3, Fermilab Report No. FERMILAB-CONF-02/144-E (2002).

[117] G. Valencia and S. Willenbrock. *Quark-lepton unification and rare meson decays*, Phys. Rev. D **50**, 1 (1994).

[118] S. Weinberg. *Implications of dynamical symmetry breaking*, Phys. Rev. D, **13**, 974 (1976).

[119] H. Wenzel and K. Maeshima. *Search for Pati-Salam Leptoquarks via the decays $B_S \to e^{\pm}\mu^{\mp}$ and $B_d \to e^{\pm}\mu^{\mp}$*, CDF Note 4224 (1998).

[120] ZEUS Collaboration. *Search for Leptoquarks in ep Collisions at HERA*, Submitted to the XXXIst International Conference on High Energy Physics, Amsterdam, The Netherlands (2002).

[121] ZEUS Collaboration, J. Breitweg *et al.* Z. Phys. C **74**, 204 (1997).